

CVD DIAMOND GRAIN QUALITY ENHANCEMENT
BY POST-PRODUCTION LASER ANNEALING

By

KAREN ELAINE SUHM

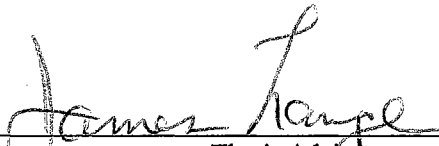
Bachelor of Science
Oklahoma State University
Stillwater, Oklahoma
1991

Master of Science
Oklahoma State University
Stillwater, Oklahoma
1993

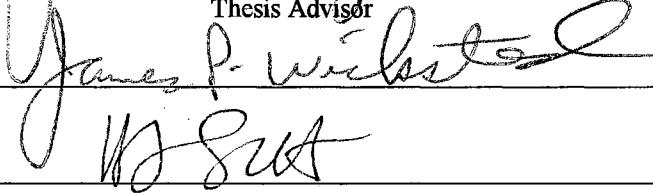
Submitted to the Faculty of the
Graduate College of the
Oklahoma State University
in partial fulfillment of
the requirements for
the Degree of
DOCTOR OF PHILOSOPHY
December, 1995

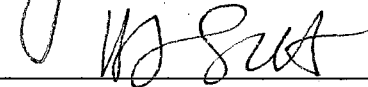
CVD DIAMOND GRAIN QUALITY ENHANCEMENT
BY POST-PRODUCTION LASER ANNEALING

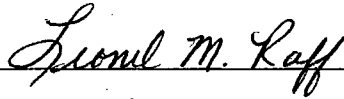
Thesis approved:

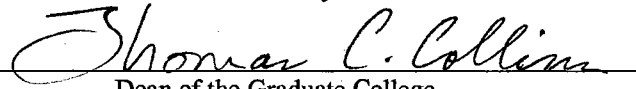


Thesis Advisor









Dean of the Graduate College

ACKNOWLEDGMENTS

The most significant person in my academic career has been my thesis advisor, Dr. Jim Lange. In the years that I have worked with Dr. Lange, he has always given me the freedom to follow my own path, yet has saved me from experimental quicksand when I got stuck. Most importantly, it was Dr. Lange's suggestion to do CVD research that got me a job -- something I feared would be hard to come by with a degree in Physics.

Many thanks also go to the other members of my thesis committee, Dr. Larry Scott, Dr. Jim Wicksted, and Dr. Lionel Raff, for their time and advice, and to Dr. Martin and Charles Hunt, who have let me borrow every piece of equipment they have at least once. Mike Lucas and everyone in the machine shop have also played an instrumental part in my research (literally) while Cheryl Outon and Susan Cantrell have done for me what Kinko's would consider impossible.

On the home front, I owe infinite quanta of thanks to Jerry Little, my dedicated husband, for his undying support in all my endeavors. He has seldom complained, whether doing dishes, laundry, or the grocery shopping, and he griped only on those rare occasions when I forgot to feed him. Through our college years, we have often been separated by our schoolwork, but have still managed to grow together. I look forward to facing the future with Jerry by my side.

My parents, Ray and June Suhm, are also worthy of thanks, for without them this thesis (and myself) would not have been possible. Somewhere in my genes are my father's quest for knowledge and my mother's work ethics, my father's logic and my mother's creativity, all recessively hidden. Without my parents I would have no blood relatives to applaud me at the hooding convocation.

Last of all, I would like to thank my friends for being there through it all. We have shared homework, guinea pig noises, and spitting-image professor imitations, pulled all-nighters, experienced the Math Methods "fire drill final", and spent quite a few Friday nights at Brannigan's. I thank all of you for everything you've done and hope none of you are upset that I didn't name you specifically.

TABLE OF CONTENTS

Chapter	Page
I. INTRODUCTION.....	1
Structure, Properties, and Applications of Diamond	1
The History of Diamond Synthesis	3
Stable High Pressure Diamond Synthesis.....	3
Metastable Low Pressure Diamond Synthesis	4
Raman Spectroscopy	7
Intensity Ratio of Anti-Stokes to Stokes Raman Bands	10
Raman Scattering in Single Crystals.....	11
The Effects of Anharmonicity on Raman Scattering in Solids	16
Summary of Thesis	22
II. SAMPLE PRODUCTION AND ANALYSIS.....	25
Background.....	25
Nucleation.....	25
Growth.....	28
Reported Raman Signatures of the Allotropes of Carbon	31
Experimental Details.....	35
Chemical Vapor Deposition.....	35
Micro-Raman Spectrometer	38
Results and Discussion.....	42
Grain Categorization	42
Evaluation of Deposition Parameters	59
Chapter Summary	66
III. CVD DIAMOND GRAIN QUALITY ENHANCEMENT BY POST- PRODUCTION LASER ANNEALING.....	67
Introduction	67
Experimental Method.....	68
Results and Discussion.....	69
The Universal Temperature Dependence of the $k \approx 0$ Optic Mode Frequency of CVD Diamond Grains	72
The Irreversible Hysteresis of the Diamond Peak Width with Grain Conversion	80
Increases in the Scattering Intensity of the Diamond Peak with Grain Conversion	86
Studies of the Underlying Silicon Substrate and the Diamond/Silicon Interface.....	91

Chapter	Page
Tube Furnace vs. Laser Annealing.....	98
The Effects of Nitrogen on Diamond Grain Growth and Conversion	101
Suggested Models for the CVD Diamond Grain Conversion Process.....	105
Chapter Summary	108
IV. SUMMARY AND SUGGESTIONS FOR FUTURE RESEARCH.....	111
REFERENCES.....	113
APPENDICES	116
APPENDIX A -- BASIC THEORY OF RAMAN SCATTERING.....	116
APPENDIX B --DERIVATION OF RAYLEIGH'S ω^4 LAW	123
APPENDIX C -- DIAGONALIZATION OF THE HARMONIC OSCILLATOR ENERGY MATRIX.....	127
APPENDIX D --DERIVATION OF THE SCATTERING EFFICIENCY.....	129

LIST OF TABLES

Table	Page
I. SUMMARY OF RAMAN PEAK POSITIONS AND WIDTHS FOR SEVERAL ALLOTROPES OF CARBON	32
II. SUMMARY OF CHEMICAL VAPOR DEPOSITION GROWTH PARAMETERS FOR ALL SAMPLES IN THIS STUDY	43

LIST OF FIGURES

Figure	Page
1.1. Two perspectives on the diamond structure.....	2
1.2. Phase diagram of carbon.....	6
1.3. Energy level diagrams of Rayleigh scattering, Stokes Raman scattering, and anti-Stokes Raman scattering.....	9
1.4. Phonon dispersion curves for a one-dimensional chain lattice with two types of atoms.....	13
1.5. The single, triply-degenerate optic mode of diamond.....	15
2.1. Hydrocarbon cage compounds with six-membered carbon rings which could function as nuclei for-diamond crystal formation.....	27
2.2. Octahedral, cubo-octahedral, and cubic crystal morphologies.....	29
2.3. Phonon dispersion curves of diamond.....	33
2.4. Filament-assisted chemical vapor deposition chamber used for sample production.....	36
2.5. Micro-Raman spectrometer used for sample characterization.....	39
2.6. Substrate temperature vs. total flow rate for CVD diamond films in this study.....	45
2.7. Typical distribution of CVD diamond grains on the silicon substrate.....	47
2.8. SEM photographs of the different CVD diamond grain morphologies represented in this study.....	48
2.9. Typical Raman spectra for diamond-like carbon and amorphous carbon produced in this study.....	51
2.10. Typical Raman spectra for diamond produced in this study.....	52
2.11. Percentage of CVD grains containing diamond as a function of grain type.....	54
2.12. Average width of the CVD grain Raman diamond peak as a function of grain type.....	55

Figure	Page
2.13. Percentage of CVD grains which vaporized at 500 mW laser power as a function of grain type.....	57
2.14. Average position of the CVD grain Raman diamond peak as a function of grain type.....	58
2.15. Average methane concentration for CVD grains as a function of grain type	60
2.16. Schematic of a simple filament geometry.....	63
2.17. Temperature profiles across the silicon substrate for filament-to-substrate distances, h_f , of 5, 6, and 7 mm.....	65
3.1. SEM photographs of laser-annealed cauliflower and cauli-faceted CVD diamond grains.....	71
3.2. The downshifting and broadening of the Raman diamond peak with increased temperatures.....	73
3.3. The universal diamond peak position vs. temperature curve for all CVD diamond grains in this study.....	75
3.4. The splitting of the diamond peak with increased temperatures	76
3.5. The universal diamond peak position vs. temperature curve fit to the equation for the volume-expansion shift.....	79
3.6. Typical diamond peak width vs. temperature curve for CVD diamond grains in this study.....	81
3.7. Irreversible hysteresis of the diamond peak width vs. temperature curve which occurred with grain conversion	84
3.8. Raman spectra taken before and after the conversion-induced hysteresis shown in Figure 3.7.....	85
3.9. The uprising of the diamond peak from out of the disordered sp^3 background with grain conversion	87
3.10. A typical example of the increase in scattering intensity seen upon grain conversion	88
3.11. Spatial coordinates in the backscattering configuration.....	89
3.12. The universal silicon peak position vs. temperature curve for the silicon substrate beneath CVD diamond grains	92
3.13. The universal silicon peak width vs. temperature curve for the silicon substrate beneath CVD diamond grains	94

Figure	Page
3.14. Diamond grain temperature as a function of the temperature of the underlying silicon substrate.....	96
3.15. Silicon peaks obtained from the exposed surface of a CVD-processed silicon wafer and a clean silicon wafer for comparison.....	97
3.16. SEM photographs of black cauliflower grains with (100) faces taken before and after tube furnace annealing in air at 800°C for 30 minutes	99
3.17. SEM close-up of the central grain in Figure 3.16.....	100
3.18. SEM photographs of cauliflower grains with (100) faces and cauliflower grains after tube furnace annealing in air at 800°C for 30 minutes	102
3.19. Raman spectra of CVD grains containing high quality, single-crystal diamond and polycrystalline disordered sp^3 -bonded carbon before and after tube furnace annealing	103
3.20. The homogeneous defect distribution model proposed to explain grain conversion.....	106
3.21. The radially-varying defect distribution model proposed to explain grain conversion.....	108
A.1. Primed coordinate system (x' , y' , z') rotating with respect to a fixed coordinate system (x , y , z) about the z ($=z'$) axis with frequency ν_T	119

CHAPTER 1

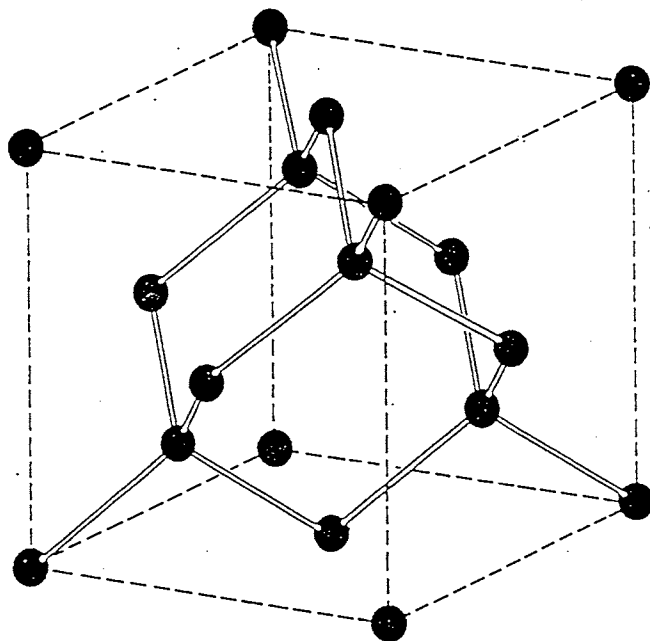
INTRODUCTION

Structure, Properties, and Applications of Diamond

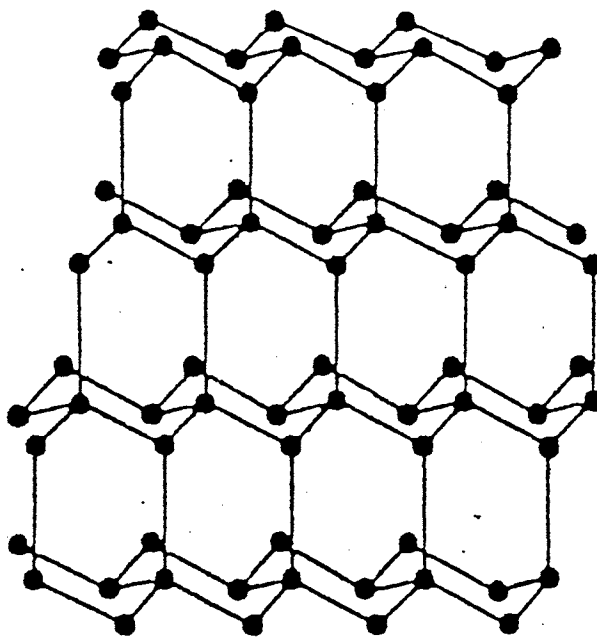
The diamond lattice is face-centered cubic with a basis of two identical carbon atoms situated at $0, 0, 0$ and $\frac{1}{4}, \frac{1}{4}, \frac{1}{4}$ relative to each lattice point. Every carbon atom is covalently bonded to four other carbon atoms, giving diamond the tetrahedral sp^3 electronic configuration. In this formation, the atoms of a diamond crystal are more densely packed than those in any other known material. The conventional cubic cell measures 3.56\AA on a side, while nearest neighbors are 1.54\AA away from each other [1]. The diamond structure may also be visualized as stacked planes of six-membered hexagonal carbon rings. The six carbon atoms in any given ring are alternately situated higher and lower than the central plane in what is labeled the "chair" configuration. Collections of planes are layered in the stacking sequence ABCABC, with the normal to these planes corresponding to the $\{111\}$ direction of the conventional face-centered cubic cell. These two perspectives on the diamond structure are illustrated in Figure 1.1.

Diamond has unique mechanical, electrical, and optical properties which make it one of the most useful crystalline solids known to man. The only weakness in the diamond structure lies in the octahedral planes, corresponding to the $\{111\}$ direction, where diamond crystals can be cleaved with relative ease. Diamond has a low coefficient of friction, equaling that of Teflon, and is well-suited for abrasive, tribological, and wear-resistant applications.

As a result of the close-packing of carbon atoms, diamond has a thermal conductivity unsurpassed by any other material -- at $20.00\text{ W/cm}\cdot^\circ\text{C}$, it is almost five times greater than that of silver [1]. Combined with an electrical resistivity of $10^{15}\text{ ohm}\cdot\text{cm}$, a band gap of 5.45 eV , and a low coefficient of absorption, diamond is the perfect heat sink for high-power electronic and optical devices [1]. It is also the most transparent substance in the far infra-red and is resistant to both corrosion and radiation damage.



(a)



(b)

Figure 1.1. Two perspectives on the diamond structure. (a) Face-centered cubic lattice with carbon atoms at $0, 0, 0$ and $\frac{1}{4}, \frac{1}{4}, \frac{1}{4}$. (b) Planes of puckered six-membered carbon rings stacked in the sequence ABCABC.

The electronic properties of diamond make it competitive with and superior to many conventional semiconductor materials. It has high electron and hole mobilities, high saturation velocities, and a high breakdown voltage. Diamond is able to dissipate power 8200 times more easily than silicon and has a high frequency limit 32 times larger [2]. Additionally, by doping diamond with boron, nitrogen, phosphorous, and similar materials, its electronic properties may be favorably altered. Diamond has an extensive list of applications which grows with improvements in technology. Fortunately, the demand for diamond will never exceed the supply since man now has the ability to cheaply synthesize diamond in a matter of hours or days.

The History of Diamond Synthesis

In 1797, Smithson Tennant demonstrated that diamond was a form of carbon by burning a diamond in oxygen and obtaining carbon dioxide gas and a small amount of ash [3]. By comparing the density of diamond (3.53 g/cm^3) to that of graphite (2.25 g/cm^3), he hypothesized that diamond was the high pressure form of carbon. In the early 1800's, attempts to synthesize diamond began, though efforts remained fruitless for over one hundred years. By the mid-1900's, diamond synthesis attempts had split in two different directions - one focused on the thermodynamically stable region of superhigh pressure and high temperature and the other on the thermodynamically-hindered low pressure region.

Stable High Pressure Diamond Synthesis

In 1955, General Electric scientists Bundy, Hall, Strong, and Wentorf were the first to announce success in diamond synthesis [3]. They had exposed graphite to 1×10^5 atmospheres at 2000°C and, over the next five years, perfected their method in a series of patent applications. Inspired by the presence of iron troilite in the diamond-containing Canon Diablo meteorite from Arizona Meteor Crater, the key to their initial success had been the addition of iron sulfide to a graphitic carbon source [3]. The melted iron acted as a solvent, dissolving the graphite and crystallizing out diamond as it moved from the outer edges of the press to the hot graphite center.

In the 1960's, two other techniques of high pressure diamond synthesis were developed, -- carbonado sintering and the shock compression of graphite. In the carbonado sintering method, diamond powder is briefly exposed to 1×10^5 atmospheres at temperatures near 3000°C [3]. The resulting black, randomly-oriented polycrystalline diamond, known as carbonado, is free of cleavage planes, making it tougher than single crystal diamond under high stress. Graphite shock compression involves the detonation of a steel tube packed with a graphite and metal mixture surrounded by air and explosives. For one fiftieth of a second the pressure reaches 2.5 to 4×10^5 atmospheres and the temperature nears 1000°C [3]. Once cool, the metal is dissolved with acid and the remaining micron-sized diamond particles are suitable for use in abrasives.

Since the 1960's, little has changed in the methods of high pressure diamond synthesis, though equipment capabilities have greatly improved. Today, General Electric's original high pressure process is used to produce roughly 150 tons of diamond grit each year, while carbonado sintering and the graphite shock compression method are also used, though on a much smaller scale [3]. High-pressure synthetic diamonds now represent ninety percent of the world's industrial diamond supply and may someday become competitive with natural diamonds in the gemstone market [3].

Metastable Low Pressure Diamond Synthesis

In the low pressure approach to diamond synthesis, reaction kinetics as well as thermodynamics must be considered. Certain reaction paths are favored over others, so that the end product is not always the most stable one, but the *metastable* one that is created faster than all others. It is in this way that soot forms when a candle is burned -- and soot is in an even higher energy state than diamond.

The low pressure synthesis of diamond was proven feasible in 1952, when William G. Eversole of Union Carbide synthesized diamond by hydrocarbon pyrolysis. In this method, seed crystals of diamond were placed in a tube furnace heated to 1000°C and were then exposed to carbon monoxide and hydrocarbon gases, resulting in homoepitaxial diamond growth [4]. This achievement received little recognition for many years, shadowed by the success of high pressures methods and the impracticality of growing diamond on diamond.

A decade later, Eversole patented a much improved cyclic deposition process in which diamond grit heated in a furnace was alternately exposed to methane (or other hydrocarbon gas) and molecular hydrogen. The key finding of this work was the importance of hydrogen in diamond deposition -- while preferentially etching the non-diamond carbon, it was also found to react with dangling bonds on the diamond surface to form structures more closely resembling that of diamond [4]. In 1966, Angus added diborane to the gas mixture to produce blue semiconducting diamond, thus verifying the metastable low pressure synthesis of diamond, since no other allotrope of carbon turns blue when boron-doped.

Several years later, Derjaguin and Fedoseev discovered that a *mixture* of hydrogen and methane (or other hydrocarbon gas) allowed the simultaneous deposition of diamond and the etching of non-diamond carbon forms [5]. Derjaguin and colleagues also explored alternative vapor deposition techniques, producing higher levels of atomic hydrogen by using a hot filament, electrical discharge, or catalyst [6]. This allowed growth rates of up to 1 $\mu\text{m/hr}$ and the heteroepitaxial deposition of diamond on non-diamond substrates.

In the early 1980's, scientists at Japan's National Institute for Research in Inorganic Materials reproduced the Soviets work and performed their own experiments in the chemical vapor deposition (CVD) of diamond. Setaka, Sato, Matsumoto, and Kamo reported the growth of diamond crystals with well-defined facets using microwave discharges at 10 to 100 Torr and 800-1000°C [7]. Hirose at the Nippon Institute of Technology became the first to synthesize diamond using an oxy-acetylene torch at atmospheric pressure [4].

Today, low pressure CVD diamond synthesis is classified by ionization source into one of four categories: thermally activated, high-frequency plasma, direct current, or combustion flame. As with high pressure methods, almost any source of carbon can be used to produce diamond provided enough energy is supplied to promote sp^3 diamond bonding and an appropriate amount of atomic hydrogen is present to suppress the formation of non-diamond carbon forms. This has been illustrated using graphite, C_{60} , and oil as carbon sources [8-11].

The phase diagram shown in Figure 1.2 summarizes both high and low pressure regions of diamond synthesis [3]. Letter A represents the region where diamond is the thermodynamically stable

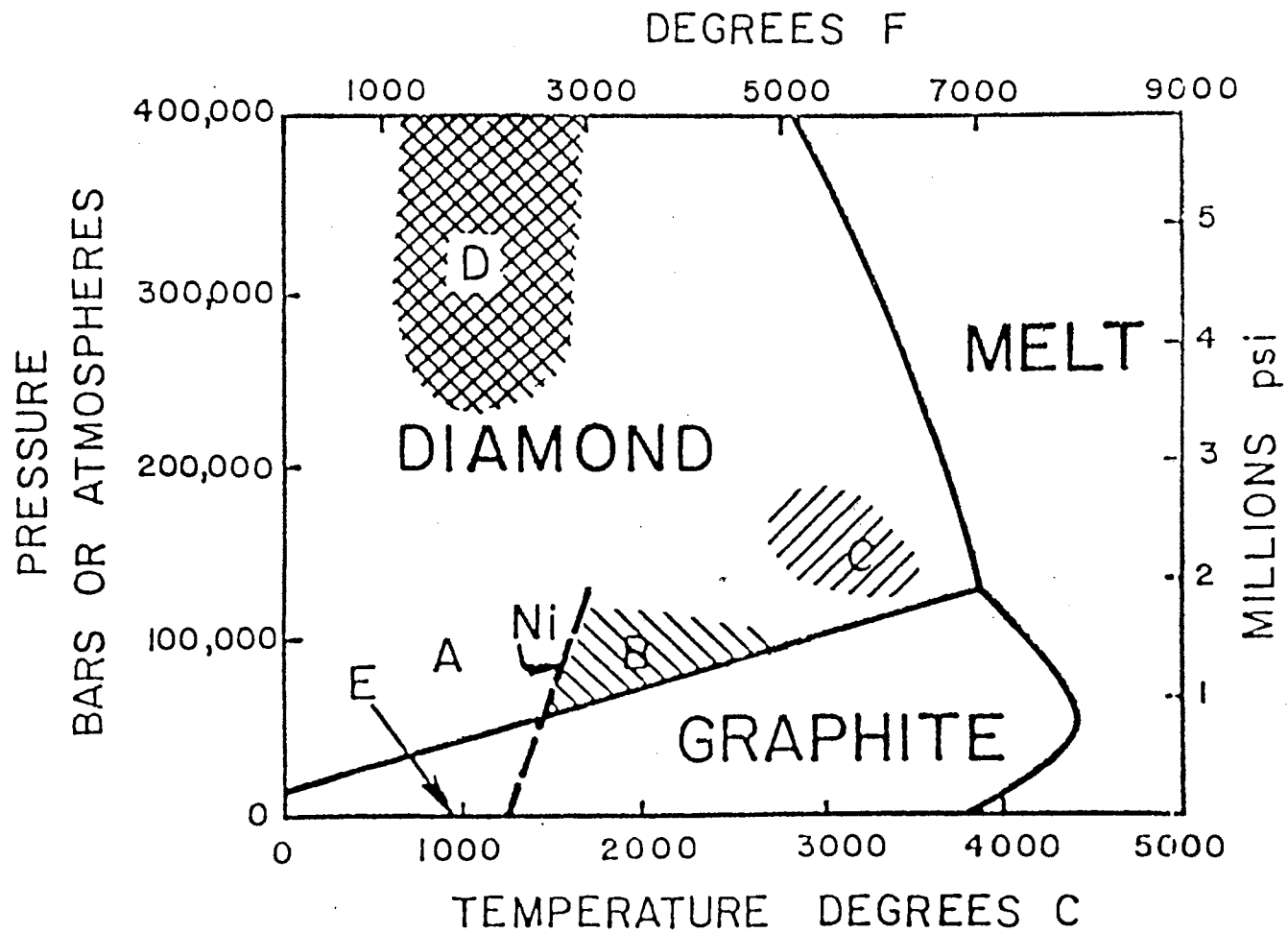


Figure 1.2 Phase diagram of carbon. (A) Region where diamond is thermodynamically stable. (B-D) represent regions where diamond has been produced by (B) General Electric high pressure methods, (C) carbonado sintering, (D) the shock compression of graphite, and (E) chemical vapor deposition (from *Diamond Films and Coatings*, 1993).

form of carbon, while B, C, D, and E respectively represent the metastable regions of General Electric diamond, carbonado sintering, graphite shock compression diamond, and CVD diamond film growth. Note that all but the CVD method involve temperatures and pressures in the region where diamond is the thermodynamically stable form of carbon.

Just as diamond is grown under metastable conditions, so are the other allotropes of carbon, including graphite, diamond-like carbon, and lonsdaleite. Synthetic diamond may contain one or several of these carbon structures if even a single deposition parameter is slightly off. The result is a drastic, undesirable reduction in the mechanical, optical, and electronic properties of the film. Fortunately, several characterization techniques exist with which carbon structures may be identified and growth procedures perfected. Raman spectroscopy is the most practical and informative of these, revealing not only carbon structure, but also crystalline perfection, stress state, domain size, and sample temperature.

Raman Spectroscopy

When a sample is irradiated with monochromatic radiation, the incident radiation may be transmitted, reflected, absorbed, or scattered. Of the radiation scattered by a sample, most will be scattered elastically, whence the incident and scattered photons will have the same energy. The strongest form of elastic scattering is Rayleigh scattering, in which the electrons and protons within a molecule are displaced in opposite directions by the oscillating electric field of the incident radiation. A dipole moment is induced in the molecule, oscillating at the same frequency as the incident radiation. This dipole moment emits radiation in all directions, with the scattered radiation having the same frequency as the incident radiation.

Monochromatic radiation may also be scattered inelastically by a molecule, whence incident and scattered photons do not have the same energy. In this form of scattering, known as the Raman effect, the energy of the molecule is found to change. This effect was predicted theoretically by Smekal in 1923 and experimentally demonstrated in 1928 by C.V. Raman and Landsberg and Mandelstam almost simultaneously [12]. The effect was named after Raman when he received the Nobel Prize in Physics in 1930 for his efforts.

In Raman scattering, a photon with initial energy $h\nu_0$ interacts with a molecule to produce a scattered photon of energy $h\nu_s \neq h\nu_0$. By the law of the conservation of energy, $h\nu_0$ must equal $h\nu_s + h\nu$, where $h\nu$ is the change in the energy of the molecule. In a Stokes transition, $h\nu_s < h\nu_0$ and the molecule gains energy $h\nu$, while in an anti-Stokes transition, $h\nu_s > h\nu_0$ and the molecule gives up energy $h\nu$. Figure 1.3 illustrates the distinction between Rayleigh scattering and Stokes and anti-Stokes Raman scattering. The difference in frequency observed in the Raman effect is caused by an energy exchange between the incident radiation and one of the normal modes of the scattering material. The normal mode involved could be a vibrational or rotational mode in a molecule, a lattice mode in a crystal, or a mixture of these modes in amorphous materials [13].

In the case of free molecules, electronic, vibrational, and rotational Raman effects exist. These effects respectively involve transitions between molecular energy levels, quantized vibrational states, and quantized rotational states. In each case, radiation of frequency ν will either be absorbed or emitted, such that

$$h\nu = |E_f - E_i|,$$

where electronic transitions are largest and rotational transitions are smallest. The Raman effect thus follows the selection rule

$$h\nu_0 \pm h\nu = h\nu_s,$$

where the plus and minus signs correspond to anti-Stokes and Stokes Raman scattering, respectively. If there is no energy transition equal to $h\nu$, then the corresponding transition from $h\nu_0$ to $h\nu_s$ is forbidden. A combination of the electronic, vibrational, and rotational effects may also occur together, as is the case in rotational-vibrational transitions.

The effects of Rayleigh scattering, vibrational, rotational, and rotational-vibrational Raman scattering are derived classically in Appendix A. While the classical treatment successfully accounts for the various frequency shifts present in Raman scattering, it fails in its result for the intensity ratio of the anti-Stokes to Stokes Raman lines. In this case, a quantum mechanical treatment is needed to obtain a theoretical result in agreement with experiment.

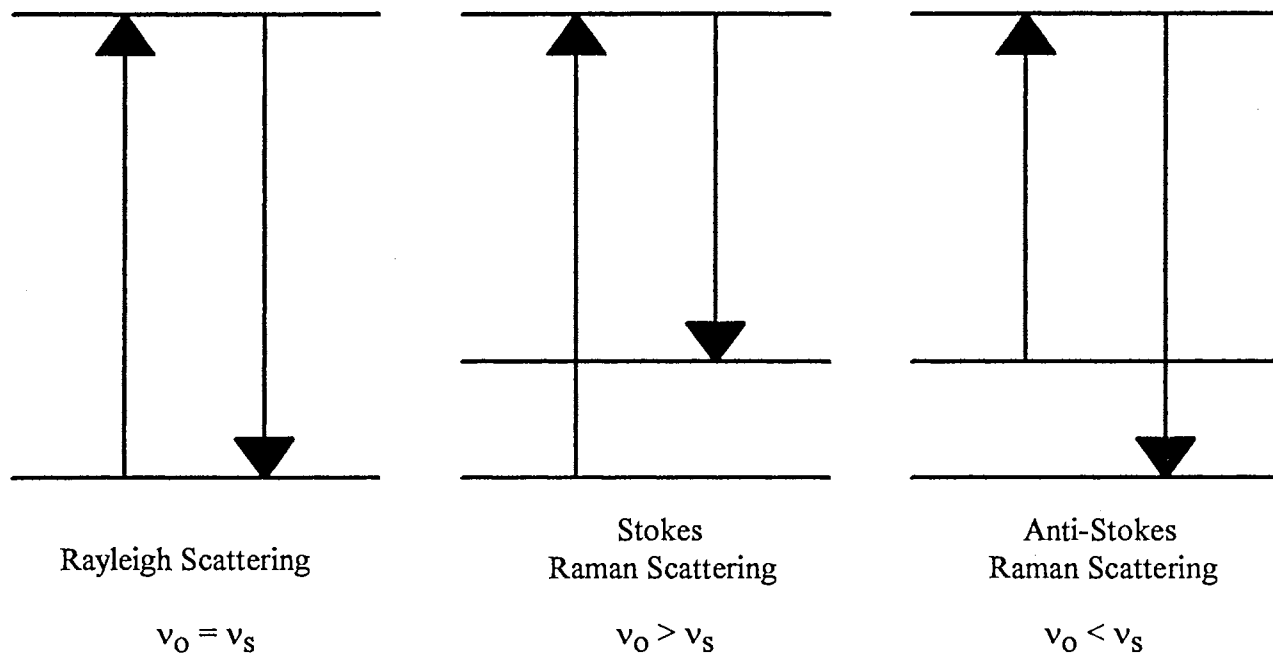


Figure 1.3 Energy level diagrams of Rayleigh scattering, Stokes Raman scattering, and anti-Stokes Raman scattering.

Intensity Ratio of Anti-Stokes to Stokes Raman Bands

Though useful in showing the existence of the Raman effect, classical mechanics does not correctly predict the ratio of the anti-Stokes band to the Stokes band. The error in the classical approach lies in the assumption that there are as many molecules in a position to give up vibrational energy as there are in a position to receive the energy. In the quantum mechanical treatment, however, most molecules are considered to be in the ground state at room temperature, with very few in the higher energy levels.

The intensity of scattered radiation is proportional to the fourth power of the frequency of the emitted radiation, as derived in Appendix B. If there are N_k molecules in the k^{th} energy level and N_n molecules in the n^{th} energy level, which is higher than the k^{th} energy level, a transition from k to n , representing a Stokes transition, will thus have an average intensity proportional to $N_k(\nu_0 - \nu_{nk})^4$. A similar transition from n to k , representing an anti-Stokes transition, will have an average intensity proportional to $N_n(\nu_0 + \nu_{nk})^4$. Combining these relations, the intensity ratio of the anti-Stokes band to the Stokes band is thus

$$\frac{I_A}{I_S} = \frac{N_n(\nu_0 + \nu_{nk})^4}{N_k(\nu_0 - \nu_{nk})^4},$$

which agrees with the classical result if the number of molecules in each energy level is taken to be equal.

In the quantum mechanical approach, however, N_n and N_k are related by the Boltzmann distribution function, so that

$$\frac{N_n}{N_k} = e^{-h\nu_{nk} / kT},$$

where h is Planck's constant, k is Boltzmann's constant, and T is the temperature in degrees Kelvin.

Inserting this into the equation for (I_A/I_S) yields

$$\frac{I_A}{I_S} = \frac{(\nu_0 + \nu_{nk})^4}{(\nu_0 - \nu_{nk})^4} e^{-h\nu_{nk} / kT},$$

which is in accord with experiment.

The Raman effect is slightly different in gases, liquids, and solids, due to the nature of the allowed oscillations for each physical state. Higher order Raman interactions between the incident

electric field and polarizability also exist, as do resonance effects, which occur near the frequencies of the electronic and vibrational transitions. Particularly pertinent to this study is the treatment of Raman scattering in crystalline solids, which behave quite simplistically due to their high levels of order and symmetry.

Raman Scattering in Single Crystals

Single crystals are highly-ordered solids composed of a single unit cell repeated over and over. Vibrations of the crystal lattice give rise to Raman scattering, with normal modes of oscillation displacing different portions of the lattice against each other, giving up and absorbing energy. The origin of these normal oscillations, referred to as *optic modes*, may be demonstrated using the simple example of a one-dimensional chain of atoms.

One-Dimensional Chain Lattice Consider an infinite one-dimensional chain of atoms. The even and odd numbered atoms have masses M_1 and M_2 , respectively and identical atoms are separated by a distance a when they are at rest. If the oscillations are considered harmonic, the equations of motion of the $2n^{\text{th}}$ and $(2n+1)^{\text{th}}$ atoms are

$$M_1 \ddot{x}_{2n} = \beta(x_{2n+1} + x_{2n-1} - 2x_{2n}),$$

$$\text{and } M_2 \ddot{x}_{2n+1} = \beta(x_{2n+2} + x_{2n} - 2x_{2n+1}),$$

where x_n denotes the displacement of the n^{th} atom and β is the linear restoring force. If the displacements are assumed to be periodic in time and position, the solutions are

$$x_{2n} = A e^{i2nKa' - i\omega t},$$

$$\text{and } x_{2n+1} = B e^{i(2n+1)Ka' - i\omega t},$$

where $a' = a/2$ is the nearest neighbor distance, ω is the periodicity in time, and K is the wavevector, or periodicity in space.

When the values for x_{2n} and x_{2n+1} are plugged into their corresponding differential equations, a bit of algebra yields the relations for ω^2 and the ratio A/B :

$$\omega^2 = \frac{\beta(M_1 + M_2)}{M_1 M_2} \left(1 \pm \sqrt{1 - \frac{4M_1 M_2 \sin^2(Ka')}{(M_1 + M_2)^2}} \right),$$

$$\text{and } \frac{A}{B} = \frac{2\beta - M_2 \omega^2}{2\beta \cos(Ka')}.$$

A plot of ω vs. K , called the *phonon dispersion relation*, provides a graphic representation of the different modes in a crystal. Since $\sin^2(Ka') = \sin^2(Ka' + \pi)$, it is sufficient to plot ω vs. K for $-\pi/2a' < K < \pi/2a'$ or, in terms of the identical atom spacing, $-\pi/a < K < \pi/a$. This region of wavevector space is called the first Brillouin zone.

In the case where M_2 is greater than M_1 , ω has two branches -- an upper branch corresponding to the plus sign and a lower one corresponding to the minus sign. The phonon dispersion relation for the one-dimensional lattice is shown in Figure 1.4 [14]. Note that as $K \rightarrow 0$, the upper and lower branches approach their maximum and minimum values, respectively.

For the lower branch, $A/B = 1$ at $K = 0$. This implies that neighboring atoms are displaced an equivalent amount in the same direction, so that the center of mass is not fixed, but moves with the oscillation. This translational motion of the entire lattice resembles the behavior of sound waves, and the branch is consequently called an *acoustic* branch.

For the upper branch, the ratio $A/B = -M_2/M_1$ at $K = 0$. Since $x_{2n}/x_{2n+1} = (A/B) e^{-iKa'}$, this implies that neighboring atoms are displaced in opposite directions, vibrating against each other about a fixed center of mass. If the atoms are oppositely charged, this type of vibration may occur when electromagnetic radiation is incident on the sample. This branch is correspondingly called an *optical* branch.

Three-Dimensional Lattices When all three dimensions of a crystal are taken into account, the normal oscillations may again be divided into optical and acoustical modes. If there are n atoms in a unit cell of a crystal, a total of $3n$ modes will arise from that cell, with three acoustical and $3n-3$ optical modes. The optical modes may be further divided into oscillations of the molecular units as a whole, called *lattice* modes, and oscillations of the atoms within the molecular units, called *internal* modes. The frequencies of the lattice modes are usually small, while those of the internal modes may be relatively large.

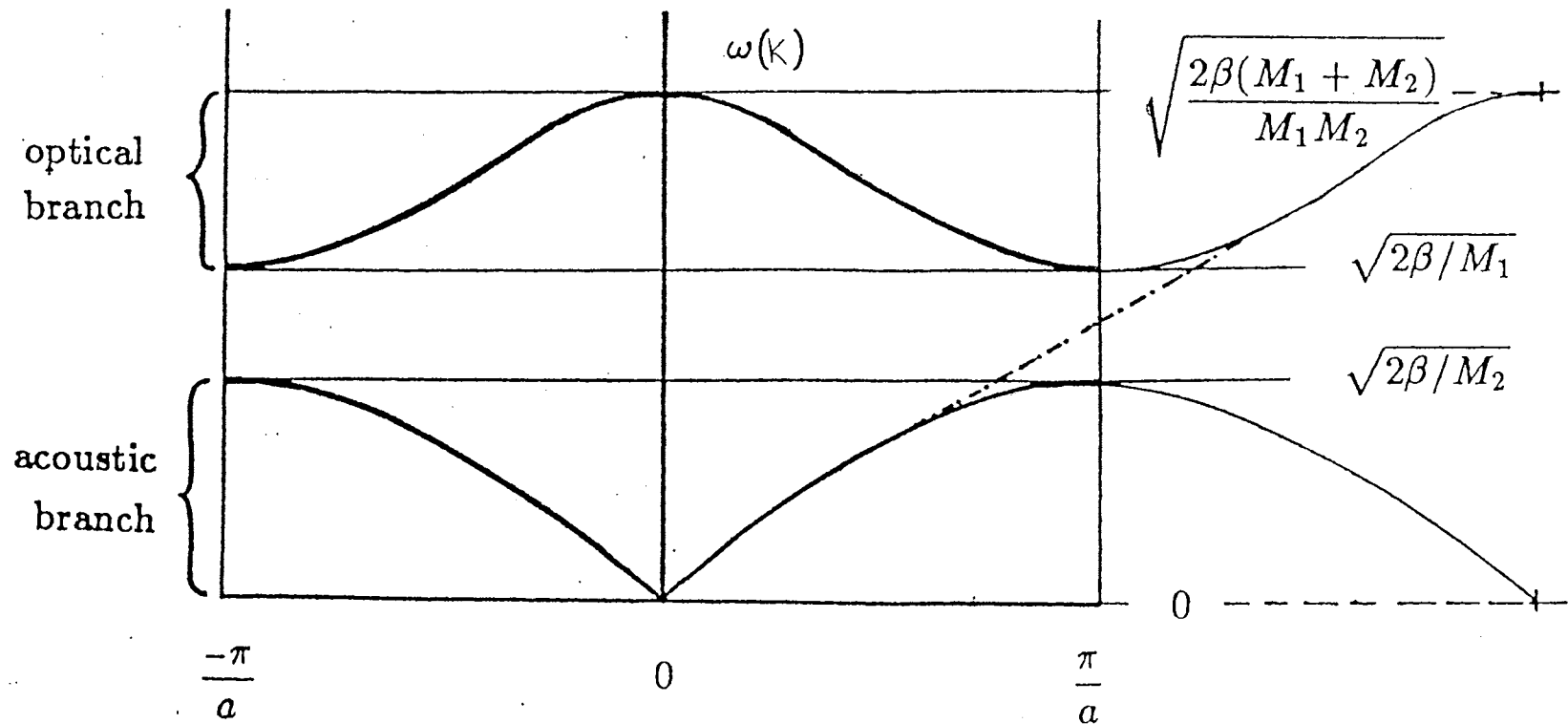


Figure 1.4. Phonon dispersion curves for a one-dimensional chain lattice with two types of atoms. Masses M_1 and M_2 are defined such that $M_2 > M_1$. The frequencies at $K = 0$ and $\pm \pi/a$ are given at the right side of the diagram (from Böer, 1990).

Since all equivalent lattice points in a crystal will have the same motion at a given instant in time, the spectral activity of the crystal may be determined from a single unit cell. The three acoustic modes of oscillation cannot induce a dipole moment in the crystal and therefore do not give rise to Raman scattering. The $3n-3$ optical modes, on the other hand, may or may not be Raman active, depending on whether or not the vibration causes a change in the induced dipole moment.

If two axes in a crystal are equal, a two-fold degeneracy will occur for all modes oscillating in the plane of symmetry. As a result, there will be two distinct acoustical modes and $2n-2$ distinct optical modes [15]. Likewise, in a cubic crystal, with three equal axes, there will be $n-1$ distinct optical modes. Thus, as the symmetry of a crystal increases, there are fewer distinct modes and more degeneracies.

In the particular case of diamond, the unit cell is face-centered cubic with a two atom basis. Since the three crystal axes are equal, there will be $2 - 1 = 1$ distinct optic mode. This triply degenerate optic mode is illustrated in Figure 1.5. The two atom basis forms two interpenetrating lattices, represented by white and black atoms. These two lattices oscillate against each other about the fixed center of symmetry, marked by the "x". Because this oscillation produces a change in the induced dipole it is Raman allowed.

Selection Rules for Raman Scattering in Crystals Although a lattice vibration cannot carry momentum, it will interact with photons as if its momentum were $\hbar\mathbf{K}$, called the *crystal momentum*. Thus, by the conservation of energy and momentum, two selection rules exist for crystals:

$$\omega_s = \omega_0 \pm \omega$$

$$\text{and } \mathbf{k}_s = \mathbf{k}_0 \pm \mathbf{K}.$$

The plus and minus signs represent anti-Stokes and Stokes scattering, while (ω_s, \mathbf{k}_s) , (ω_0, \mathbf{k}_0) , and (ω, \mathbf{K}) are the frequency and wavevector of the scattered photon, incident photon, and phonon, respectively. Those phonons with displacements along \mathbf{K} are denoted longitudinal, while those with displacements perpendicular to it are denoted transverse. Thus, of the three acoustical modes, two are transverse acoustical (TA) modes and one is a longitudinal acoustical (LA) mode. Similarly, two transverse optical (TO) modes exist for each longitudinal optical (LO) mode.

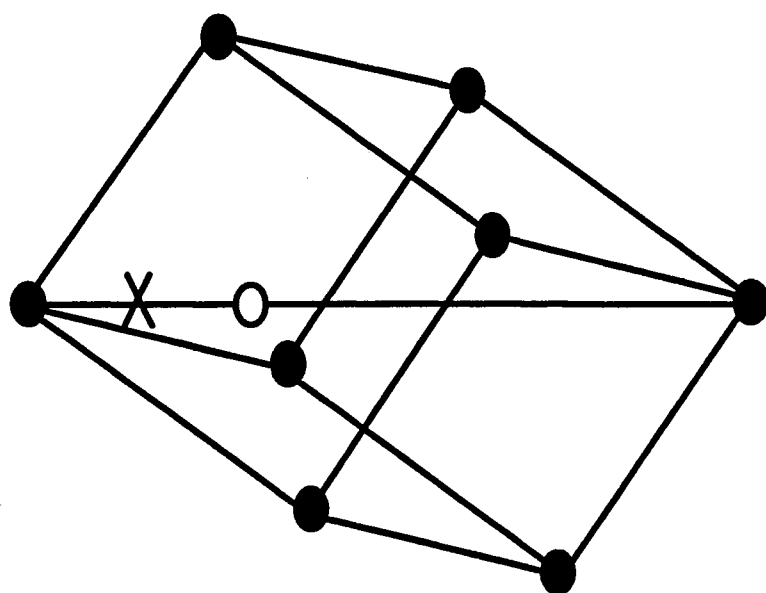


Figure 1.5. The single, triply-degenerate optic mode of diamond.

The wavevector, \mathbf{k} , and photon wavelength, λ , are related by the equation $|\mathbf{k}| = 2\pi/\lambda$ in free space and by $|\mathbf{k}| = 2\pi n/\lambda$ in the crystal, where n is the index of refraction of the crystal. The wavelength of the incident radiation is typically on the order of 10^{-4} cm, corresponding to a \mathbf{k} -vector on the order of 10^5 cm^{-1} . Since this is many orders of magnitude smaller than the first Brillouin zone ($\sim 10^8 \text{ cm}^{-1}$), all phonons will occur at $|\mathbf{K}| \approx 0$. In this region, the upper (optical) branch of the phonon dispersion curve is flat and the lower (acoustical) branch goes to zero. It is because of this that the optical modes of a crystal produce sharp Raman bands while the acoustic modes are Raman inactive.

The Effects of Anharmonicity on Raman Scattering in Solids

In the classical treatment, the N atoms in a crystal are approximated as masses attached by springs, displaced only slightly from their equilibrium positions so that the potential energy of the crystal may be expanded in a Taylor series about the equilibrium configuration:

$$V(q_1, q_2, \dots, q_{3N}) = \sum_{i,j}^{3N} f_{ij} q_i q_j + \sum_{i,j,k}^{3N} g_{ijk} q_i q_j q_k + \sum_{i,j,k,l}^{3N} h_{ijkl} q_i q_j q_k q_l + \dots$$

In this expression, f_{ij} , g_{ijk} , and h_{ijkl} are the quadratic, cubic, and quartic force constants in suitable units and q_i denotes a displacement from equilibrium, with q_n , q_{n+1} , and q_{n+2} respectively representing the x , y , and z displacements of the n^{th} atom. The quadratic sum represents purely harmonic motion, while the higher order terms give rise to thermal expansion, damping, and other anharmonic effects.

The origin of thermal expansion is most easily seen by considering the one-dimensional classical harmonic oscillator with potential energy

$$V(x) = fx^2 + gx^3 + hx^4,$$

where the quadratic, cubic, and quartic force constants are again given by f , g , and h , and x represents a displacement from the equilibrium position. The average displacement of the atom is given by

$$\langle x \rangle = \frac{\int_{-\infty}^{\infty} x e^{-V(x)/kT} dx}{\int_{-\infty}^{\infty} e^{-V(x)/kT} dx},$$

where the possible values for x have been weighted by the Boltzmann distribution function according to their thermodynamic probability [16]. By expanding the exponential to first order in a Taylor series and evaluating the integrals, we obtain

$$\langle x \rangle \approx \frac{3g}{4f^2} kT.$$

so that the thermal expansion coefficient to first order arises from the cubic potential energy term.

While the thermal expansion of the crystal is most easily seen classically, the origins of phonon damping and the temperature-dependent behavior of the vibrational modes of the crystal are more easily developed in a quantum mechanical approach to the problem. This is done by first making the transformation from Cartesian coordinates to normal coordinates, so that the Hamiltonian for the purely harmonic motion of the N atom crystal is given by

$$H = \frac{1}{2} \sum_k^{3N} \dot{Q}_k^2 + \frac{1}{2} \sum_k^{3N} \omega_k^2 Q_k^2$$

where ω_k is the frequency of oscillation of the k^{th} normal coordinate, Q_k , and the energy and momentum selection requirements are assumed to be fulfilled in this and all subsequent equations.

This expression, derived in Appendix C, may be converted into the quantum mechanical energy representation by writing the Q_k 's and \dot{Q}_k 's in terms of the creation and annihilation operators a_k^+ and a_k :

$$Q_k = \sqrt{\frac{\hbar}{2\omega_k}} (a_k + a_k^+) \quad \text{and} \quad \dot{Q}_k = i\sqrt{\frac{\hbar\omega_k}{2}} (a_k^+ - a_k).$$

Upon making this substitution and using the commutation relation $[a, a^+] = 1$, the Hamiltonian becomes

$$H = \sum_k^{3N} \left(a_k^+ a_k + \frac{1}{2} \right) \hbar\omega_k$$

which has eigenstates of the form

$$|\Psi\rangle = |n_1, n_2, \dots, n_{3N}\rangle,$$

and energy eigenvalues

$$E = \sum_k^{3N} \left(n_k + \frac{1}{2} \right) \hbar\omega_k.$$

Since phonons are bosons, the occupation numbers n_k of the vibrational modes are given by the Bose-Einstein distribution function,

$$n_k = (e^{\hbar\omega_k / kT} - 1)^{-1},$$

so that at higher temperatures, all of the normal modes contain larger numbers of phonons. These energy levels are discrete, but may be degenerate if two or more vibrational modes have the same frequency.

By now including higher order terms from the Taylor series potential energy expression, the effects of thermal broadening and shifting may be accounted for. Assuming the anharmonic terms are much smaller than the harmonic ones, they may be treated as perturbations on the harmonic energy solutions. In the method of time-dependent perturbation theory [17], the eigenstates are explicit functions of time:

$$|\Phi(t)\rangle = \sum_i c_i(t) |\Psi_i(t)\rangle = \sum_i c_i(t) |n_1, n_2, \dots, n_{3N}\rangle_i$$

and the Hamiltonian is given by

$$\begin{aligned} H = H_0 + H' = & \sum_k \left(a_k^+ a_k + \frac{1}{2} \right) \hbar\omega_k + \sum_{ijk} b_{ijk} (a_i + a_i^+) (a_j + a_j^+) (a_k + a_k^+) \\ & + \sum_{ijkl} c_{ijkl} (a_i + a_i^+) (a_j + a_j^+) (a_k + a_k^+) (a_l + a_l^+) \end{aligned}$$

where the sums respectively give the harmonic, cubic, and quartic contributions to the energy. Using the time-dependent Schroedinger equation,

$$H|\Phi(t)\rangle = i\hbar \frac{\partial}{\partial t} |\Phi(t)\rangle,$$

the coefficients $c_n(t)$ of the energy eigenvectors are found to be

$$\dot{c}_n(t) = -\frac{i}{\hbar} \sum_i c_i(t) H'_{ni} e^{i\omega_{ni}t},$$

$$\text{where } \omega_{ni} = \frac{E_n - E_i}{\hbar}$$

$$\text{and } H'_{ni} = \langle \Psi_n(0) | H' | \Psi_i(0) \rangle.$$

In continuing, we now suppose that the system is in a definite eigenstate of H_0 at time $t = 0$ and that the only state to which it can go is m . With these restrictions and again assuming the fulfillment of

the energy and momentum selection rules,

$$c_n(0) = 1,$$

$$c_{i \neq n}(0) = 0,$$

$$\langle \Psi_n(0) | H' | \Psi_m(0) \rangle \neq 0,$$

$$\text{and } \langle \Psi_i(0) | H' | \Psi_j(0) \rangle = 0 \text{ (} i, j \neq n \text{)}.$$

There are only two coefficients which have non-zero time derivatives:

$$\dot{c}_n(t) = -\frac{i}{\hbar} c_m(t) H'_{nm} e^{i\omega_{nm}t}$$

$$\text{and } \dot{c}_m(t) = -\frac{i}{\hbar} c_n(t) H'_{mn} e^{i\omega_{mn}t}.$$

If the probability of finding the system in state $|\Psi_n(0)\rangle$ decreases exponentially like $e^{-\gamma t/2}$, where γ is effectively a decay constant, the expression for $\dot{c}_m(t)$ may be integrated from 0 to t to yield $c_m(t)$:

$$c_m(t) = -\frac{i}{\hbar} \frac{H'_{mn} (e^{(i\omega_{mn} - \gamma/2)t} - 1)}{(\omega_{mn} - \gamma/2)}$$

Plugging this expression into the above expression for $c_n(t)$, with $\dot{c}_n(t) = (-\gamma/2)e^{-\gamma t/2}$, the resulting equation reveals that γ is a complex function of time.

Letting $\gamma = \gamma' + i\gamma''$, the probability that the system will have made the transition from $|\Psi_n(0)\rangle$ to $|\Psi_m(0)\rangle$ in a time t is given by

$$|c_m(t)|^2 = \frac{|H'_{mn}|^2}{\hbar^2} \frac{e^{-\gamma' t} - e^{-\gamma' t/2} \cos[(\omega_{mn} - \gamma''/2)t] + 1}{(\omega_{mn} - \gamma''/2)^2 + (\gamma'/2)^2}.$$

At $t = \infty$, the transition probability becomes

$$|c_m(\infty)|^2 = \frac{|H'_{mn}|^2}{\hbar^2} \frac{1}{(\omega_{mn} - \gamma''/2)^2 + (\gamma'/2)^2}$$

The real and imaginary parts of the decay constant may be found by explicitly evaluating the expression for $\dot{c}_n(t)$. However, this equation must be altered slightly, since the time dependence of γ suggests that the eigenstate $|\Psi_m(0)\rangle$ is not discrete, but rather includes a time varying continuum of energies. The adjusted equation for $c_n(t)$ is then

$$c_n(t) = -\frac{i}{\hbar} \int c_m(t) H'_{nm} e^{i\omega_{nm}t} dm$$

which becomes, upon plugging $c_m(t)$ and $\dot{c}_n(t) = (-\gamma/2)e^{-\gamma t/2}$ in,

$$\gamma = \frac{2i}{\hbar^2} |H'_{mn}|^2 \int \frac{(1 - e^{[i\omega_{nm} + \gamma/2]t})}{(\omega_{nm} - i\gamma/2)} dm$$

When the decay rate γ is much smaller than ω_{nm} , this becomes

$$\gamma \approx \frac{2}{\hbar^2} |H'_{mn}|^2 \int \frac{[(\sin \omega_{nm}t) + i(\cos \omega_{nm}t)] \rho(\omega_{nm})}{\omega_{nm}} d\omega_{nm}$$

where $\rho(\omega_{nm}) = (dm/d\omega_{nm})$ is the density of phonon states with frequency ω_{nm} .

In the limit as t goes to infinity, we get

$$\gamma' = \frac{2\pi}{\hbar^2} |H'_{nm}|^2 \rho(\omega_{nm})$$

$$\text{and } \gamma'' = \frac{2}{\hbar^2} P \int \frac{|H'_{nm}|^2 \rho(\omega_{nm})}{\omega_{nm}} d\omega_{nm},$$

where P denotes the principal part of the integral. By redefining $\gamma'/2 = \Gamma$ and $\gamma''/2 = \Delta$ and substituting these expressions into the above result for $|c_m(\infty)|^2$, the probability of the transition from $|\Psi_n(0)\rangle$ to $|\Psi_m(0)\rangle$ becomes

$$|c_m(\infty)|^2 = \frac{\Gamma}{\pi[(\omega_{nm} - \Delta)^2 + \Gamma^2]}$$

This result is clearly Lorentzian, with the real part of γ , Γ , giving the vibrational mode a finite line width and the imaginary part, Δ , producing a shift in the vibrational frequency. Provided that the given mode is Raman active, these effects will show up in the spectrum as an increase in the Raman peak width and a shift in the position of the peak maximum. As the anharmonic phonon interactions are reduced to zero, γ vanishes and the transition probability reduces to a delta function, agreeing with the result obtained for purely harmonic motion.

Since the operators a and a^+ acting on the $|\Phi(t)\rangle$ yield expressions containing the Bose-Einstein distribution function, $n_k = (e^{\hbar\omega_k/kT} - 1)^{-1}$, and these are contained in Γ and Δ through the $|H'_{mn}|^2$ terms, both the width and the position of the Raman peak are temperature dependent. Since the $|H'_{mn}|^2$

terms are always non-negative, Γ and $|\Delta|$ will both increase with temperature, though the direction of the frequency shift depends on the signs of ω_{nm} and Δ .

While the cubic terms in the potential energy do not shift the vibrational frequency, the quartic terms and cubic terms to second order do. This can be seen by examining the contributions to the Hamiltonian from the cubic and quartic potential energy terms:

$$H_{\text{cubic}} = \sum_{ijk} b_{ijk} (a_i + a_i^+)(a_j + a_j^+)(a_k + a_k^+),$$

$$\text{and } H_{\text{quartic}} = \sum_{ijkl} c_{ijkl} (a_i + a_i^+)(a_j + a_j^+)(a_k + a_k^+)(a_l + a_l^+).$$

All combinations of operators which raise and lower the occupation number of all the involved phonon modes an *equal* number of times will contribute to the diagonal matrix elements of the Hamiltonian. Since the cubic terms have an odd number of raising and lowering operators, they cannot raise and lower equally and therefore only occur in the off-diagonals.

An arbitrary 2x2 matrix which includes small perturbations ε_3 and ε_3' from the cubic terms and perturbations $\varepsilon_4, \varepsilon_4', \varepsilon_4'', \varepsilon_4'''$ from the quartic terms, is given by

$$\begin{vmatrix} V + \varepsilon_4 - \lambda & \varepsilon_3 + \varepsilon_4' \\ \varepsilon_3' + \varepsilon_4'' & V' + \varepsilon_4''' - \lambda \end{vmatrix} = 0.$$

This determinant may be clearly seen to have energy eigenvalues shifted to first order by only the diagonal contributions from the quartic terms. The off-diagonal terms, both cubic and quartic, shift the energy eigenvalues only through second order effects.

The constants f_{ij} as well as the other force constants in the potential energy expression, are affected by the presence of defects, imperfections, and boundaries within the crystal lattice. These entities cause localized strains in the lattice which, through the force constants, shift the frequencies of oscillation of the normal modes of the crystal. The magnitude and direction of the frequency shift for a given vibrational mode in a *single* unit cell of the crystal depends on the changes in the force constants affecting that particular unit cell. Since each unit cell may be perturbed differently, depending on the type and size of localized strains present in that cell, the Raman spectrum of the *entire* crystal shows a *distribution* of

vibrational frequencies for the given normal mode, with the width of the peak broadened by the variations in strain between the different units cells. The net strain on the crystal may be determined from the maximum of the Raman peak. A lowering of frequency is caused by net tensile stress and an increase is caused by net compressive stress. The magnitude of the frequency shift is proportional to the amount of strain present, which is on the order of $(-10^{10} \text{ dyn/cm}) \times (\Delta v_s(\text{cm}^{-1}))$ for diamond [18]. Of course, the more similar the unit cells of the lattice are, regardless of the net strain present, the narrower the energy distribution will be.

In addition to the temperature-dependence of the vibrational modes which arises from the anharmonic interactions in the potential energy expression, there is an additional temperature dependence which occurs when the harmonic force constants are dependent on the volume of the crystal. In this case, the anharmonic contributions which cause the vibrational frequencies to shift and also give rise to the thermal expansion of the lattice indirectly cause the vibrational frequencies to shift an additional amount due to the changes in the harmonic force constants. The Grüneisen parameter, γ , has been developed to account for this volume-dependent frequency shift, where the Grüneisen parameter of the i^{th} vibrational mode, γ_i , is defined as

$$\gamma_i = -\frac{V}{\omega_i} \frac{d\omega_i}{dV}$$

[19]. This unitless parameter provides a measure of the frequency shift due entirely to changes in the crystal volume.

Summary of Thesis

In this study, the effects of laser annealing on CVD diamond grains are investigated using micro-Raman spectroscopy and scanning electron microscopy. This research is motivated by the discovery of significant heating of CVD diamond grains upon exposure to 514.5 nm laser light, as evidenced by severe downshifting of the Raman diamond peak at increasingly higher laser powers. This effect is considered in conjunction with the results of two furnace annealing studies which have shown diamond films to be drastically improved after annealing.

Surprisingly, there is a great lack of awareness in current CVD diamond literature of the sensitivity of diamond grains to laser heating and/or the sensitivity of Raman spectra to temperature changes. On several occasions, papers have reported diamond peaks severely downshifted from the position of natural diamond [20-23], but have given either inadequate or incorrect explanations for the shift. In these papers, the shift is attributed either to massive strains in the diamond lattice or the growth of lonsdaleite, a hexagonal form of sp^3 -bonded carbon, rather than diamond. The strong temperature-dependence of the diamond peak was realized a paper too late by the present author, who attributed sharp ($\sim 5 \text{ cm}^{-1}$) Raman peaks at 1320 cm^{-1} to lonsdaleite in a previous paper [23] which were later determined to be diamond peaks downshifted by laser heating.

The responsiveness of CVD diamond grains to laser exposure, due to the presence of impurities and defects in the diamond lattice, which may decrease both the transparency and thermal conductivity of the grains, may provide a means of altering grains in a positive way. Uchida *et al.* [24] have reported that CVD diamond films post-etched in an oxygen atmosphere at 800°C are dramatically improved, as the process selectively removes disordered sp^2 and sp^3 carbon bonds from the diamond lattice. Additional research by the author of the present paper has shown that the band gaps and transmission coefficients of CVD diamond films become significantly larger and more like those of natural diamond after annealing in nitrogen in a tube furnace at 700°C [25].

While furnace annealing may provide a practical way of improving diamond coatings on optics, the possibility of laser annealing diamond grains may be more practical, since this method would allow more precise control. By laser annealing samples, *microscopic* regions of diamond could be selectively improved while generating minimal substrate heating. The most obvious application of this technique is in the microchip industry, where high precision is required.

In summary, the present paper provides an account of the successful improvement of diamond grains by laser annealing, where conditions similar to those in furnace annealing studies have been produced by exposing grains to a variable-power laser beam in the atmosphere. As grains become laser-heated to appropriate temperatures, they are seen to improve significantly in quality, as determined by

reductions in the linewidth of the Raman diamond peak. SEM photographs reveal mass loss with annealing, suggesting that impurities and defects are selectively removed from the diamond lattice, as seen to occur in furnace annealing.

Studies of the silicon substrate beneath diamond grains have shown that the silicon is not affected by the conversion process. However, the reflection of thermal phonons at the interface between the diamond and silicon is seen to increase after annealing. As a result, it is ventured that an interface, most probably silicon carbide, is present between the two materials. The existence of this layer is supported by tube furnace annealing studies and comparisons between regular and nitrogen-doped diamond, also produced in this study.

SEM photographs of grains taken before and after laser and tube furnace annealing show that the distributions of defects and impurities within grains vary with grain morphology. By combining these SEM observations with the results of the Raman data, two models have been proposed to explain the conversion process. The thesis concludes with a chapter on the applications of laser annealing and suggestions for future research.

CHAPTER II

SAMPLE PRODUCTION AND ANALYSIS

Background

Chemical vapor deposition is defined by Pierson as "the deposition of a solid on a heated surface from a chemical reaction in the vapor phase" [26]. The CVD process is essentially the same for all materials: high energy is supplied to initiate reactions, either by thermal means or by interaction with a plasma, and then a driving force, such as a temperature gradient or an electric field, transports the reactants to a heated substrate, where, if conditions are favorable, the reactants will be deposited on the substrate in solid form. In the specific case of diamond CVD, at least one carbon-containing gas must be used, as must some gas which etches graphite and/or suppresses its formation. Substrates should be near the solubility limit of carbon, so that carbon atoms will form diamond on the surface, rather than diffusing into the substrate [4].

Typical CVD conditions for diamond include an input gas mixture of molecular hydrogen with 0.1 to 2.0% methane (CH_4), flowing at a total rate of 100 standard cubic centimeters per minute (sccm), a substrate temperature between 600 and 1100°C, and a pressure of 1 to 100 Torr. Deposition times range anywhere from 15 minutes to more than 24 hours and appropriate substrates currently include silicon, molybdenum, and most carbides. Studies of films at different times during deposition have shown that the development of crystalline carbon films takes place in two stages: nucleation and growth.

Nucleation

As stipulated by thermodynamic theory, the free energy of a reaction must be negative if it is to occur. Nucleation occurs with the formation of critically-sized carbon structures on the substrate surface,

large enough that the contributions between volume and surface energies balance [27]. The contribution of bond formations between atoms in the nucleus is negative, while the corresponding contribution of the surface, due to bond strains and unsatisfied valencies is positive [28]. Thus, until the nuclei reach their critical size, they will be unstable.

Matsumoto *et al.* [29] have suggested that sp^3 bonded multiply-twinned hydrocarbon cage compounds with six-membered carbon rings, like adamantane, bicyclo [2.2.2] octane, tetracyclo [4.4.0.1.1] dodecane, hexacyclo [5.5.1.1.1.0.0] pentadecane, and dodecahedrane could function as nuclei [28, 29]. These compounds, shown in Figure 2.1, are not normally stable at typical diamond CVD temperatures, but may be stabilized by the supersaturation of carbon and atomic hydrogen long enough to form critical nuclei [28]. Those nuclei that do not obtain critical size are absorbed by other nuclei or dissociate.

The nucleation of diamond on non-diamond surfaces may be enhanced by scratching, carbon coating, and seeding with diamond particles [10]. Scratching with diamond or other abrasives has been found to increase the number of nucleation sites, either by leaving a residue of diamond seeds or by mechanically damaging the sample, creating high energy damage sites on the surface [30]. Covering the substrate with carbon-containing species also enhances nucleation, saturating the surface with carbon [10] and/or reducing stress by improving the lattice match [28].

An incubation period has been observed before the onset of nucleation on many substrates. Within this period, carbide and amorphous carbon (a-C) layers were found to form [10, 28, 31, 32, 33], growing rapidly at first, more slowly as the carbide or a-C layer thickened, and almost completely stopping at the first appearance of diamond [31]. An interesting observation made by Williams *et al.* [32, 33] is that different intermediate layers, i.e. carbides or a-C, can be produced on the same substrate by different gas phase compositions. The duration of the carbide or a-C formation period seems dependent on the carbon diffusion rate of the substrate, which is directly related to the carbon surface saturation. The process continues until a critical surface carbon concentration is attained, which is necessary for the formation and survival of stable nuclei.

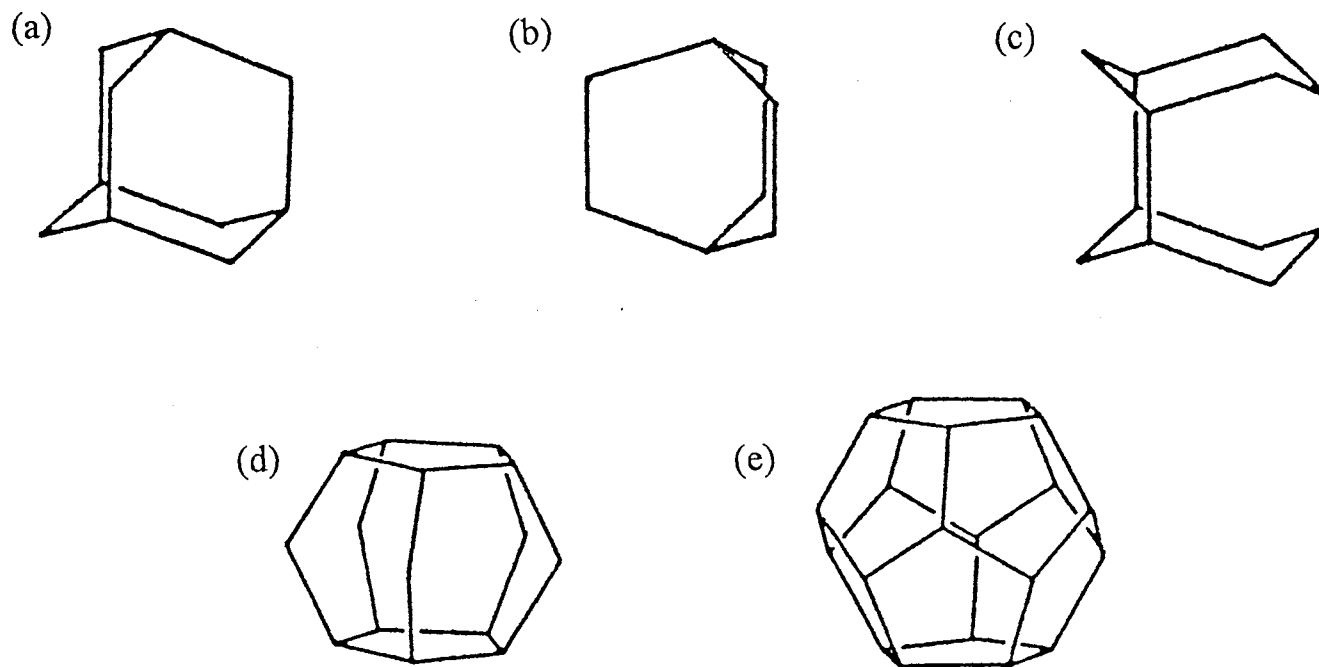


Figure 2.1. Hydrocarbon cage compounds with six-membered carbon rings which could function as nuclei for diamond crystal formation. (a) adamantane, (b) bicyclo [2.2.2] octane, (c) tetracyclo [4.4.0.1.1] dodecane, (d) hexacyclo [5.5.1.1.1.0.0] pentadecane, (e) dodecahedrane.

Growth

Once the saturation level of nucleation is reached, the stable nuclei on the substrate coarsen and become more faceted, often exhibiting a preferred orientation [34]. This orientation is initially related to the ratio of the total surface energy to volume energy, since a balance in positive and negative energies is required for formation [35]. The lowest ratio is for octahedra, composed of (111) crystallographic planes [35]. As growth progresses, the most important quantity becomes the ratio of surface area to volume, which is lowest for cubo-octahedra. Thus, grains most frequently begin as octahedra and grow into cubo-octahedra over time. The relationship between octahedra, cubes, and cubo-octahedra is illustrated in Figure 2.2.

The morphology and growth rate of diamond films are greatly affected by changes in methane concentration. According to Yarbrough and Messier, (111) faces shift to (100) faces as methane concentrations are increased from 0.2 to 2.0% [22], while (100) faces prevail for methane concentrations of 2 to 6% [22, 36]. The smoothest (100) faces occur at 6% methane, while films become microcrystalline with methane concentrations greater than 7% [22, 36]. The growth rate is reported to increase as methane concentration approaches 5%, although it decreases for higher methane levels, with sp^2 carbon formation inhibiting the growth of diamond [36].

The relationship between methane concentration and the presence of non-diamond structures has been determined in a study by Zhu *et al.* [37]. No graphite or other non-diamond components were found at a methane concentration of 0.5%, while a methane concentration of 2% produced highly oriented graphite crystallites on or near the {111} diamond planes. At 5% methane, graphite crystallites were randomly distributed and, as the methane concentration increased, so did the density of defects like stacking faults and twins on the {111} diamond planes.

The flow rate of the reactants has been found by Celii *et al.* [11] to strongly affect orientation and film quality. At flow rates of 100 and 200 sccm, dominant (100) and (111) facets were respectively grown on silicon. Diamond films grown on a layer of microcrystalline diamond had dominant (100) faces at 200

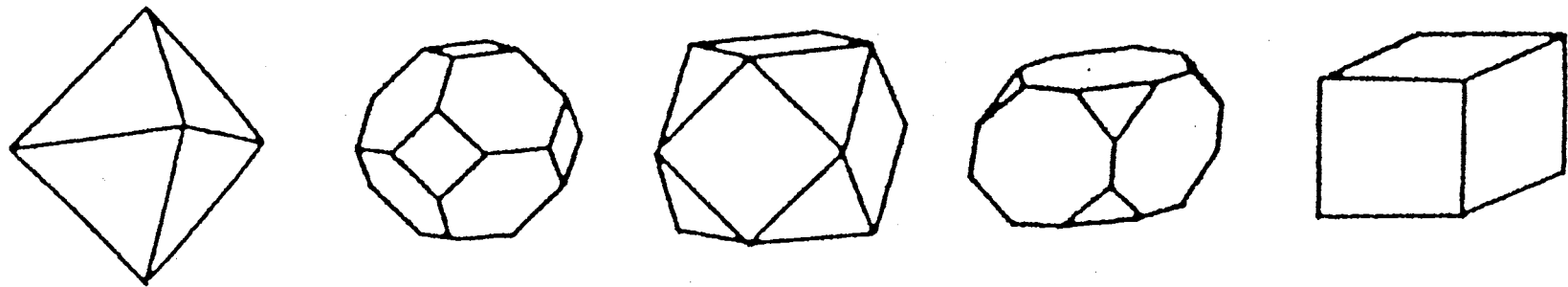


Figure 2.2. Octahedral, cubo-octahedral, and cubic crystal morphologies. The cubo-octahedron (center) is a combination of the octahedron (far left), constructed of eight $\{111\}$ planes, and the cube (far right), constructed of six $\{100\}$ planes.

sccm, but at other flow rates appeared to have only random distributions. On some occasions, films displayed small pyramidal grains, indicative of growth on the (110) planes. Highest quality films were produced at 400 sccm on silicon and at 100 sccm on microcrystalline diamond. The dependence of morphology and quality on flow rate may actually be dependent on the gas residence time, either by changing the reactant concentration, or the surface reaction time.

There is a narrow range of temperature over which single-phase diamond will grow, according to Yarbrough [22] and Badzian [27]. At temperatures of less than 800°C, a large amount of a-C is co-deposited, while temperatures over 1100°C promote the growth of graphite and a-C. In both instances, only fine grained films with no distinguishable faces were found [22]. 1000°C is reported as the temperature of best crystal quality and highest growth rate [27, 38], although the optimum nucleation temperature is reported to be 925°C [38]. At the higher and lower ends of the optimum temperature range, films display highly-faceted cubic and octahedral surfaces, respectively [27].

Several studies have been undertaken to determine the growth mechanisms involved in diamond CVD. The principal species detected by both in situ and ex situ analysis in environments which employ only hydrogen and methane source gases are molecular and atomic hydrogen (H_2 and H^+), methane (CH_4), methyl radicals (CH_3^+), acetylene (C_2H_2), and ethylene (C_2H_4), although ethane (C_2H_6) and hydrocarbons with three or more carbons have also been detected [28]. Kinetic models have confirmed the major species present and suggest that the dominant carbon growth species are most likely CH_4 , CH_3^+ , and C_2H_2 [28, 39].

The addition of oxygen to the CVD system has been found to increase the quality and growth rate of diamond films by reducing the concentration of unsaturated hydrocarbons, like C_2H_2 [40, 41]. As a result, the deposition of graphitic and a-C is suppressed, since the concentration of C_2H_2 is strongly related to their formation [41]. The rate of diamond growth increases with the addition of oxygen, for the total number of methyl radicals can be increased by increasing the flow rate or pressure [41]. Studies by Uchida *et al.* [18, 42] have additionally determined that oxygen has an even stronger etching effect than hydrogen and still rather selectively etches non-diamond components faster than diamond.

Reported Raman Signatures of the Allotropes of Carbon

Since the allotropes of carbon all have unique structures, each also has its own characteristic Raman signature. As a result, the positions of the Raman peaks distinctly specify what forms of carbon are present in a sample. The full width of the Raman peaks at half maximum (FWHM) give a qualitative estimate of the crystal quality, since the width of the peak may be broadened by localized strains produced by defects and impurities. Previous studies by Bonnot [20], Schroeder *et al.* [43], and Buckley *et al.* [44] include information on peak positions and FWHM values for many of the allotropes of carbon. Table I summarizes the reported peak positions and widths of the crystalline forms of carbon relevant in this study.

Diamond The Raman spectrum of natural diamond has a single Raman peak at 1332.5 cm^{-1} due to its fourfold coordinated sp^3 bonding, with a FWHM of approximately 2 cm^{-1} . This is the single, triply degenerate mode discussed and illustrated in Chapter I. While naturally-occurring diamond contains only 1.1% ^{13}C [45], synthetically-produced diamond may be doped with varying percentages of the isotope. This doping causes a downward shift in the vibrational energy, since the frequency of oscillation is inversely proportional to the square root of the mass. With a 15% ^{13}C concentration, the first-order diamond peak shifts to 1328 cm^{-1} , and with a 36% ^{13}C concentration, the peak is shifted to 1318.6 cm^{-1} [20].

Disordered diamond has been found to show additional peaks at 1220 and 1140 cm^{-1} , due to zone-boundary phonons [44]. In this case, the domain size, d , is on the order of the phonon mean free path, inducing an uncertainty $\Delta k \sim 1/d$ in the phonon momentum. As seen from the phonon dispersion curves in Figure 2.3 [46, 47], the energy of the optical phonon branch of diamond has its maximum at the Brillouin zone center point, Γ . The uncertainty Δk in the phonon momentum causes a relaxation in the momentum selection rule, resulting in a broadened Raman peak downshifted to a lower energy, with 1220 and 1140 cm^{-1} corresponding to the frequencies at the L [111] and X [100] points at the surface of the first Brillouin zone.

TABLE I

SUMMARY OF RAMAN PEAK POSITIONS AND WIDTHS
FOR SEVERAL ALLOTROPES OF CARBON

Form of Carbon	Peak Position(s) (cm ⁻¹)	Peak Width(s) (cm ⁻¹)
natural diamond	1332.5	2
diamond with 15% ¹³ C	1328	2
diamond with 36% ¹³ C	1319	2
lonsdaleite on sawed diamond	1319	2.2
shock-induced lonsdaleite	1316 to 1325	30
graphite	1580	20
typical CVD diamond	1332	10 - 20
amorphous carbon	1355, 1580, sometimes 1470-1490	both broad very broad
diamond-like carbon	1300 to 1350, 1540 to 1580	both broad

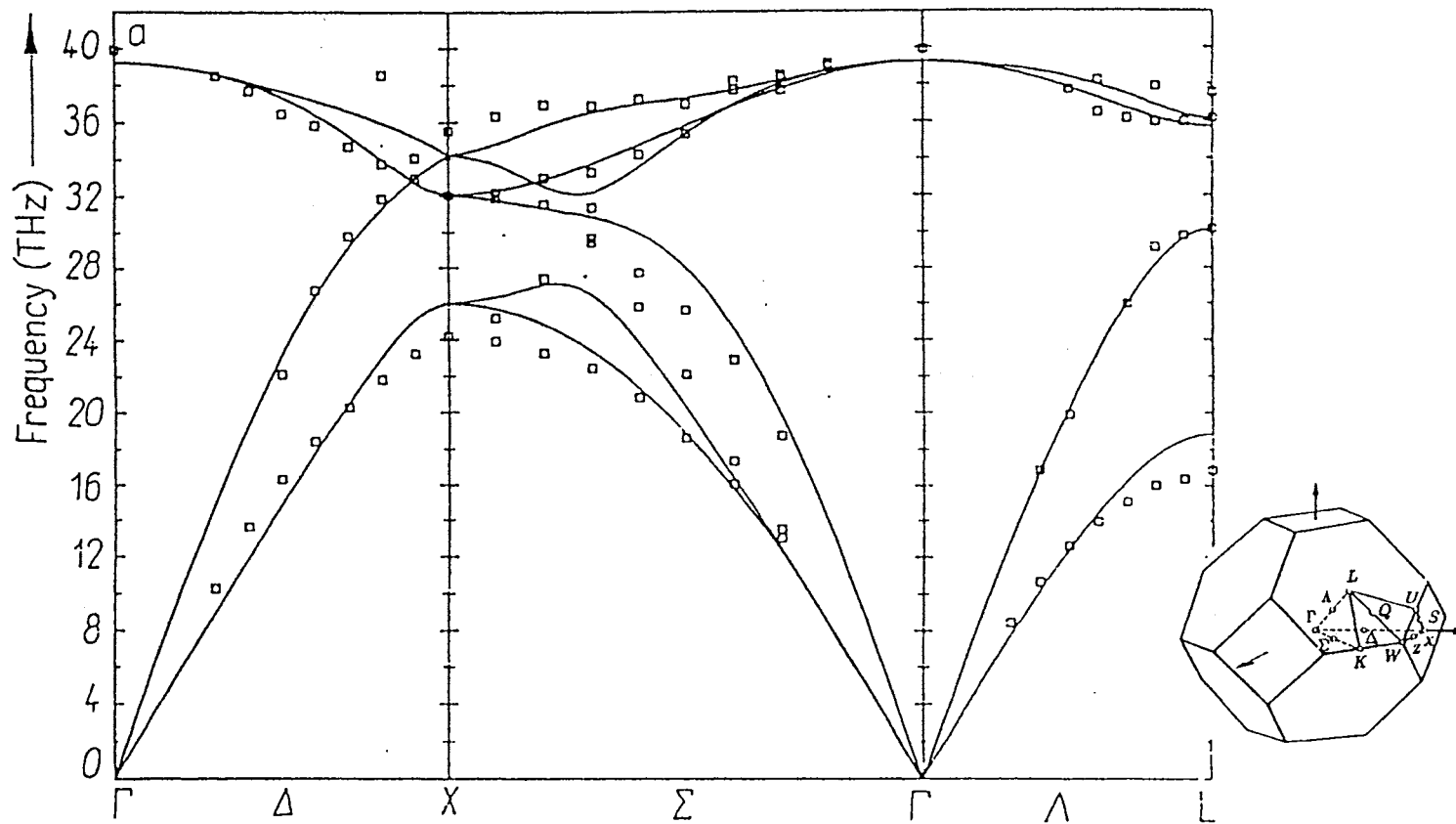


Figure 2.3. Phonon dispersion curves of diamond. The first Brillouin zone of the face-centered cubic lattice is also shown, with the important symmetry points Γ , X , L , Δ , Σ , and Λ marked (from Mohaupt, *et al.*, 1993, and Böer, 1990).

Lonsdaleite Lonsdaleite is a rare, non-naturally occurring form of carbon found only in meteorites and in quickly-formed synthesized crystalline carbon products. In one study, the Raman spectra of shock-induced high pressure lonsdaleite powder was found to display a broad peak centered between 1315 and 1326 cm^{-1} , with a half-width of 30 cm^{-1} [20]. In another study, lonsdaleite formed on the sawed surface of a ballas diamond was reported to produce a sharp peak at 1319 cm^{-1} with a FWHM of 2.2 cm^{-1} [48].

As is evident by their quite comparable Raman signatures, lonsdaleite and diamond are very similar in structure. Lonsdaleite is often called "hexagonal diamond" because of its hexagonal lattice of sp^3 bonding. It is composed of six-membered carbon rings identical to those along the {111} direction of diamond, with each atom tetrahedrally bonded to four others. Lonsdaleite differs from diamond, however, in that planes are stacked in the ABAB sequence, rather than the ABCABC sequence of diamond [28]. In this "boat" configuration, atoms in every other layer are eclipsed instead of staggered, giving lonsdaleite a higher energy configuration than diamond which attributes to its infrequent formation [28].

Graphite and Amorphous Carbon Perfect graphite, hexagonal in structure, is found to have a first-order Raman peak at 1580 cm^{-1} with a FWHM of roughly 20 cm^{-1} . This peak is due to in-plane displacements of trigonally-bonded atoms in the basal planes. The graphite peak is seen to broaden and shift to lower energies with increasing amounts of bond-angle disorder between atoms in sp^2 sites, with the peak maximum moving from 1580 cm^{-1} down to 1550 cm^{-1} [44].

When graphite forms too quickly, highly disordered microcrystalline graphite results. Also known as amorphous carbon (a-C), this form of graphite has the trigonal sp^2 electronic configuration of normal graphite, but with very short-range order. Crystallites are small and randomly oriented, often exhibiting structural defects and sometimes containing small amounts of hydrogen. The Raman spectrum of a-C is composed of two broad bands at 1580 and 1355 cm^{-1} [20]. These peaks correspond respectively to the mode of perfect graphite and a disorder-induced breaking of symmetry within the crystal, with the intensity of the 1355 cm^{-1} band being inversely proportional to grain size [20]. An additional broad peak has been found to occur between 1470 and 1490 cm^{-1} on several occasions, with this peak thought to

correspond to graphitic carbon with even higher levels of bond-angle disorder than those which causes the 1540 cm^{-1} peak [49].

Diamond-like Carbon Like microcrystalline graphite, diamond-like carbon (DLC) is the result of an overly-quick crystallization of carbon atoms. In this form of carbon, extremely small crystallites exhibit predominantly tetrahedral sp^3 bonding, but also contain many defects and display sp^2 bonding at the grain boundaries. Diamond-like carbon has a Raman spectrum nearly identical to that of microcrystalline graphite with two very similar broad peaks. One peak, located between 1540 and 1580 cm^{-1} , is attributed to graphitic sp^2 bonding, and the other, located between 1300 and 1350 cm^{-1} , is due to carbon atoms in sp^3 sites.

DLC and a-C are most easily distinguished from one another by the specific location of the lower energy Raman peak. In graphite powders and a-C, this peak is always situated above 1350 cm^{-1} , as it originates from the distortion of the hexagonal graphite lattice near the crystal boundary. In DLC, this peak is typically at lower energies, closer to the diamond peak at 1332 cm^{-1} , since it is due to sp^3 bonding. The term "diamond-like" is appropriate for the blend of sp^3 and sp^2 bonding, because some desirable properties associated with diamond are present.

Experimental Details

Chemical Vapor Deposition

The method of filament-assisted CVD was chosen for diamond film production in this study because of its low cost and operational simplicity. This method has the advantage of allowing the establishment of large gradients in substrate temperature and carbon concentration, providing a wide variety of deposition conditions on a single sample. This diversity increases the likelihood that diamond will be produced on at least one region of the substrate, while it also reveals sensitivity to other carbon structures.

Apparatus The deposition chamber, shown in Figure 2.4, consisted of a silica glass cylinder twelve inches high, six inches in diameter, and three-fourths of an inch thick. The top and bottom plates

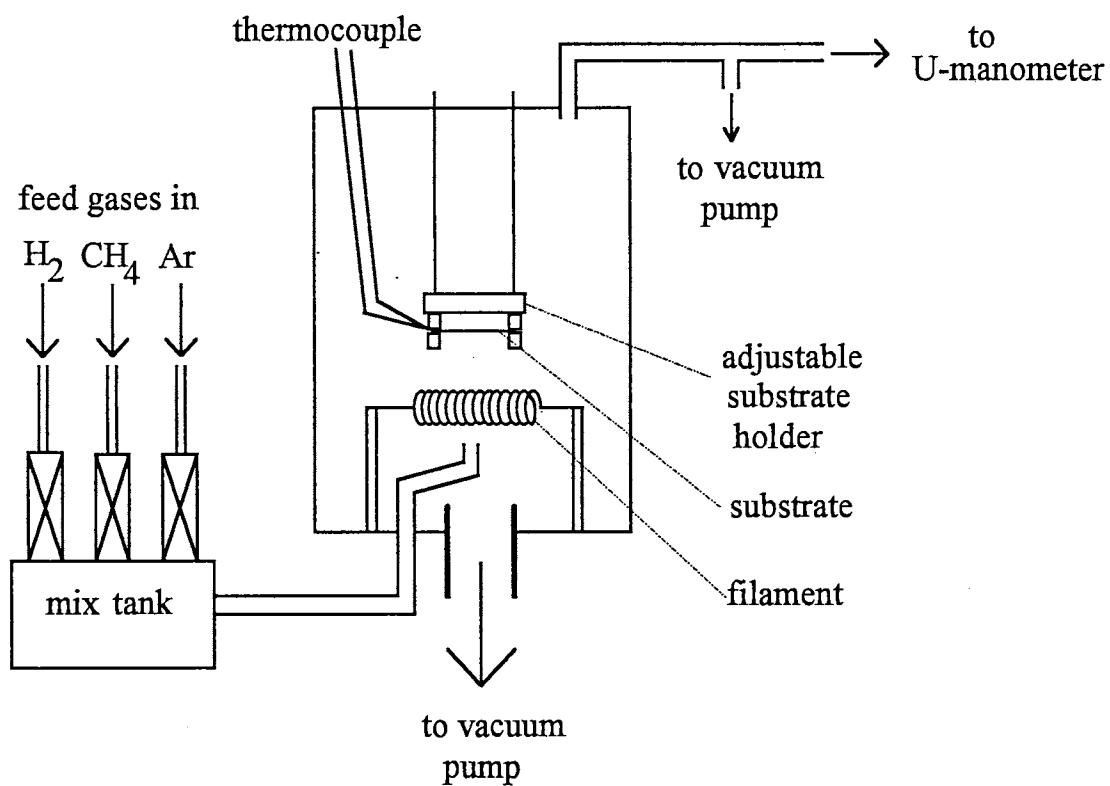


Figure 2.4. Filament-assisted chemical vapor deposition chamber used for sample production.

of the cylinder were made of stainless steel, with "O" rings sealing the chamber under pressure. A filament composed of three twisted 0.3 inch tungsten wires was clamped to two large copper electrodes connected to a step-down transformer, ammeter, and Variac voltage regulator.

A Leibold model 4-A rotary pump was attached to the deposition chamber by way of valves in both the upper and lower plates. The lower valve could be opened to a diameter of three inches and was used solely for the purpose of pumping out large quantities of gas. The upper valve led to a bladder-type differential evacuation pressure controller and a mercury U-manometer, allowing both monitoring and accurate control of the chamber pressure. Hydrogen, methane, and an optional third gas (i.e. nitrogen or argon) could be simultaneously fed into the deposition chamber through Gilmont flow meters connected to a mixing chamber. Mixed gases were fed into the chamber at the base, where they were directed toward the filament and substrate via a copper tube. Gilmont Flowrate Analysis software was used to determine standard cubic centimeters per minute (sccm) of gas flowing into the chamber at the operating pressure. Within this software, changes in gas density and viscosity were taken into consideration.

The substrate holder consisted of two thin, molybdenum clamps attached to a copper brace and two stainless steel rods. It touched the sample only on two opposite corners, allowing for rapid substrate heating and large temperature variations across the surface. The distance between the substrate and filament was adjusted by raising and lowering the substrate holder through two screws in the top plate. Substrate temperature measurements were made using a high-temperature thermocouple made of tungsten + 3% rhenium and tungsten + 25% rhenium wires held to the back of the silicon substrate by a beveled-edge ceramic bar. The filament temperature was measured using a three-band optical pyrometer focused on the hottest area of the filament.

Procedure Substrates were cut to roughly 3 cm x 3 cm from four inch silicon wafers obtained from Wacker. The prime (polished) wafers were all from the same lot, with {100} orientation and resistivities of 1 to 10 ohm-cm. Cut substrates were polished with 9 μm diamond paste followed by a water rinse. This procedure was intended to leave as much diamond seed on the silicon as possible, thus enhancing the number of nucleation sites. Inspection of samples before deposition with a 3400x microscope, however, revealed no residual diamond particles larger than 0.01 μm .

Substrates were secured to the substrate holder by the two molybdenum clamps and the thermocouple was then sandwiched between the silicon substrate and ceramic bar. The top plate was lowered into place and the distance between the substrate and the filament adjusted to approximately 5 to 7 mm. The deposition chamber was evacuated to 100 mTorr, closed off, and then filled with the pre-determined amount of hydrogen, methane, and optional third gas. Once a pressure of 30 Torr was reached, the bladder pressure in the controller was set and the filament turned on. The filament voltage was increased by 15 volts every 30 seconds until the substrate reached the desired temperature. Filament temperature during operation commonly reached 1900 ± 50 °C.

The system was monitored every 20 minutes for the entire deposition period. Substrate and filament temperatures, filament voltage and current, and gas flow rates were recorded and adjustments were made when necessary. At the end of the deposition period, the bottom plate valve was opened fully to evacuate the chamber, all gases were shut off, and the filament was slowly turned off. The system was maintained at 100 mTorr until the chamber cooled to room temperature. Samples were then ready for Raman characterization.

Micro-Raman Spectrometer

Apparatus The setup for the micro-Raman spectrometer used in this experiment is shown in Figure 2.5. Monochromatic, coherent light of wavelength 514.5 nm was produced using a Spectra Physics 2020 argon-ion laser with a variable power from 50 mW to 2.0 W. The laser output was directed into a Pelin Broca filter system, which allowed the selective transmission of vertically polarized light and filtered the non-lasing plasma lines. Prisms in the system dispersed the laser beam and then re-focused it by a lens of focal length 300 mm into a pinhole aperture placed at the focal point. The beam then entered a second lens of focal length 100 mm located 100 mm away, from which it was directed into an Olympus BH-2 metallurgical microscope via a system of mirrors.

The Olympus BH-2 was equipped with objective lenses of 10x, 50x, and 100x mounted on a rotatable turret. A Javelin video camera connected to an NEC monitor allowed for both viewing and positioning of the laser beam on the sample surface. Internal lenses within the microscope and camera

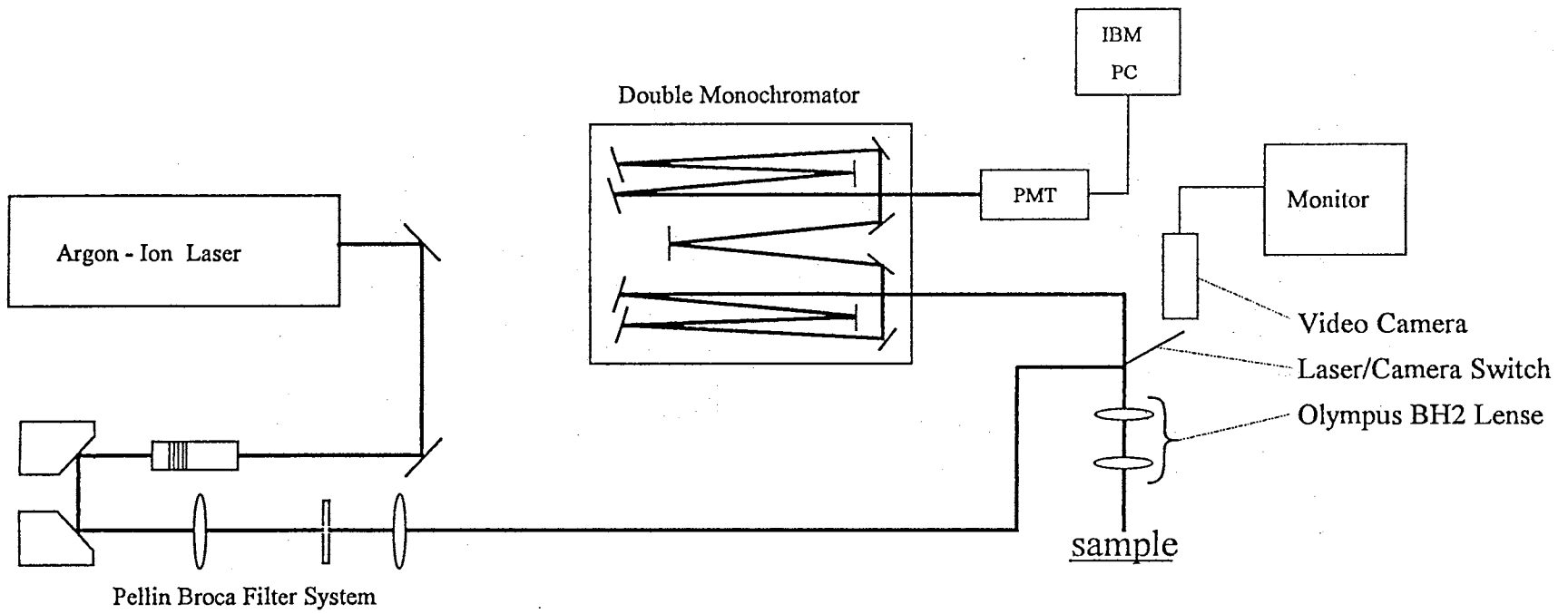


Figure 2.5. Micro-Raman spectrometer used for sample characterization.

added a total magnification of 34x, giving sample-to-screen magnifications of 340x, 1700x, and 3400x. Incident laser light was focused normal to the pivoting substrate platform through the Olympus BH-2 lens system, with the beam diameter at the sample measuring roughly 2 μm using the 100x objective.

Light scattered (and reflected) by the sample was collected in the backscattering configuration, focusing into a Jobin-Yvon Ramanor U-1000 double monochromator. Each of the two monochromators featured an asymmetric Czerny-Turner mounting with two symmetrical opening slits. The diffraction gratings of the monochromators (1800 grooves/mm) rotated on a single horizontal shaft parallel to the grating grooves. A concave mirror of focal length 0.5 m coupled the two monochromators by imaging the exit slit of the first with the entrance slit of the second. Four mirrors, all with focal lengths of 1.0 m, diverted the optical paths. Light exiting the double monochromator was directed into an RCA C31034A photomultiplier tube (PMT) cooled to -20°C by a Products for Research thermoelectric cooling unit. This was in turn connected to an IBM PC running ISA Enhanced Prism software.

Procedure Each day the Raman spectrometer was used, several alignment and calibration procedures were performed. First, the optics of the double monochromator were aligned using the 546.1 nm mercury line of fluorescent room light. With slits equally opened to 20 μm and the diffraction gratings appropriately positioned for the mercury line, both the monochromator coupling mirror and the final mirror in the second monochromator were adjusted to maximize the PMT signal intensity

Next, the laser beam was aligned through the optics, beginning at the Pelin Broca filter system. The pattern of the beam was observed after the beam expander and, if not circularly symmetric, the mirror just before the beam expander was adjusted. The second Pelin-Broca prism was then aligned to maximize the intensity of the beam through a pinhole. Next, the laser beam was focused on a single crystal (100) prime silicon wafer through the 100x objective of the microscope. With the image of the beam on the monitor, the microscope stage was moved up and down to check the symmetry of the beam. If the beam did not focus symmetrically, mirrors leading into the microscope were adjusted until it did, thus assuring the backscattering configuration. Next, with monochromator slit widths of 200 μm , a laser power of 500 mW, and the (110) direction of the silicon sample aligned with the polarized laser beam, the mirror

directing scattered light into the first monochromator was adjusted to maximize the intensity of 520 cm^{-1} peak of silicon. The peak maximum was determined by a quick scan from 515 to 525 cm^{-1} with an increment of 0.1 cm^{-1} and an integration time of 0.2 s . If not located at 520 cm^{-1} , the peak maximum was recalibrated to this value within the Prism software.

Since Raman linewidths were important in this study, the width of the Raman peak of natural diamond was determined as a function of slit width. Scans were taken with slit widths of 200 , 150 , 100 , 50 , and $30\text{ }\mu\text{m}$ from 1310 to 1350 cm^{-1} in 0.2 cm^{-1} increments with an integration time of 1.0 s . The peak width was found to decrease linearly with slit width until reaching $30\text{ }\mu\text{m}$, where diffraction became a problem. By plotting peak width vs. slit width, the zero-slit width (intrinsic) diamond peak width was found to be 1.7 cm^{-1} . The actual width of the diamond peak is found by Solin and Ramdas [50] to be 1.65 cm^{-1} at room temperature, so that instrumental broadening is minimal. The purpose of this exercise was to determine the absolute minimum peak width which could be expected for CVD diamond grains while using large slit widths. In this way, resolution could be sacrificed to obtain an improved signal to noise ratio.

Before scans were taken, the entire surface of each diamond film was visually inspected using the $100\times$ objective of the Raman microscope. Next, preliminary scans were done on representative grains in regions of interest. These scans extended over the broad range of 500 to 1600 cm^{-1} in 1.0 cm^{-1} increments, each integrated for 0.2 s . This was done to check for not only different carbon structures, but also for the presence of carbides and non-carbon materials. Those samples found to contain diamond were further evaluated every 1 to 2 mm across the surface, radially outward from the sample center to either of the clamped corners. These more focused scans extended from 1250 to 1700 cm^{-1} in 0.5 cm^{-1} increments with integration times of 0.2 s . All spectra were taken at a constant laser power of 500 mW , which amounted to roughly 100 mW at the sample. With each of the secondary scans, grain size, morphology, and location on the sample were recorded.

After scans were taken, they were converted from Prism ISA to ASCII files and were loaded into Jandel's Scientific Peakfit where they were fit using the Voight profile -- the response of a Gaussian filter to a Lorentzian signal. Spectra were fit using a minimal number of peaks, with additional peaks added

only when the fitted curve clearly strayed from the observed data points. Computations were continued through at least one hundred iterations to ensure a good fit, if not stopped by the computer sooner. The coefficient of determination, r^2 , provided a measure of accuracy for the computer-generated curve. This number, which ranges from zero to one (with one indicating a perfect fit to the data), was typically 0.99 or better for CVD grain examined in this portion of the study although poorer quality grains had lower r^2 values, since the signal to noise ratios were reduced for these grains. From this, it is seen that the r^2 value provides a quantitative measure of fit *and* resolution. Grain statistics were evaluated and graphed using Stanford Graphics software.

Results and Discussion

Forty-four samples produced in this study were found to contain grains of diamond. Deposition parameters for these films, summarized numerically in Table II and graphically in Figure 2.6, were quite varied, with methane concentrations ranging from 1.0 to 6.7%, substrate temperatures from 770 to 1100°C, and total flow rates from 26 to 200 sccm. All samples were grown with a chamber pressure of 30 ± 5 Torr and filament temperature of 1900 ± 50 °C.

Grain Characterization

To the unaided eye, sample surfaces appeared coated with concentric ellipses of gray material centered about the region closest to the filament. These rings, thickest at the sample center, originated from differences in the temperature and carbon concentration, which both decreased at greater distances from the sample center. Inspection with the 100x objective of the microscope revealed dense non-structured growth in the central region surrounded by grains which became smaller and sparser at distances further out. Interference patterns were seen at the corners farthest from the filament on some samples, revealing the presence of a thin film in this region.

The thick growth in the sample center was found to be Raman inactive over the range of 10 to 3000 cm^{-1} aside from the silicon peak, suggesting that this region most likely contains either completely disordered sp , sp^2 , and sp^3 carbon or possibly an amorphous silicon layer. Excluding this region, the

TABLE II
SUMMARY OF CHEMICAL VAPOR DEPOSITION GROWTH PARAMETERS
FOR ALL SAMPLES IN THIS STUDY

Sample #	Percent Methane	Substrate Temperature (°C)	Total Flow Rate (sccm)	Deposition Time (h)
1	1.0	1100	180	3.5
2	1.1	1000	180	4.5
3	1.3	1050	180	6.0
4	1.4	860	160	3.0
5	1.4	1050	190	3.0
6	1.5	820	160	3.0
7	1.5	930	200	4.5
8	1.5	1020	200	3.0
9	1.6	850	170	3.5
10	1.6	880	160	3.0
11	1.6	890	140	4.5
12	1.6	940	190	3.5
13	1.6	1020	180	4.5
14	1.6	1040	190	4.0
15	1.7	985	190	3.0
16	1.7	1000	200	3.0
17	1.7	1030	170	4.5
18	1.7	1050	190	9.5
19	1.8	970	170	3.0
20	1.8	990	160	3.0
21	1.8	1010	180	3.0
22	1.9	940	79	3.0

TABLE II (cont'd)

Sample #	Percent Methane	Substrate Temperature (°C)	Total Flow Rate (sccm)	Deposition Time (h)
23	2.0	880	81	3.5
24	2.0	960	160	3.0
25	2.0	1000	200	3.0
26	2.2	1050	190	3.0
27	2.7	960	190	2.5
28	2.7	1020	180	3.5
29	2.8	790	170	3.0
30	3.3	920	43	2.0
31	3.5	960	26	4.0
32	3.5	1060	160	3.0
33	3.8	930	50	6.5
34	3.9	970	180	2.5
35	4.1	910	190	3.0
36	4.1	920	58	5.0
37	4.4	1000	91	2.5
38	4.6	845	200	3.5
39	4.6	960	120	3.0
40	5.0	850	48	3.0
41	5.8	770	170	3.0
42	6.1	900	45	3.0
43	6.4	830	220	3.0
44	6.7	930	40	1.5

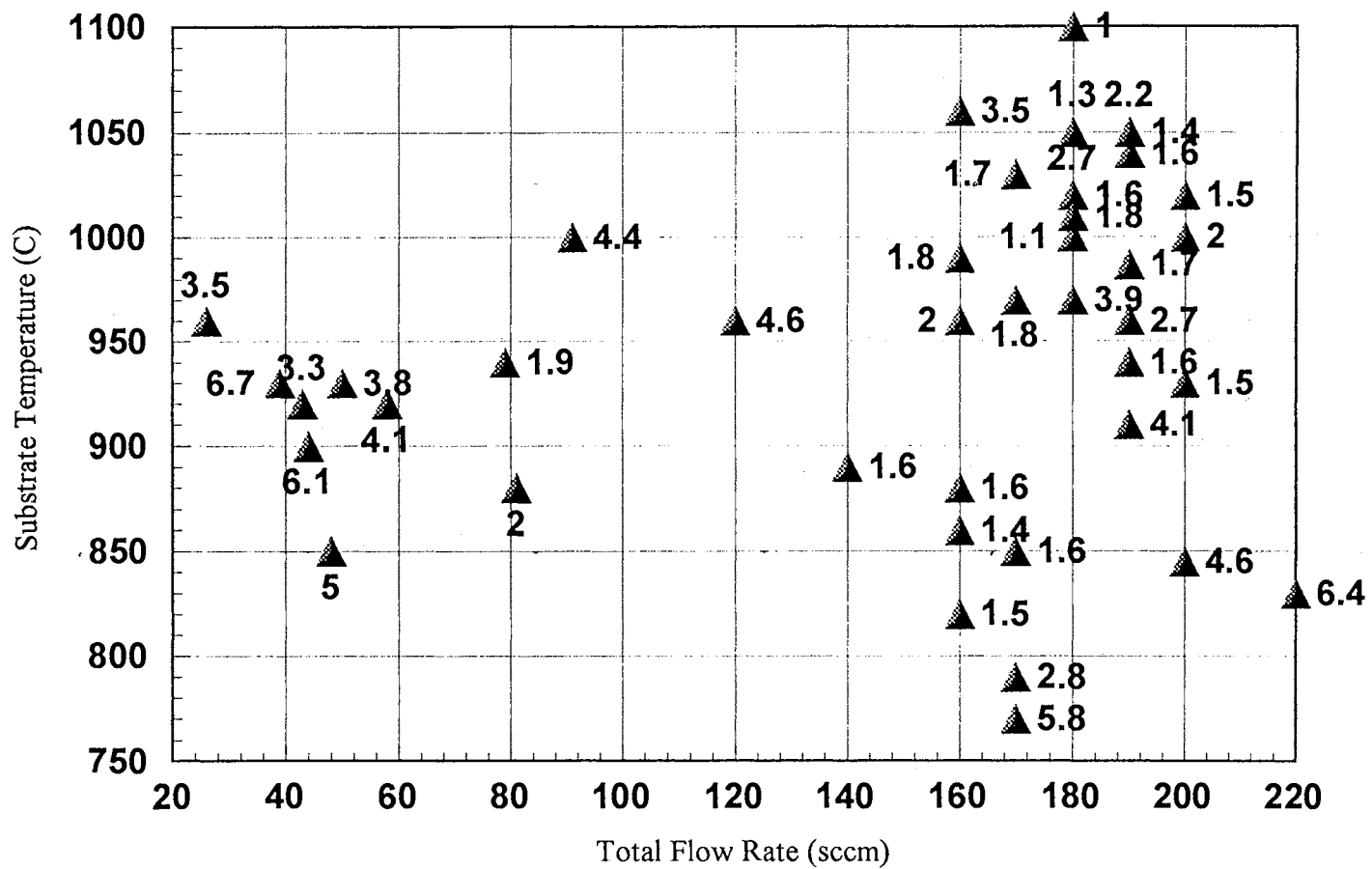


Figure 2.6. Substrate temperature vs. total flow rate for CVD diamond films in this study. Corresponding methane concentrations are listed next to data points.

substrate was covered with a single layer of carbon grains typically 1 to 10 μm in diameter, with an average grain size of 2 μm . The average grain density, estimated by counting grains on the video monitor, was approximately 10^5 to 10^6 grains/ cm^2 , although in some regions of extremely thick growth, densities neared 10^{10} grains/ cm^2 . In most regions, grains did not completely cover the sample surface.

Raman spectra, grain size, and morphology were recorded as a function of location for 167 grains on the 44 samples in this study. These grains were then classified by color and morphology into seven different categories: black cauliflower grains, black cauliflower grains with shiny inclusions, black cauliflower grains with (100) faces, dark gray cauliflower grains, silver cauliflower grains, silver cauliflower faceted grains, and silver faceted grains. The numbers of grains in each category were 10, 15, 7, 21, 58, 36, and 20, respectively. Radially outward from the sample center, grain types occurred predominantly in the order listed above, though not all types were present on all samples. In fact, each sample showed only one region of highly-faceted grains, if any at all. Those samples which contained black cauliflower grains with (100) faces had only the first four or five grain types, while those with silver faceted grains contained only the last three or four grain types. Darker grains were typically situated 2-4 mm from the center of the sample, while lighter grains were found 4-6 mm out, on the average. Figure 2.7 illustrates the regions of the sample where each grain type was typically found if it was present on the sample. Growth rings were narrower along the axis which ran parallel to the filament, but otherwise showed the same distribution of grain types.

SEM photographs of the various grain morphologies are shown in Figure 2.8(a-d). Black cauliflower, dark gray cauliflower, and silver cauliflower grains, differing visually only by shading, are represented in 2.8(a), with an absence of clearly defined faces and a high degree of disorder. Figure 2.8(b) is representative of (100) faces on black cauliflower grains, consisting of a conglomeration of well-defined (100) cube faces and cauliflower growth. The size of the faces varied a great deal between grains, ranging from roughly 0.1 μm to 5 μm on a side. Those grains with (100) faces even smaller than 0.1 μm were referred to as black cauliflower grains with shiny inclusions.

Cauli-faceted grains are shown in Figure 2.8(c), resembling a multitude of spiked balls of octahedra with their [100] crystal axes pointing radially outward. As the distance from the sample

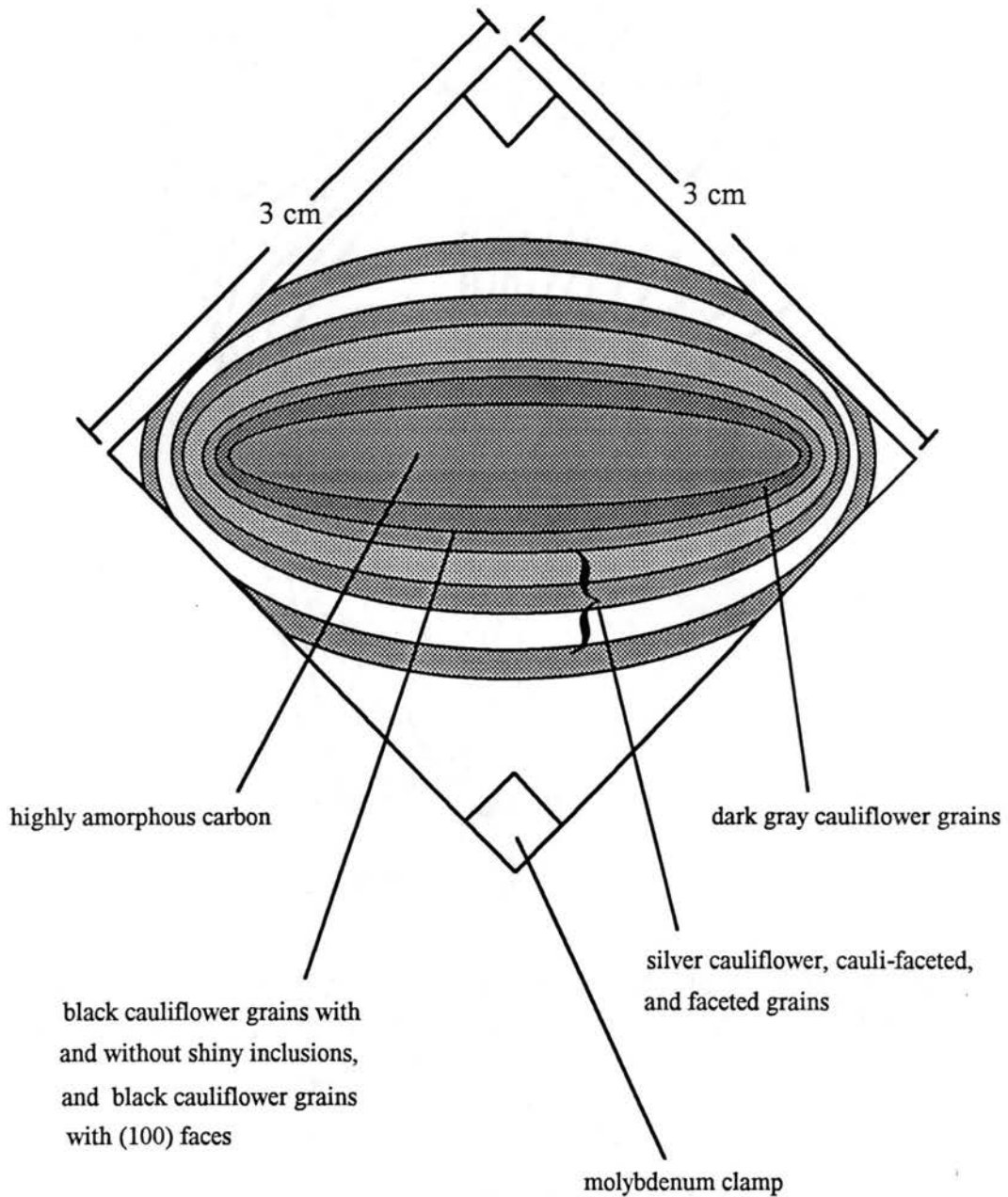
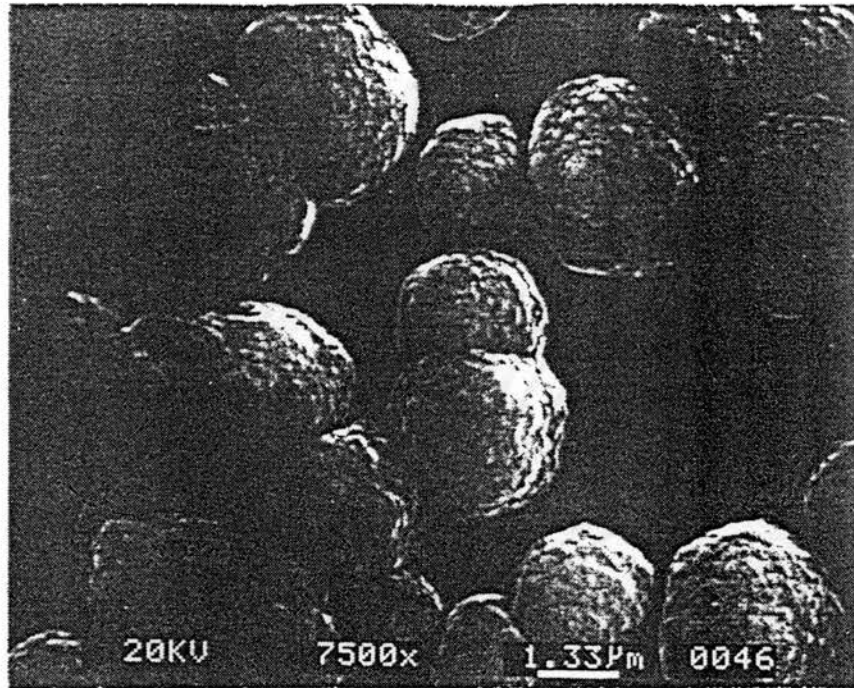
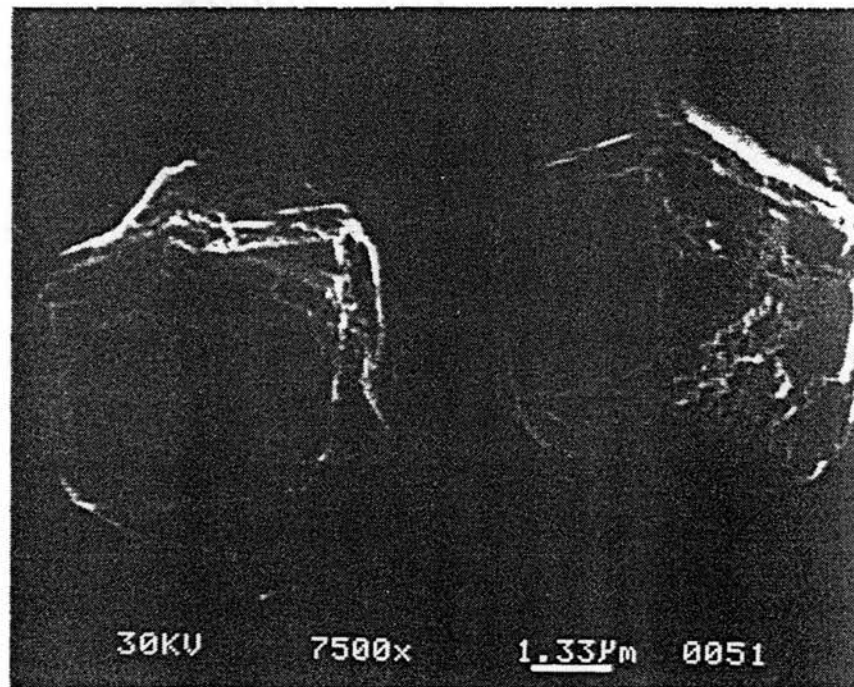


Figure 2.7. Typical distribution of CVD diamond grains on the silicon substrate. The longer oval axis runs parallel to the filament. Locations of molybdenum clamps are also noted.

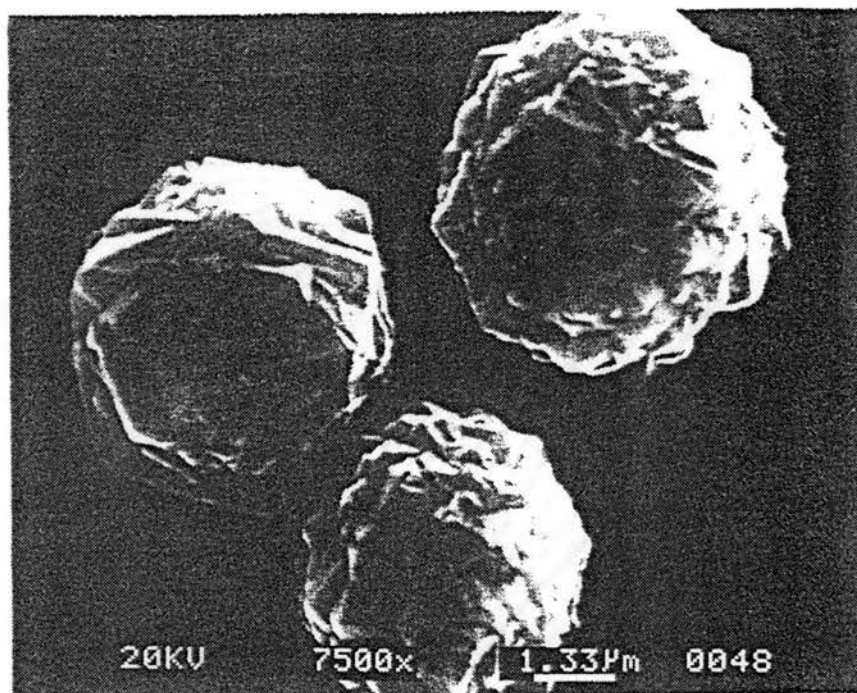


(a)

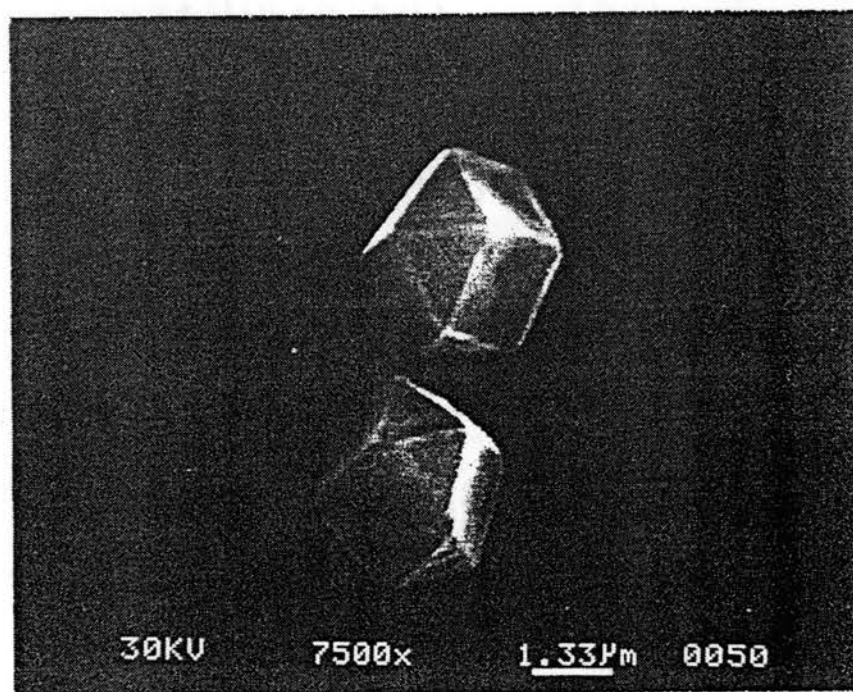


(b)

Figure 2.8. SEM photographs of the different CVD diamond grain morphologies represented in this study. (a) highly disordered cauliflower grains and (b) cauliflower grains with (100) faces. Figure 2.7 (c) and (d) are shown on following page.



(c)



(d)

Figure 2.8 (continued from previous page). SEM photographs of the different CVD diamond grain morphologies represented in this study. (c) cauli-faceted grains, resembling spiked balls of octahedra with the [100] crystal axes pointing radially outward and (d) single-crystal faceted grains -- in this case, twinned cubo-octahedra with (111) faces parallel to the substrate.

center increased, silver cauli-faceted grains became less polycrystalline, eventually evolving into single-crystal silver faceted grains, like those shown in 2.8(d). In this figure, two twinned cubo-octahedra are oriented with their triangular (111) faces parallel to the silicon surface. The majority of silver faceted grains in a given region were found to have the same orientation, although several exceptions were found. In addition, the morphologies of adjacent grains were often different, with twinned grains commonly occurring beside perfect cubo-octahedra.

Raman spectra of the different grain types revealed the presence of different carbon forms in the different categories of grains. Diamond-like carbon (DLC) was the most widespread allotrope of carbon, present in all categories and in most of the 167 grains examined. Amorphous carbon (a-C) was found in considerably lesser amounts than DLC, but was found in all categories except that of (100) faces on black cauliflower grains. On several occasions, the a-C spectra contained the additional peak at 1490 cm^{-1} attributed to small domains. Typical Raman spectra for DLC and a-C are shown in Figure 2.9.

The majority of grains showed an additional, much narrower Raman peak located between 1320 and 1336 cm^{-1} , suggestive of either diamond or lonsdaleite. Of these grains, those with peaks situated between 1325 and 1336 cm^{-1} were certain to contain diamond shifted by heat and/or stress from the 1332.5 cm^{-1} position of natural diamond. Additional Raman spectra were taken of those grains with peaks situated below 1325 cm^{-1} to determine whether they contained lonsdaleite or diamond. (Levels of ^{13}C higher than 1.1% were ruled out, since the methane used in this experiment was obtained from natural sources.) By taking scans at successively lower laser powers, peaks were seen to become narrower and closer to 1332.5 cm^{-1} , revealing that these grains were in fact diamond, shifted in position due to laser heating, and not lonsdaleite.

The quality and amount of diamond present varied significantly by grain type. Peak widths commonly ranged from 10 to 20 cm^{-1} , although some were as broad as 80 cm^{-1} . At the author's discretion, these broader peaks were still categorized as diamond, since the peak occurred in addition to an even broader underlying sp^3 peak. Much narrower diamond peaks were produced by exceptional grains, some with linewidths of 2.6 cm^{-1} , the same as that of natural diamond using $200\text{ }\mu\text{m}$ slit widths. Three typical diamond spectra are shown in Figure 2.10.

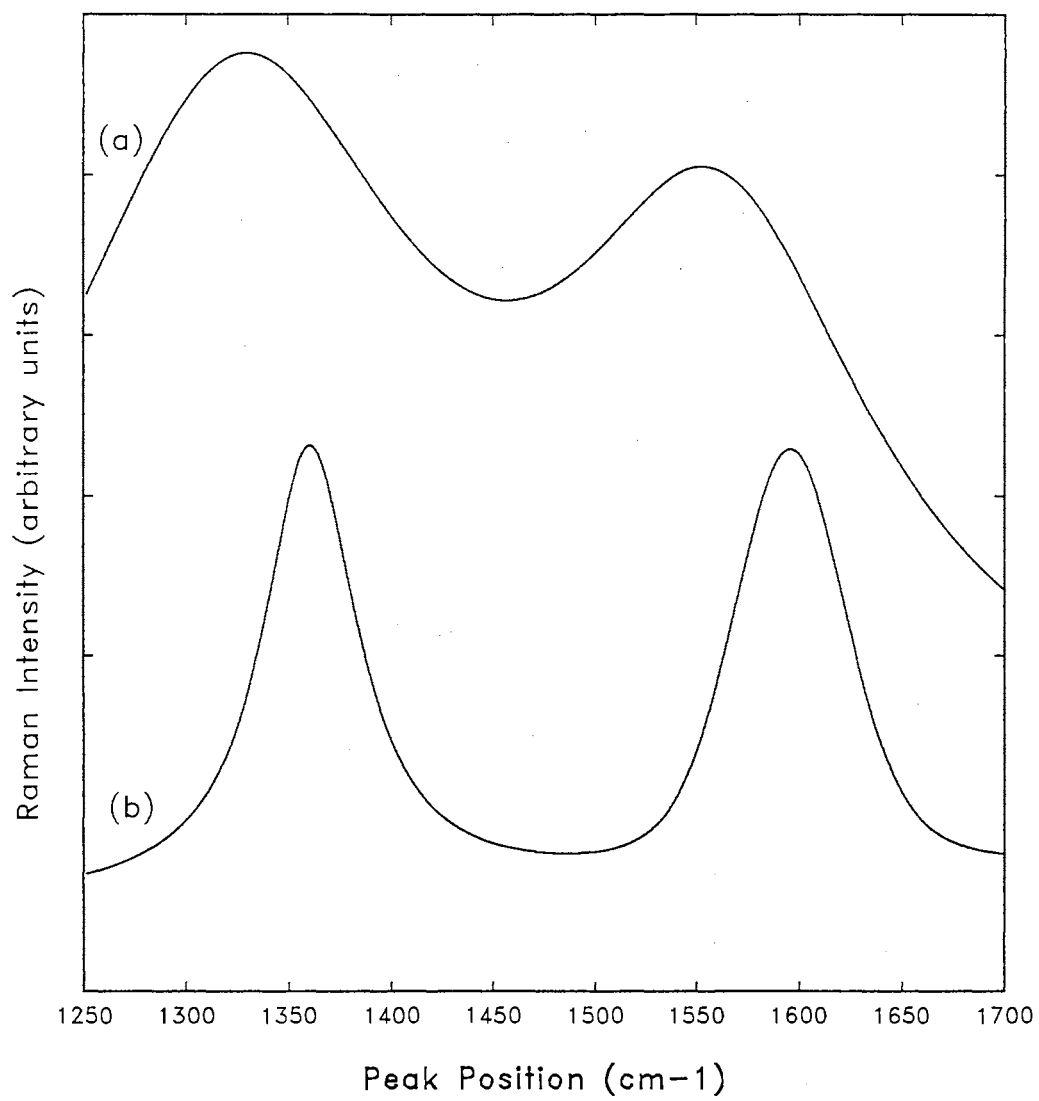


Figure 2.9. Typical Raman spectra for (a) diamond-like carbon and (b) amorphous carbon produced in this study.

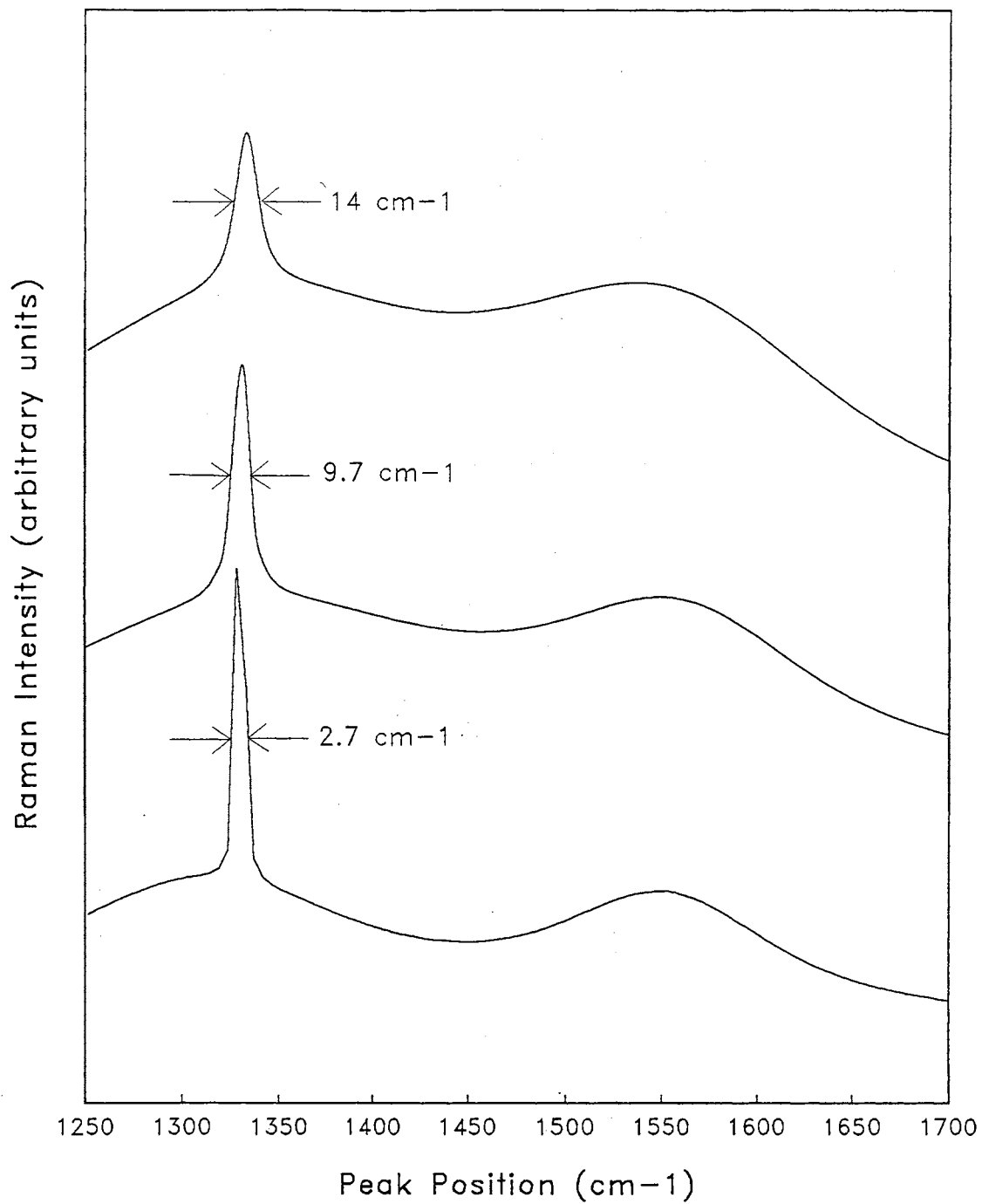


Figure 2.10. Typical Raman spectra for diamond produced in this study. FWHM values from top to bottom are 14, 9.7, and 2.7 cm⁻¹.

Since not all grains in each group were found to contain diamond, the percentage of diamond-containing grains was determined for each grain type. These percentages, found by dividing the number of grains in a category that show a diamond peak by the total number of grains in the category, are shown in Figure 2.11. Black cauliflower grains with (100) faces and silver faceted grains were found to have the highest proportion of diamond-containing grains, at 100 and 95%, respectively. Percentages dropped to 86, 70, and 43% for silver cauli-faceted, silver cauliflower, and dark gray cauliflower grains. Only 6.7% of black cauliflower grains with shiny facets were found to contain diamond while black cauliflower grains contained none.

Since the width of the diamond peak is governed by localized strains in the diamond lattice due to defects and impurities, as well as by the anharmonic interactions between the vibrational modes, it suffices to say that the width of the diamond peak provides a measure of crystalline quality. By comparing the average linewidths for each grain type, the quality of diamond present was found to vary largely as a function of morphology and color. As seen in Figure 2.12, black cauliflower grains with (100) faces contained the highest quality diamond, with an average peak width of 5.1 cm^{-1} . These were followed by silver faceted, silver cauli-faceted, silver cauliflower, and dark gray cauliflower grains, which had average peak widths of 12, 16, 20, and 25 cm^{-1} , respectively. Standard deviations were greatest for silver cauli-faceted, silver cauliflower, and dark gray cauliflower grain categories, which contained increasingly greater quantities of disordered diamond with broad (40 to 80 cm^{-1}) peak widths. Only one black cauliflower grain with shiny inclusions had a diamond peak in its Raman spectrum, giving this category a standard deviation of zero.

In comparing Figures 2.11 and 2.12, the percentage of diamond-containing grains seems to be inversely correlated with the average diamond peak width and thus directly correlated with the quality of the diamond present. At first, this would seem to imply that the more likely a grain is to contain diamond, the higher its quality is likely to be. In actuality, though, this connection stems from the amount of disorder present in the different types of grains. The diamond peak originates from the growth of ordered domains of sp^3 bonding, becoming narrower and more intense as the domain size increases. In some cases, domains of sp^3 bonding may be present, but may be so broad and lacking in intensity that

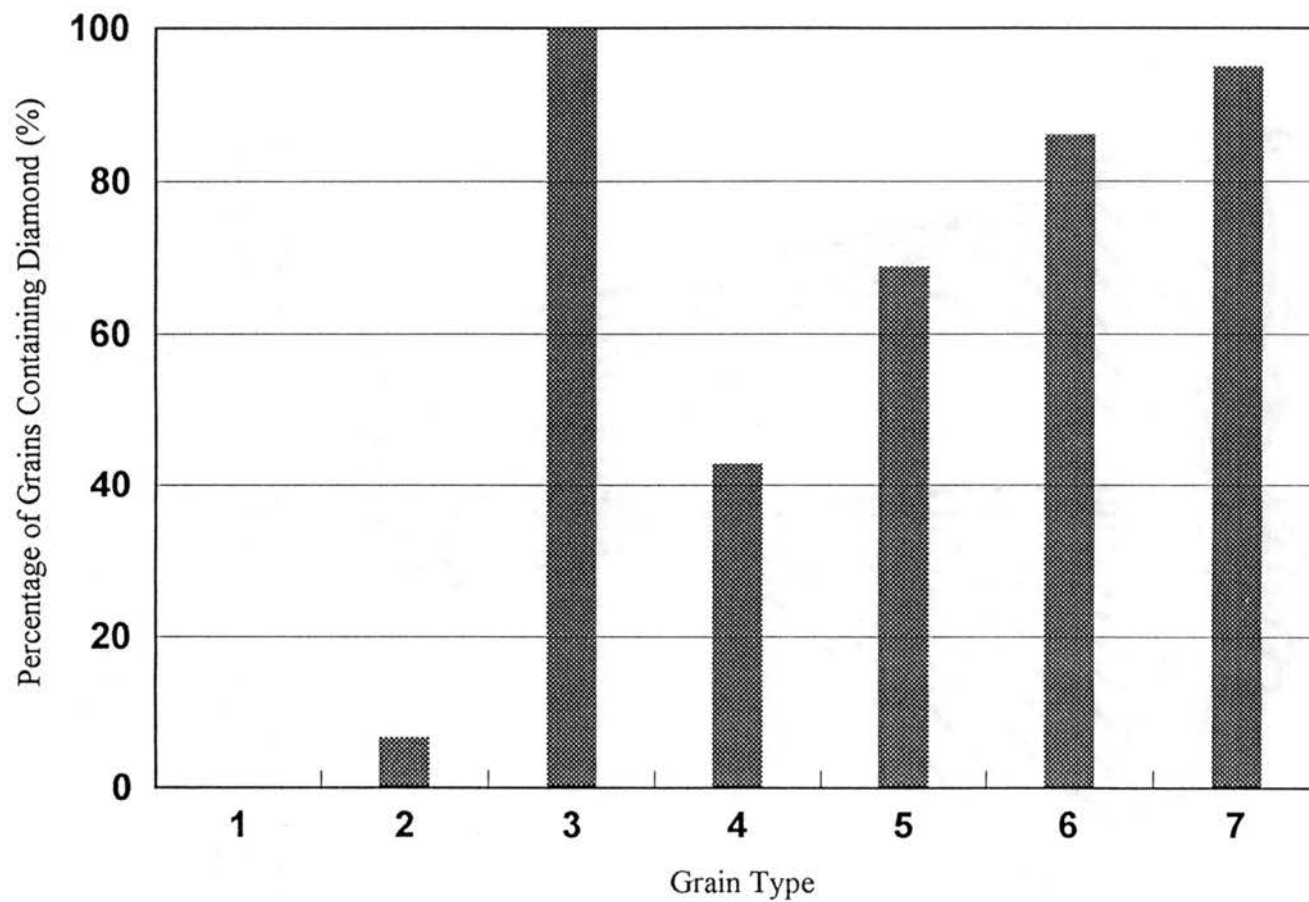


Figure 2.11. Percentage of CVD grains containing diamond as a function of grain type. 1 = black cauliflower grains, 2 = black cauliflower grains with shiny inclusions, 3 = black cauliflower grains with (100) faces, 4 = dark gray cauliflower grains, 5 = silver cauliflower grains, 6 = silver cauli-faceted grains, and 7 = silver faceted grains.

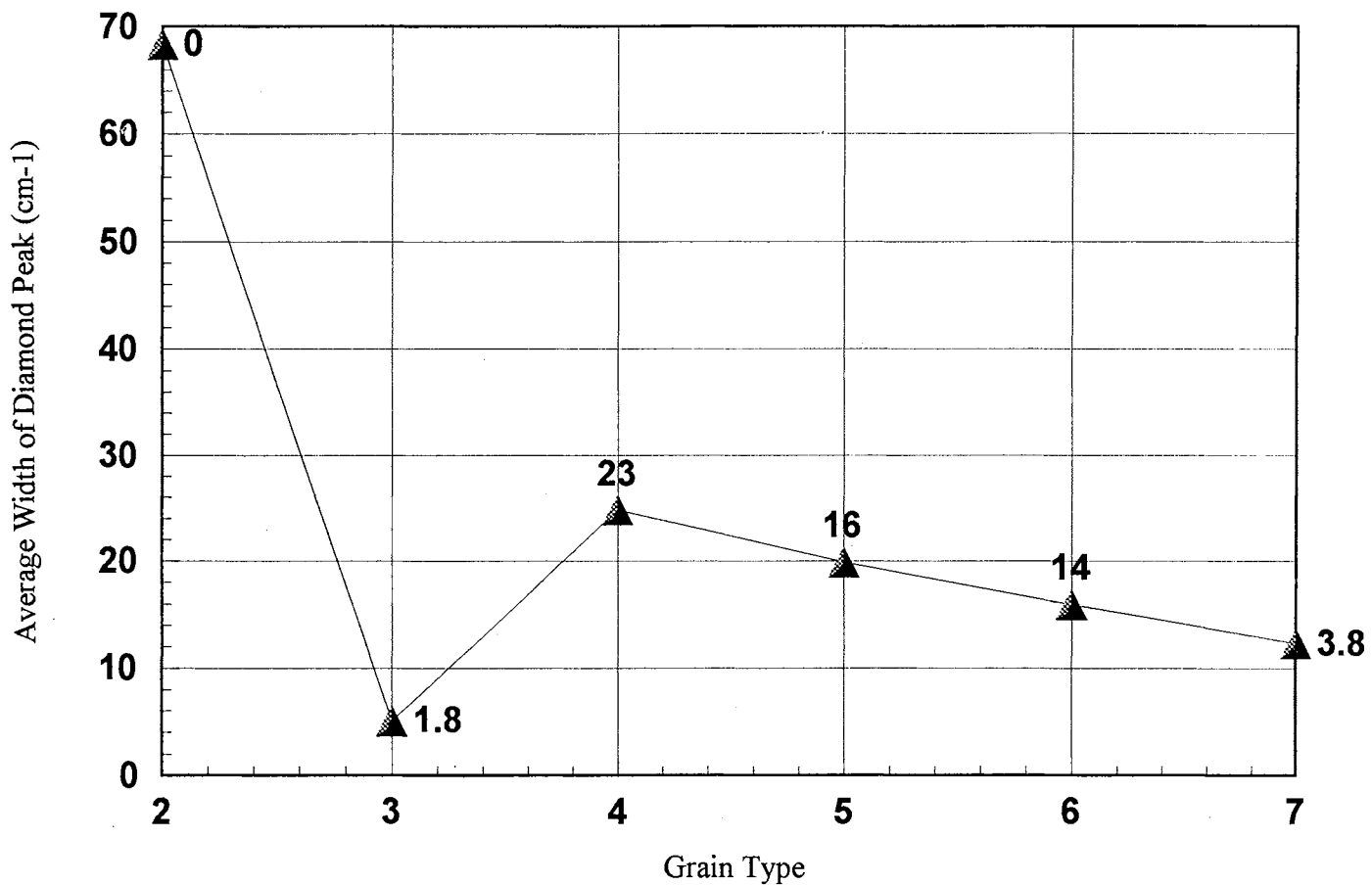


Figure 2.12 Average width of the CVD grain Raman diamond peak as a function of grain type. 2 = black cauliflower grains with shiny inclusions, 3 = black cauliflower grains with (100) faces, 4 = dark gray cauliflower grains, 5 = silver cauliflower grains, 6 = silver cauli-faceted grains, and 7 = silver faceted grains. Standard deviations are included beside data points.

they are obscured by noise and the disordered sp^3 peak. With this in mind, it is more correct to say that the more likely a grain is to contain *large domains* of sp^3 bonding, the higher its quality is likely to be. And well it should, since the domain size and quality are both directly dependent on the amount of disorder present.

Quality also had a significant influence on the responsiveness of grains to laser exposure. Higher quality grains, usually lighter in color, contained lower levels of sp^2 bonding. As a result, they were more transparent to the 514.5 nm laser light, which was absorbed more readily by more graphitic grains. Those grains with larger domains and hence fewer boundaries were better able to transfer energy into the silicon, which acted as an infinite heat sink. This is because some percentage of the thermal phonons are always reflected back into the material of origin at each boundary. This occurrence, known as the *kapitza resistance* phenomenon, is discussed more fully in Chapter III.

Extreme heating effects were displayed by many poorer quality grains, which vaporized instantly upon exposure to the 500 mW laser beam. These findings are supported by Figure 2.13. Calculated by grain type, the lowest percentages of vaporization occurred for black cauliflower grains with (100) faces (0%), silver faceted grains (5.0%), silver cauli-faceted grains (8.3%), and silver cauliflower grains (17%). Much larger percentages of vaporization were found for dark gray cauliflower grains, black cauliflower grains with shiny inclusions, and black cauliflower grains.

Grain heating also affected the position of the diamond peak, as shown in Figure 2.14. The average diamond peak position of 1332.2 cm^{-1} for silver faceted grains was closest to the 1332.5 cm^{-1} position of natural diamond. Silver cauli-faceted, silver cauliflower, dark gray cauliflower, and black cauliflower grains with (100) faces experienced increasingly more downshifted average positions of 1331.8 , 1330.7 , 1329.3 , and 1326.2 cm^{-1} . This is as one would expect for those grain types with lower quality and higher percentages of grain vaporization. However, in comparing Figures 2.13 and 2.14, black cauliflower grains with (100) faces are seen to behave anomalously, having the highest quality, and yet also shifting the most. For these grains, uniquely composed of a heterogeneous conglomeration of (100) cubic faces and dark cauliflower growth, laser light passing through the cube faces is absorbed by the black cauliflower growth. The cauliflower material heats the faces up, while the faces keep the

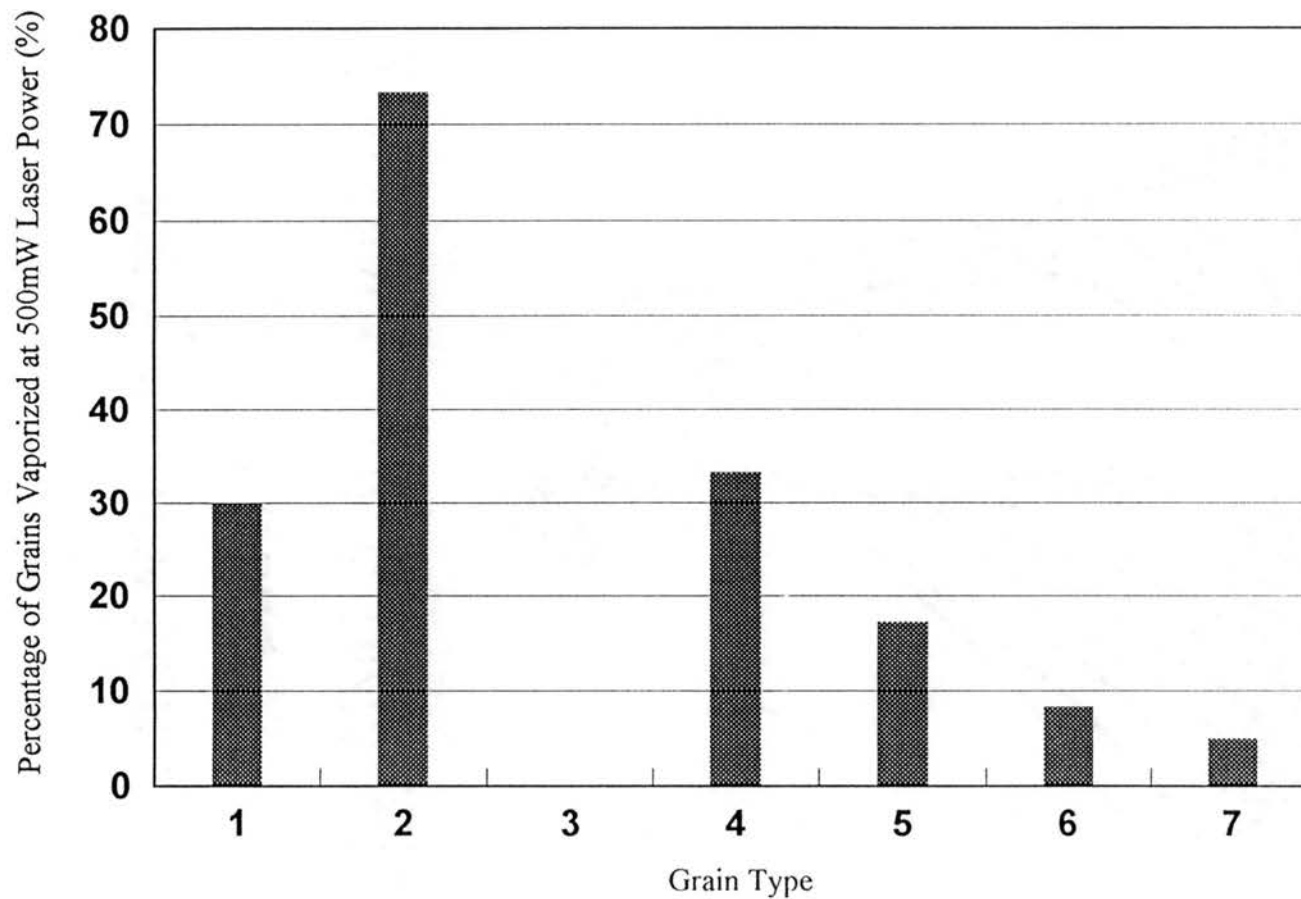


Figure 2.13. Percentage of CVD grains which vaporized at 500 mW laser power as a function of grain type. 1 = black cauliflower grains, 2 = black cauliflower grains with shiny inclusions, 3 = black cauliflower grains with (100) faces, 4 = dark gray cauliflower grains, 5 = silver cauliflower grains, 6 = silver cauli-faceted grains, and 7 = silver faceted grains.

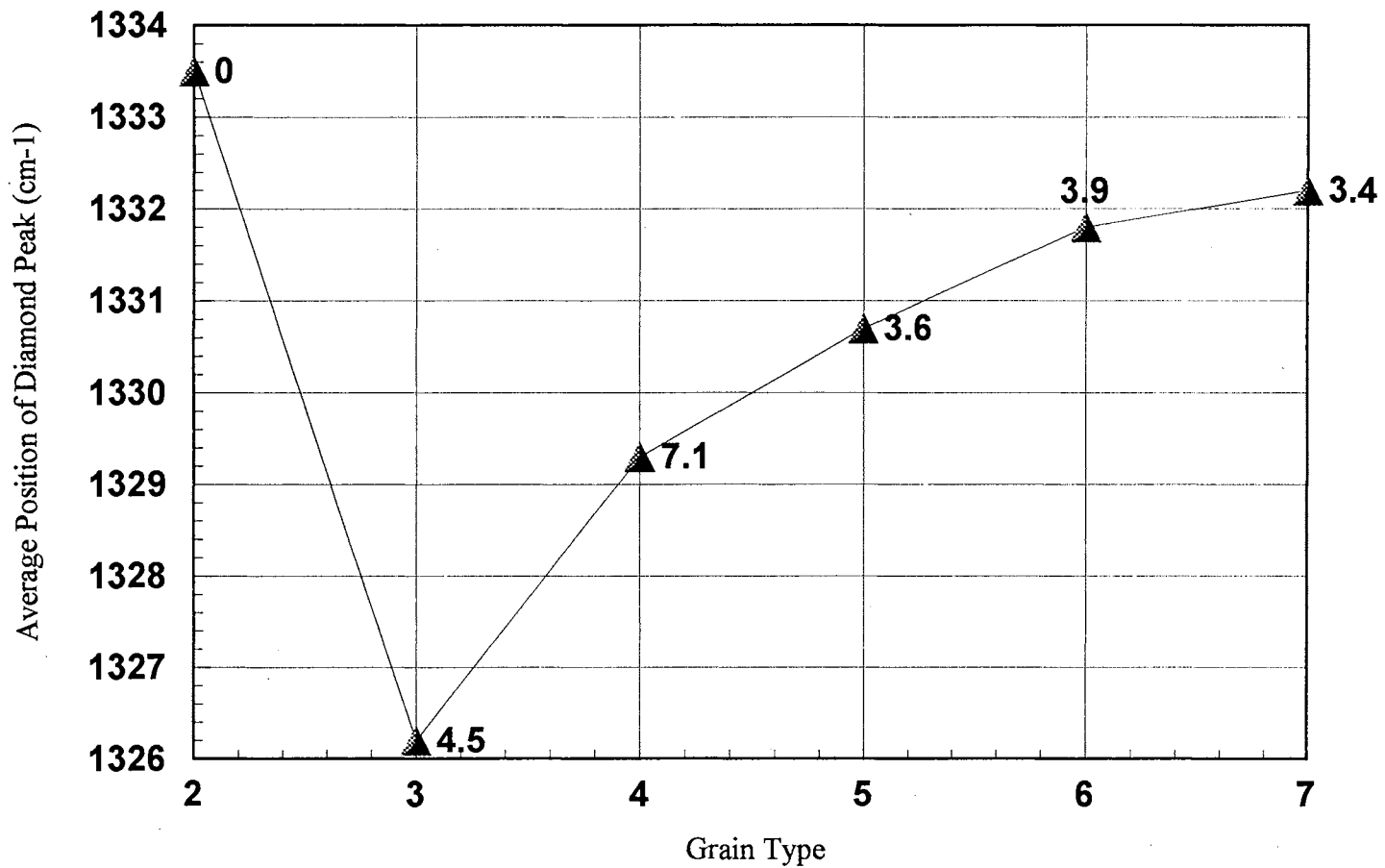


Figure 2.14. Average position of the CVD grain Raman diamond peak as a function of grain type. 2 = black cauliflower grains with shiny inclusions, 3 = black cauliflower grains with (100) faces, 4 = dark gray cauliflower grains, 5 = silver cauliflower grains, 6 = silver cauli-faceted grains, and 7 = silver faceted grains. Standard deviations are included beside data points.

cauliflower growth from vaporizing by helping to dissipate the heat. The standard deviation for black cauliflower grains with (100) faces is significantly larger than those of all other grain types, most probably because the sizes of the faces and the black cauliflower regions vary independently, drastically affecting heat absorption and dissipation.

While heating effects will always cause a downward shift in peak position, stresses may shift the diamond peak in either direction, with tensile and compressive stresses respectively causing positive and negative shifts in the frequency. Many silver grains showed peak positions slightly higher than that of natural diamond, most certainly due to a net compressive stress within the grains. Given that these grains form in the outer regions of the substrate, the diamond peak could very well be shifted due to carbon defects and hydrogen interstitials in the diamond lattice. This is supported by the fact that the *single* crystal silver faceted grains have an average Raman peak width twice as large as the *polycrystalline* conglomerations of black cauliflower grains with (100) faces. This is peculiar, since single crystal grains should be more ordered than polycrystalline ones. However, grains further from the filament form more slowly, since more ions have recombined before reaching this region of the substrate. These slower reaction rates could result in single-surface epitaxial growth, but with greater numbers of defects and inclusions left in the lattice due to the reduced levels of atomic hydrogen.

Evaluation of Deposition Parameters

Although all samples were found to contain several different types of grains across the surface, attempts were made to more uniquely determine the deposition parameters leading to the different shades and morphologies of grains. In assessing the relationships between growth parameters and grain types, it became apparent that grains were most sensitive to methane concentration and temperature, while total flow rates were less crucial.

Higher average methane-to-hydrogen ratios were found to coincide with poorer quality grains, as seen in Figure 2.15. Black cauliflower grains with and without shiny inclusions were found to grow at an average methane concentration of 3.2%, followed by silver cauliflower grains at 3% and dark gray cauliflower and silver cauli-faceted grains at 2.8%. Silver faceted grains and black cauliflower grains

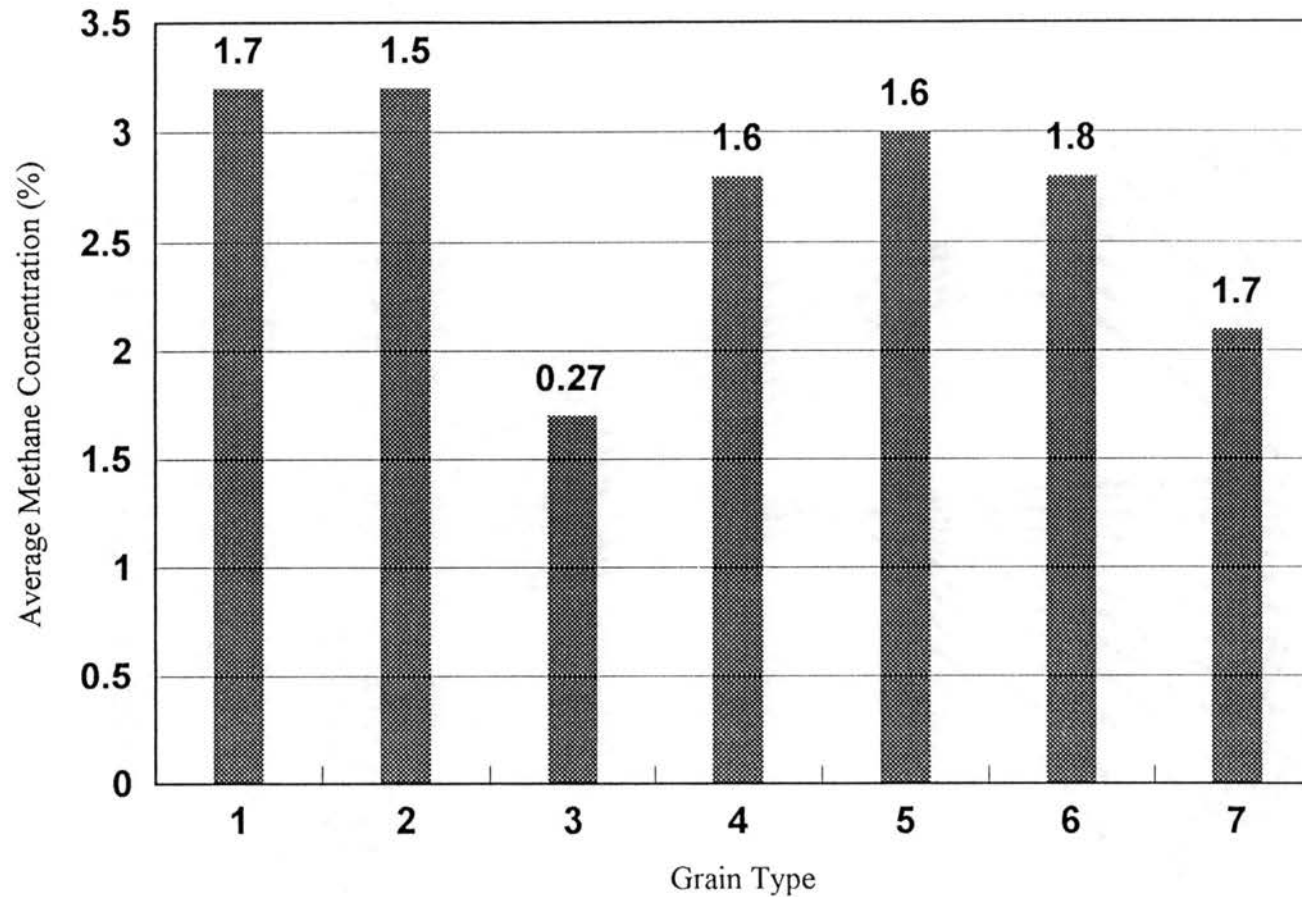


Figure 2.15. Average methane concentration for CVD grains as a function of grain type. 1 = black cauliflower grains, 2 = black cauliflower grains with shiny inclusions, 3 = black cauliflower grains with (100) faces, 4 = dark gray cauliflower grains, 5 = silver cauliflower grains, 6 = silver cauli-faceted grains, and 7 = silver faceted grains. Standard deviations are included beside data points.

with (100) faces grew at much lower average concentrations of 2.1% and 1.7%, respectively. These results demonstrate the importance of atomic hydrogen in the CVD system. As methane concentrations were reduced, grains became more faceted, with higher levels of atomic hydrogen present to suppress and remove graphitic sp^2 bonds.

In analyzing the average substrate temperature as a function of grain type, all grain types were found to have an average substrate temperature of roughly 950°C. Of course, since growth occurred over a large portion of the substrate, the possibility of substantial temperature gradients across the sample surface has to be considered. Dark gray and silver grain types, grown in the middle and outer rings, are certainly exposed to lower temperatures than black grains grown in the inner rings. Fortunately, the magnitude of this difference can be estimated theoretically.

In filament-assisted CVD systems, radiation from the filament dominates conduction and convection as the primary method of heat transfer, since temperatures are typically around 2000°C. A rough estimate of the temperature drop across the substrate may thus be made by considering the only heat transfer mechanisms to be radiation from the filament to the substrate and radiation from the substrate to its surroundings. The radiative heat absorbed from the filament by a differential substrate area dA_s , of the substrate is given by

$$Q_{fs} = F_{fs} \epsilon_f \sigma T_f^4 \epsilon_s dA_s,$$

where ϵ_f and ϵ_s are respectively the gray-body emissivities of the filament and substrate, $\sigma = 5.67 \times 10^{-12}$ W/cm² K⁴ is the Stefan-Boltzmann constant, T_f is the filament temperature, and F_{fs} is a shape factor, dependent on the diameter of the filament, filament-to-substrate distance, and the location on the sample relative to the filament. In a similar fashion, the radiative heat lost by the substrate to the wall of the deposition chamber is given by

$$Q_{sw} = 2\epsilon_s(T_s) \sigma T_s^4 dA_s,$$

where T_s is the substrate temperature and $\epsilon_s(T_s)$ is the temperature dependent gray-body emissivity of the substrate. Nulman has obtained a third degree polynomial fit for $\epsilon_s(T_s)$ for silicon in the temperature region of interest, given by

$$\varepsilon_s(T_s) = -2.8324 + 1.0379 \times 10^{-2} T_s - 9.653 \times 10^{-6} T_s^2 + 2.963 \times 10^{-9} T_s^3$$

[51]. In thermal equilibrium, the heat gained by the substrate is equal to the heat lost, so that

$$F_{fs} \varepsilon_f \sigma T_f^4 \varepsilon_s dA_s = 2 \varepsilon_s(T_s) \sigma T_s^4 dA_s.$$

Following the method used by Wolden *et al.* [52], the shape factor for a long, straight filament of length $2L$ and diameter d_f , centered at $(0, 0, h_f)$ above the center of the substrate, may be determined using variables as defined in Figure 2.16. In this figure, dA_1 and dA_2 are the differential areas of the substrate and filament joined by the vector r . The normals to the substrate, the differential filament area, and the plane containing r and the center of the filament are respectively labeled by n_1 , n_2 , and n_f . Also relevant are α , the angle between n_2 and n_f , ϕ_1 , the angle between n_1 and r , and ϕ_2 , the angle between n_2 and r .

Since r is much greater than the filament radius, the contribution of the differential filament area dA_2 to the substrate is essentially independent of the angle α . As a result, the effective surface area of the filament reduces to $dA_f = d_f dx$ and the shape factor between the filament and a differential area of the substrate, dA_1 , is given by

$$F_{fs} = \int_{-L}^L \frac{\cos \phi_1 \cos \phi_2 d_f}{\pi r^2} dx$$

where

$$r = \sqrt{(x-X)^2 + Y^2 + h_f^2},$$

$$\cos \phi_1 = \frac{h_f}{r}, \quad \text{and} \quad \cos \phi_2 = \frac{\sqrt{(h_f^2 + Y^2)}}{r}.$$

Integration of the shape factor integral yields the expression

$$F_{fs} = \frac{h_f d_f}{2\sqrt{h_f^2 + Y^2}} \left\{ \frac{L-2X}{(L-2X)^2 + Y^2 + h_f^2} + \frac{L+2X}{(L+2X)^2 + Y^2 + h_f^2} + \frac{1}{2\sqrt{(Y^2 + h_f^2)}} \left(\tan^{-1} \frac{L-2X}{\sqrt{(Y^2 + h_f^2)}} + \tan^{-1} \frac{L+2X}{\sqrt{(Y^2 + h_f^2)}} \right) \right\}$$

which may be evaluated at points $(X, Y, 0)$ across the substrate.

Taking the parameters in the present study to be $h_f = 0.6$ cm, $d_f = 0.5$ cm, and $L = 1.5$ cm, and assuming the center of the sample to be at the measured temperature of 1000°C , temperatures at various

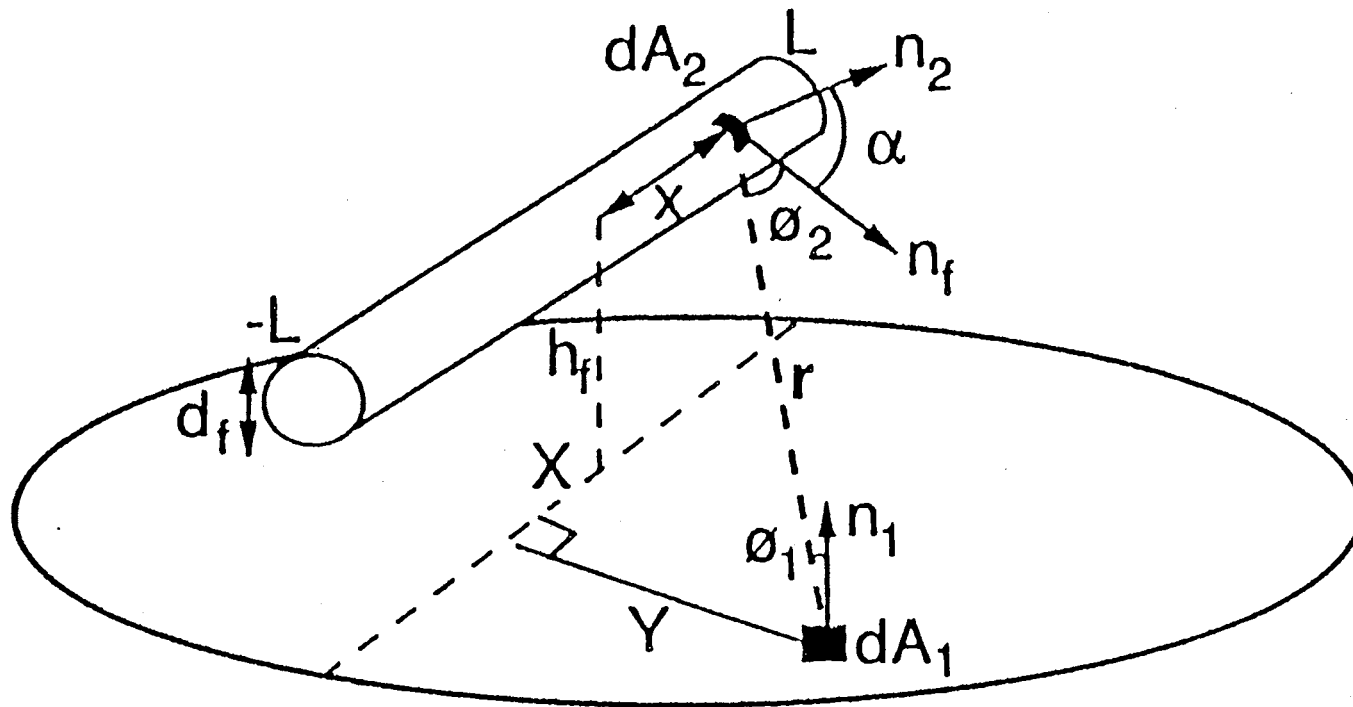


Figure 2.16. Schematic of a simple filament geometry (from Wolden, *et al.*, 1992).

points across the substrate were determined. In terms of the coordinates defined in Figure 2.16, the regions of darker and lighter grains located perpendicularly outward from the center of the filament axis are at (0 cm, 0.3 cm, 0 cm) and (0 cm, 0.5 cm, 0 cm). At these locations, the temperatures were respectively found to be 950°C and 870°C, of which the latter of these is substantially less than the temperature measured at the sample center.

Because the filament-to-substrate distance, h_f , makes as large a contribution to the temperature profile as the distance Y from the sample center, the shape factor is quite sensitive to the distance between the filament and substrate. As a result, an error of even 1 mm in the measurement of the filament-to-substrate distance can significantly change the temperature gradients between the outer rings and the sample center. This can be seen in Figure 2.17, where temperature profiles across the sample have been plotted for $h_f = 5, 6,$ and 7 mm. Note that as the filament-to-substrate distance approaches infinity, the temperature gradient across the sample goes to zero.

This sensitivity to the filament-to-substrate distance could readily explain why (100) faces on black cauliflower grains grow in narrow rings close to the sample center while silver faceted grains grow in wider rings at the outer regions of the substrate. Faceted grains of all morphologies should grow at approximately the same temperature when all other growth parameters (i.e. total flow rate, methane concentration, filament temperature, and pressure) are equal, suggesting that the filament is further from the sample when silver faceted grains are produced, with a larger portion of the sample at the ideal temperature. Black cauliflower grains with (100) faces are most likely produced with the filament closer to the substrate, whereby large temperature gradients across the sample produce a preponderance of cauliflower growth both radially inward and outward from these grains.

The sensitivity of the substrate temperature profile to the filament-to-substrate distance is further complicated by the fact that tungsten filament carburizes upon exposure to carbon at high temperatures. This carburization causes an expansion of the filament, so that as time passes, the filament-to-substrate distance is decreased. Carburization also affects the amount of carbon reaching the sample, having the greatest effect in the first hour of use of a new filament.

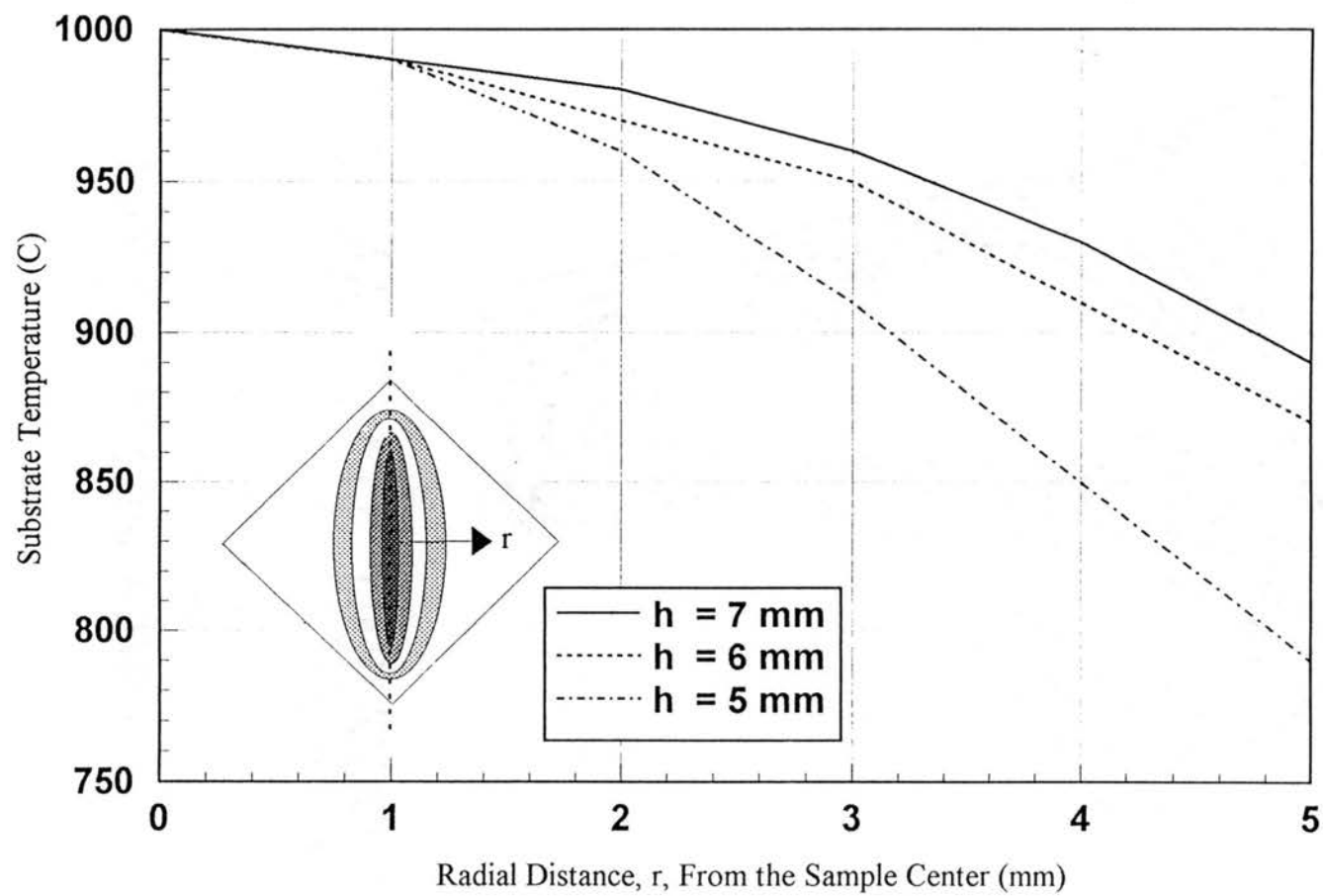


Figure 2.17. Temperature profiles across the silicon substrate for filament-to-substrate distances, h_f , of 5, 6, and 7 mm.

Chapter Summary

In this portion of the study, diamond grains produced by filament-assisted CVD were evaluated using micro-Raman spectroscopy, whereby quality and laser-responsiveness were determined as a function of morphology and shading. More faceted grains, with narrower peak widths, were found to have the highest quality and largest domains of tetrahedral sp^3 bonding. Grains lighter in color were seen to heat the least, as they contained smaller amounts of graphitic defects and absorbed less laser light.

From an analysis of deposition parameters, methane concentration and temperature were concluded to have the greatest effects on grain morphology and quality. Higher methane-to-hydrogen ratios coincided with higher levels of disorder, since less atomic hydrogen was available to remove graphitic carbon. Temperature gradients across the silicon substrate were seen to be quite sensitive to the filament-to-substrate distances and, as a result, significantly different grains were produced when all other growth parameters were roughly equal. Total flow rates were found to have no noticeable effect on grains.

In proceeding to laser annealing studies with a thorough understanding of grain morphologies and characteristics, the most obvious choices for preliminary annealing experiments are the darker grain types -- black cauliflower grains with and without shiny inclusions and black cauliflower grains with (100) faces. These grains frequently vaporized or showed largely downshifted Raman peaks when exposed to 500 mW output laser power, indicating that significantly high temperatures are indeed attainable -- if not at 500 mW, then at higher laser powers.

The existence of a wide assortment of grain morphologies with varying levels of domain sizes, graphitic defects, and impurities is a favorable occurrence in this study. By examining the effects of laser annealing on the various grain types, much can be learned about the way grains are formed and how they are bonded to the substrate.

CHAPTER III

CVD DIAMOND GRAIN QUALITY ENHANCEMENT BY POST-PRODUCTION LASER ANNEALING

Introduction

This portion of the study is motivated by two previous studies which have shown that CVD diamond films may be significantly improved by furnace annealing. By exposing diamond films to an O₂ atmosphere at 800°C, Uchida *et al.* were able to see significant improvements in the structures of the films, with only disordered *sp*² and *sp*³ carbon Raman peaks present before the 30 minute annealing period replaced by high quality diamond peaks afterwards [24]. SEM photographs in Uchida's study reveal a great deal of mass loss in the annealing process, with an initially smooth cauliflower surface etched until only jagged fragments remained. From these findings, Uchida concluded that non-diamond carbon forms can be selectively removed from CVD diamond films by oxygen annealing [24].

Research by the author of the present paper has additionally shown that the optical properties of CVD diamond films are remarkably improved after tube furnace annealing in nitrogen at 700°C [25]. After several hours of annealing, films showed sharper band gaps, more closely resembling the almost vertical 5.45 eV band gap of natural diamond, and increased transmission coefficients. Films experienced some degree of mass loss in the annealing process, which was attributed to the removal of non-diamond components in the outer layers of the films.

Encouraged by the combined results of furnace annealing and the heating and/or vaporization of grains observed with exposure to 500 mW laser light of 514.5 nm, this portion of the study focuses on single grain quality enhancement by laser annealing. It is hypothesized that grains in the atmosphere heated to temperatures between 700 and 800°C by laser exposure should be improved in a manner similar to those which have been furnace annealed at the same temperature in either oxygen or nitrogen. The

laser annealing of grains has the added advantage of in situ Raman analysis, which provides information on the time scale of the conversion process as well as on the structure, quality, and temperature of both the CVD diamond grains and the underlying silicon substrate. With this information and SEM photographs, much can be concluded about the effects of annealing on the different grain types, the silicon substrate, and the diamond/silicon interface.

Experimental Method

Grains chosen for annealing were picked from the forty-four samples examined in Chapter II. As each grain was selected, its morphology, size, and surroundings were noted and the initial laser power to which the grain was exposed was based on the percentage of grains vaporized for the given grain type -- 50 mW for black cauliflower grains with shiny inclusions, 200 mW for all cauliflower grain types, and 500 mW for silver cauli-faceted and faceted grains and black cauliflower grains with (100) faces. Using the 100x microscope objective, Stokes and anti-Stokes Raman scans of the grain were taken in the sp^3 peak region from 1250 to 1400 cm^{-1} and in the silicon peak region from 500 to 540 cm^{-1} . These scans were incremented by 0.25 and 0.1 cm^{-1} , respectively, with integration times as follows: 0.2 s for all Stokes scans, 1.0 s for anti-Stokes sp^2/sp^3 scans, and 0.5 s for anti-Stokes silicon scans. The four monochromator slits were always set at 200 μm .

Changes in the laser power were made in a controlled stepwise fashion, with two distinct procedures used in the preliminary and secondary stages of the study. In the preliminary stage, the laser power was successively increased by 20 to 100 mW, with the magnitude of the increment dependent on the absorptiveness of the grain. These successive increases in the laser power were repeated until either the maximum attainable laser power was achieved or the grain changed, visually or by unusual behavior in the Raman data. In secondary experiments, the laser power was increased in steps of 50 to 200 mW and returned to the initial laser power setting between each higher-powered scan. This procedure of increasing and decreasing the laser power was repeated until either the grain vaporized or the maximum laser power was achieved.

In analyzing the Raman data, all scans were converted from Prism ISA to ASCII files and evaluated using Jandel's Scientific Peakfit software. Peaks were best fit using a Voight profile and attempts were made to maximize the coefficient of determination, r^2 . This number, which ranges from zero to one (with one indicating a perfect fit to the data), was typically 0.99 or better for Stokes spectra and 0.98 or better for anti-Stokes spectra in the diamond peak region. The difference in r^2 values between Stokes and anti-Stokes data occurred because the ultimate value for r^2 is dependent not only on the fit, but also on the signal to noise ratio of the scan, which is considerably lower for anti-Stokes Raman components. The r^2 values for the silicon spectra varied significantly -- from 0 to 0.99 or better, depending on the thickness and absorptiveness of the covering diamond grain. r^2 values as low as 0.9 were permitted for fits of anti-Stokes diamond and silicon spectra, but only when the low r^2 value could be attributed to reduced signal-to-noise ratios.

All Stokes and anti-Stokes Raman peak positions, widths, and intensities obtained by fitting were entered into spreadsheets in Stanford Graphics software. Here, sample temperatures were calculated using the ratio of the anti-Stokes and Stokes peak intensities derived in Chapter I:

$$\frac{I_A}{I_S} = \frac{(\nu_o + \nu_{nk})^4}{(\nu_o - \nu_{nk})^4} e^{-h\nu_{nk} / kT},$$

where I_A and I_S are the anti-Stokes and Stokes intensities, ν_o is the frequency of the incident laser light, ν_{nk} is the phonon frequency, and T is the temperature of the sample in degrees Kelvin. Using Stanford Graphics software, diamond and silicon peak positions and widths were studied as a function of temperature and in relation to each other. Raman spectra from clean silicon and natural diamond were used as controls.

Results and Discussion

It was seen in Chapter II that the seven categories of CVD diamond grains respond quite differently to an output laser power of 500 mW, depending on their quality and absorptiveness. This was also clearly evident in the present chapter, where black and dark gray grains were much more sensitive to laser exposure than silver ones. Some black cauliflower grains could not withstand even the minimum

output laser power of 50 mW, while many silver faceted grains were heated by less than 50°C using the maximum 2.0 W laser power. As a result, grain types are not equally represented in this portion of the study, with the majority being the more responsive black cauliflower grains with or without shiny inclusions and with (100) faces. Nevertheless, all categories are indeed represented.

SEM photographs of two CVD grains laser-annealed in this study are shown in Figure 3.1(a-b). A cauliflower grain is shown in Figure 3.1(a), where the outer layers of growth have been removed by laser annealing to reveal a radially-varying distribution of diamond growth. Gradations in color reflect changes in the electrical conductivity of the grain, as well as changes in morphology, since both these variables affect the levels of secondary electron emissions which reach the detector. The dark and light regions on the unannealed grains in the lower portion of the picture are believed to be from surface roughness, rather than changes in conductivity, since the profile of the annealed grain is jagged, rather than smooth. On the other hand, the color changes in the exposed inner layers of the annealed grain are attributed to changes in conductivity, since depth studies using the optical microscope after annealing reveal indentation. The darker regions of the grains are found to be more electrically conductive (and more graphitic), as determined from graphite/diamond comparisons with the SEM. Thus, the grain is believed to contain higher levels of sp^2 bonding at distances further from the center, with the exception of the extreme outer surface. This outer layer most probably contains large amounts of hydrogen and dangling carbon bonds.

An annealed cauli-faceted grain is shown in Figure 3.1(b), with the inset showing the annealed grain above a neighboring unannealed grain for comparison. In this case, the conductivity is seen to be essentially uniform throughout the annealed grain, attributed to the presence of large domains of single-crystal diamond and reduced levels of graphitic bonding. The annealed grain is believed to be lighter in color than the unannealed grain because some portion of graphitic bonds have been selectively removed. Since this grain has a much higher diamond content than the cauliflower grain, it experiences less mass loss in the annealing process.

In comparing the Raman characteristics of grains as a function of temperature, all categories were found to exhibit similar trends in Raman behavior. The vibrational frequency of the $k \approx 0$ optic

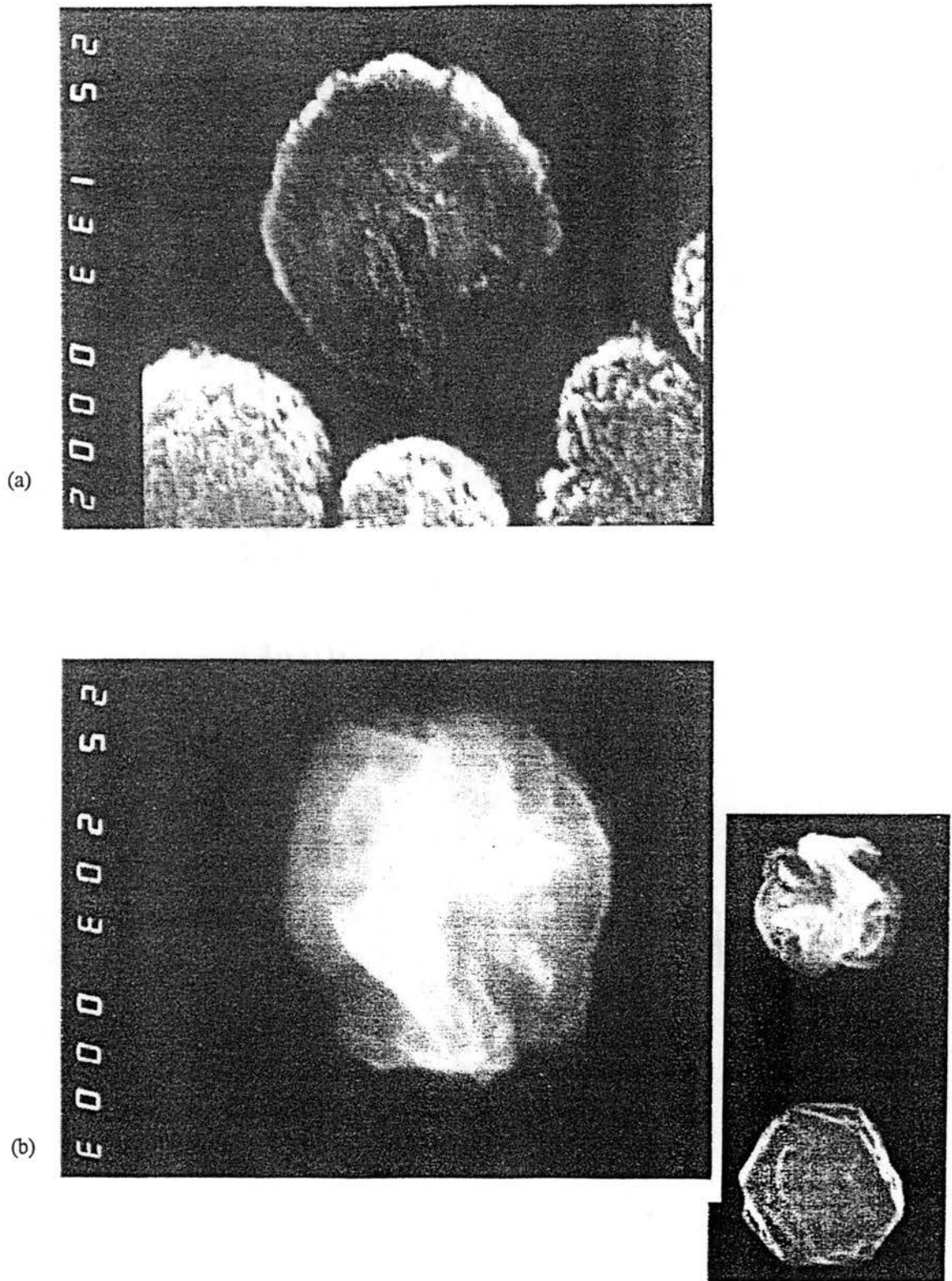


Figure 3.1. SEM photographs of laser-annealed (a) cauliflower and (b) cauli-faceted CVD diamond grains. The inset shows grain (b) above an unannealed cauli-faceted grain for comparison.

phonon of diamond was always seen to become more downshifted at higher temperatures, as shown in Figure 3.2, but *never* dropped below 1319 cm^{-1} . When the diamond peak reached this position and the grains were exposed to higher laser powers, they were seen to either become lighter in color or vaporize. Those grains which vaporized subsequently showed a complete absence of Raman peaks between 1250 and 1400 cm^{-1} , while those which became lighter showed diamond peaks which were situated *closer* to the position of natural diamond rather than being further downshifted. From the ratio of the anti-Stokes-to-Stokes intensities, this reverse shift in peak position was found to correspond to a drop in grain temperature. The two extremes of vaporization and conversion seen to occur with laser annealing suggest that there is a narrow temperature range over which grain conversion takes place and that only slightly beyond this range grains turn to carbon dioxide.

The temperature dependence of the conversion or vaporization of grains was confirmed by laser annealing neighboring grains using different laser power increments. Grains exposed to small increases in laser power were able to survive exposure to much greater laser powers than those exposed to high powers in larger increments. In this way, grains which initially reached 1319 cm^{-1} at several hundred milliwatts could be progressively converted in repeated heatings until they eventually withstood even the maximum achievable laser power of 2.0 W . Each time the conversion temperature was reached, the grain would become somewhat lighter in color and cool off and the process could be repeated all over again. Upon exposing identical grains situated less than a micron away to laser powers increased in somewhat larger increments, grains were seen to vaporize at much lower laser powers. These grains, not given adequate time to convert, absorbed too much energy, reached intolerable temperatures, and were destroyed rather than converted to a lighter color.

The Universal Temperature Dependence of the $k \approx 0$ Optic Mode Frequency of CVD Diamond Grains

As discussed in Chapter I, anharmonic interactions between the vibrational modes of a crystal cause the frequency of vibration of a given mode to shift from its position at absolute zero at increased temperatures. In comparing the behavior of the $k \approx 0$ optic mode frequencies of CVD diamond grains as a function of temperature, all data points, regardless of grain or category, were found to fall on a universal

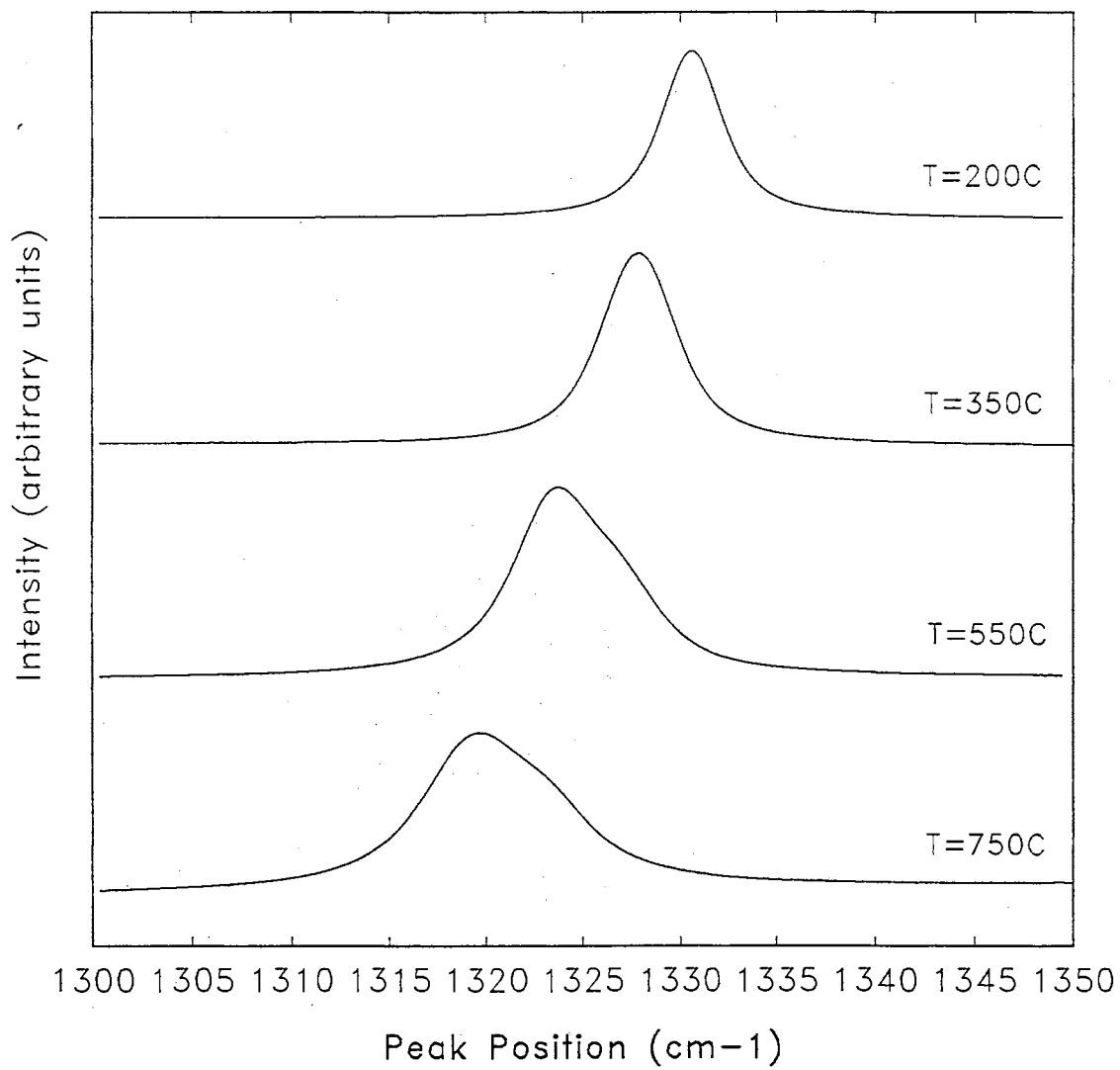


Figure 3.2. The downshifting and broadening of the Raman diamond peak with increased temperatures. From top to bottom, temperatures are roughly 200, 350, 550, and 750°C.

curve. This curve, shown in Figure 3.3, extends from 100 to 900°C and behaves in an approximately exponential fashion.

Although it is not obvious from the graph, the individual grain curves showed discontinuous behavior above 700°C, where the curve leveled off. No diamond grains were seen to reach temperatures above 900°C, as this temperature corresponded to the peak position of roughly 1319 cm^{-1} . These findings suggest that the conversion process occurs between 700 and 900°C and that temperatures above 900°C result in grain vaporization. In comparing the peak position vs. temperature curves before and after grain conversion, no differences could be seen. Even though much greater laser powers were needed to reach the same temperature after annealing, all data points still fell on the same curve. This suggests that the fundamental structure of the diamond lattice is not changed in the conversion process.

As the peak positions of grains approached 1319 cm^{-1} , many unusual spectra were seen, with anti-Stokes-to-Stokes intensity ratios sometimes yielding ludicrous temperatures of 2000°C to 3000°C. These bizarre temperatures were attributed to the dramatic increases in the scattering intensity which occurred with conversion and the ordering of Stokes scans before anti-Stokes scans. By comparing trends in the Stokes and anti-Stokes backgrounds, the conversion process was found to take place over several minutes. Depending on the initial temperature to which grains were raised, 10 to 40 minutes elapsed before the grain temperature dropped below the conversion temperature range and the intensity of the background signal leveled off. In contrast, vaporization was seen to occur in less than one second.

Because grains cool as they are converted and the diamond peak consequently moves closer to the position of natural diamond in the process, the shapes of the Stokes and anti-Stokes diamond peaks could be compared to determine the validity of each pair of spectra. Since both Stokes and anti-Stokes peaks arise from photon interactions with the same vibrational mode, the magnitude of the Raman energy shift and the uncertainty in the energy should be identical for both processes. As a result, those Stokes and anti-Stokes pairs with peak positions and/or widths which disagreed with each other by more than 1.0 cm^{-1} were thrown out. These acceptance criteria were applied to all scans in the study.

On many occasions, the diamond peak was seen to split into *two* distinct peaks at energies below 1330 cm^{-1} , as illustrated in Figure 3.4. This splitting could, in theory, be attributed to either a breaking

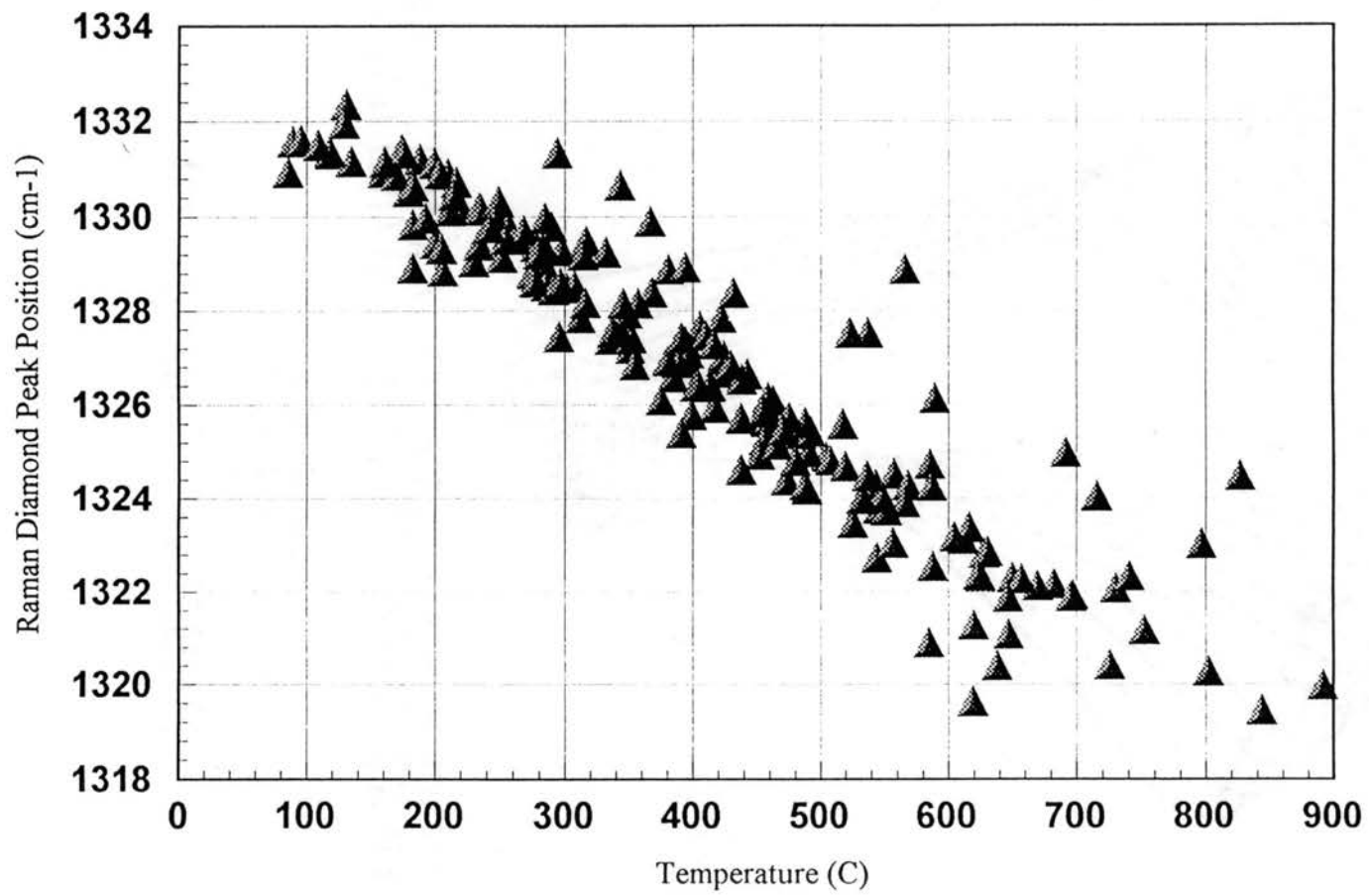


Figure 3.3. The universal diamond peak position vs. temperature curve for all CVD diamond grains in this study.

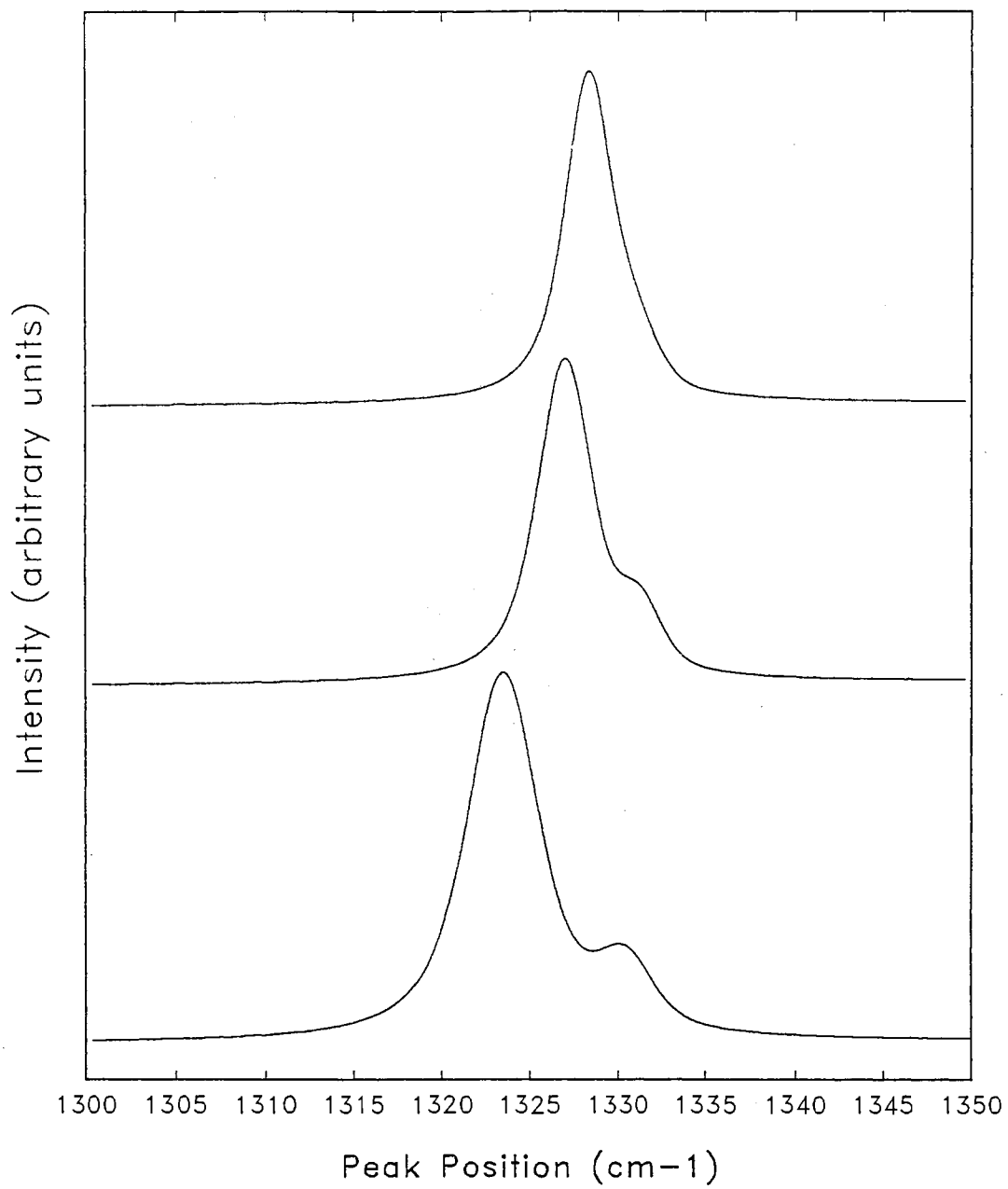


Figure 3.4. The splitting of the diamond peak with increased temperatures.

of the crystal symmetry or the presence of two distinct regions of diamond at different temperatures. However, in fitting these spectra with Jandel's Scientific Peakfit software, which essentially finds its own peak positions and widths, the Stokes/anti-Stokes pairs which met the acceptance criteria always showed the more downshifted peak to be at a higher temperature than the peak closer to 1332.5 cm^{-1} . Both peaks also fell on the same universal peak position vs. temperature curve, essentially confirming the validity of the doubly-peaked spectra. Although the splitting of the diamond peak does seem unusual, it is most likely a result of the extremely heterogeneous nature of the CVD diamond grains.

Evaluation of the Grüneisen Parameter for CVD Diamond Grains The temperature dependence of Raman scattering in crystals originates not only from the anharmonic interactions between phonons, but also from the thermal expansion of the crystal. Although thermal expansion itself occurs as a result of anharmonicity, it affects the quasi-harmonic frequencies through the harmonic force constants which may depend on the crystal volume. The Grüneisen parameter, γ , discussed in Chapter I, provides a means of measuring the magnitude of the Raman shift due *entirely* to changes in the crystal volume. The Grüneisen parameter of the i^{th} mode, γ_i , is defined as

$$\gamma_i \equiv -\frac{V}{\omega_i} \frac{d\omega_i}{dV},$$

where V is the volume of the crystal and ω_i is the frequency of the i^{th} vibrational mode [19]. Since $\omega_i = \omega_i(T, P)$, this may be equivalently written as

$$\gamma_i \equiv -\frac{V}{\omega_i} \left\{ \left(\frac{\partial \omega_i}{\partial T} \right)_P \frac{dT}{dV} + \left(\frac{\partial \omega_i}{\partial P} \right)_T \frac{dP}{dV} \right\}.$$

When the pressure is kept constant, as is the case in the present experiment, the second term vanishes. In addition, the volume coefficient of thermal expansion,

$$3\alpha = \frac{1}{V} \left(\frac{\partial V}{\partial T} \right)_P,$$

[19] may be substituted, so that γ_i becomes

$$\gamma_i = -\frac{1}{3\alpha} \frac{1}{\omega_i} \left(\frac{\partial \omega_i}{\partial T} \right)_P.$$

Separating this equation and integrating both sides from 0 to T, we obtain the temperature dependent frequency shift due to the thermal expansion of the lattice:

$$\omega_i(T) = \omega_i(0)e^{(-3\gamma_i \int \alpha(T)dT)}$$

The temperature dependent thermal expansion coefficient for diamond is given by

$$\alpha = (8.7 \times 10^{-7} / \text{K}) + (9.228 \times 10^{-9} / \text{K}^2)(T - 273\text{K}) + (6.99 \times 10^{-10} / \text{K}^3)(T - 273\text{K})^2,$$

[53], which may be inserted into the expression for $\omega_i(T)$ and evaluated. The peak position vs. temperature curves for all CVD diamond grains may then be fit by adjusting the Grüneisen parameter, γ_i , and the zero-temperature peak position, $\omega_i(0)$.

Fits to the individual grain data were best made using Grüneisen parameters ranging from 0.8 to 1.2 and zero-temperature peak positions of 1330.5 to 1333 cm^{-1} . These values for γ are within the bounds of the experimentally-determined values of γ for natural diamond, which range from 0.9 ± 0.1 to 1.2 ± 0.1 [54, 55, 56]. Figure 3.5 shows the universal curve for all experimental data fit using the equation for the thermal expansion-based shift with $\gamma = 0.9$ and $\omega(0) = 1331.5 \text{ cm}^{-1}$. In this graph, the discontinuous behavior of the curve above 700°C can clearly be seen, where this behavior is most likely due to anharmonic contributions to the frequency shift, which become more pronounced at higher temperatures. Nevertheless, the close agreement between the data and the theoretical curve suggests that changes in grain volume are the dominant cause of the vibrational frequency shift in diamond. Also, the excellent fit obtained using the Grüneisen parameter of 0.9, equaling that of natural diamond, reveals that the net strain on the diamond lattice is zero. Because all CVD diamond grains in this study show essentially the same frequency shift at a given temperature, the position of the diamond peak can be used as a temperature probe, which may be quite useful when the anti-Stokes signals are obscured by noise.

The anharmonic interactions which directly and indirectly give rise to the temperature-dependence of vibrational frequencies are also responsible for the temperature-dependent behavior of Raman linewidths. Increases in temperature produce larger phonon populations in all modes of the crystal, which interact with each other through the quasi-harmonic interactions of the lattice. These increased interactions with the other modes of vibration reduce the lifetime of diamond's optic mode and,

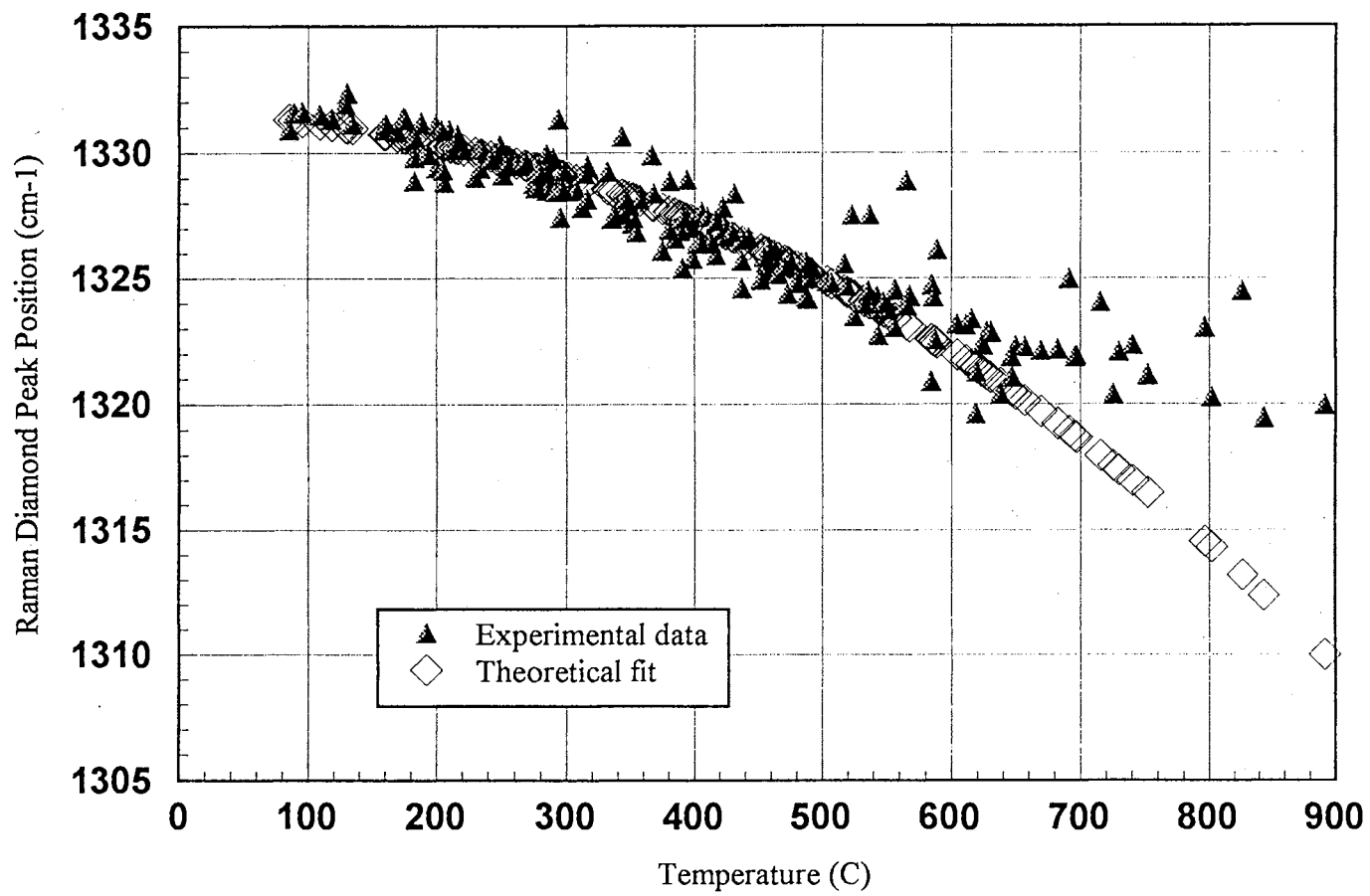


Figure 3.5. The universal diamond peak position vs. temperature curve fit to the equation for the volume-expansion shift.

through Heisenberg's uncertainty principle, this results in an increase in the linewidth of the diamond peak.

The Irreversible Hysteresis of the Diamond Peak Width with Grain Conversion

Unlike the universally temperature-dependent diamond peak position, the width of the diamond peak varied drastically as a function of temperature between different grain types and even between scans of the same grain before and after conversion. This is because the peak width is not only dependent on temperature, but also on the force constants of the crystal, which may be perturbed by defects and impurities, which produce localized strains in each unit cell. Since a large collection of unit cells take part in Raman scattering ($\sim 1 \times 10^5$), the peaks are actually a superposition of the Raman spectra produced by each unit cell, which may be vibrating at slightly different frequencies due to inhomogeneous strains. Because the force constants are intrinsic to the crystal structure, they may only be changed by changing the crystal itself.

A typical peak width vs. temperature curve is shown in Figure 3.6, where the width of the peak is clearly seen to increase with temperature. All peak widths have been corrected to zero slit width using the method of the diffraction limiting study described in Chapter II, in which the intrinsic (zero-slit setting) width of natural diamond was found to be 1.0 cm^{-1} less than the width measured using the experimental $200 \text{ }\mu\text{m}$ slit settings. The corrected peak widths for grains ranged from 1.7 to 10 cm^{-1} at 100°C , with black cauliflower grains with (100) faces having the narrowest widths and silver grains the largest. These linewidths are much smaller than the average widths obtained in Chapter II, not only because of the zero-slit width correction, but also because the lighter colored grains, which had average peak widths of 14 to 23 cm^{-1} , tended to be unresponsive to laser light and frequently could not be heated beyond 500°C .

Theoretical fits were obtained for the peak width vs. temperature curves for all grains using the three-phonon interaction model [57], in which the optic phonon of diamond is restricted to decay into two phonons of lower energy. By the conservation of energy and momentum, the optical phonon, having wavevector $\mathbf{k} \approx 0$ and frequency ω_0 , can decay into these two phonons, with wavevectors \mathbf{k}_1 and \mathbf{k}_2 and frequencies ω_1 and ω_2 , only if

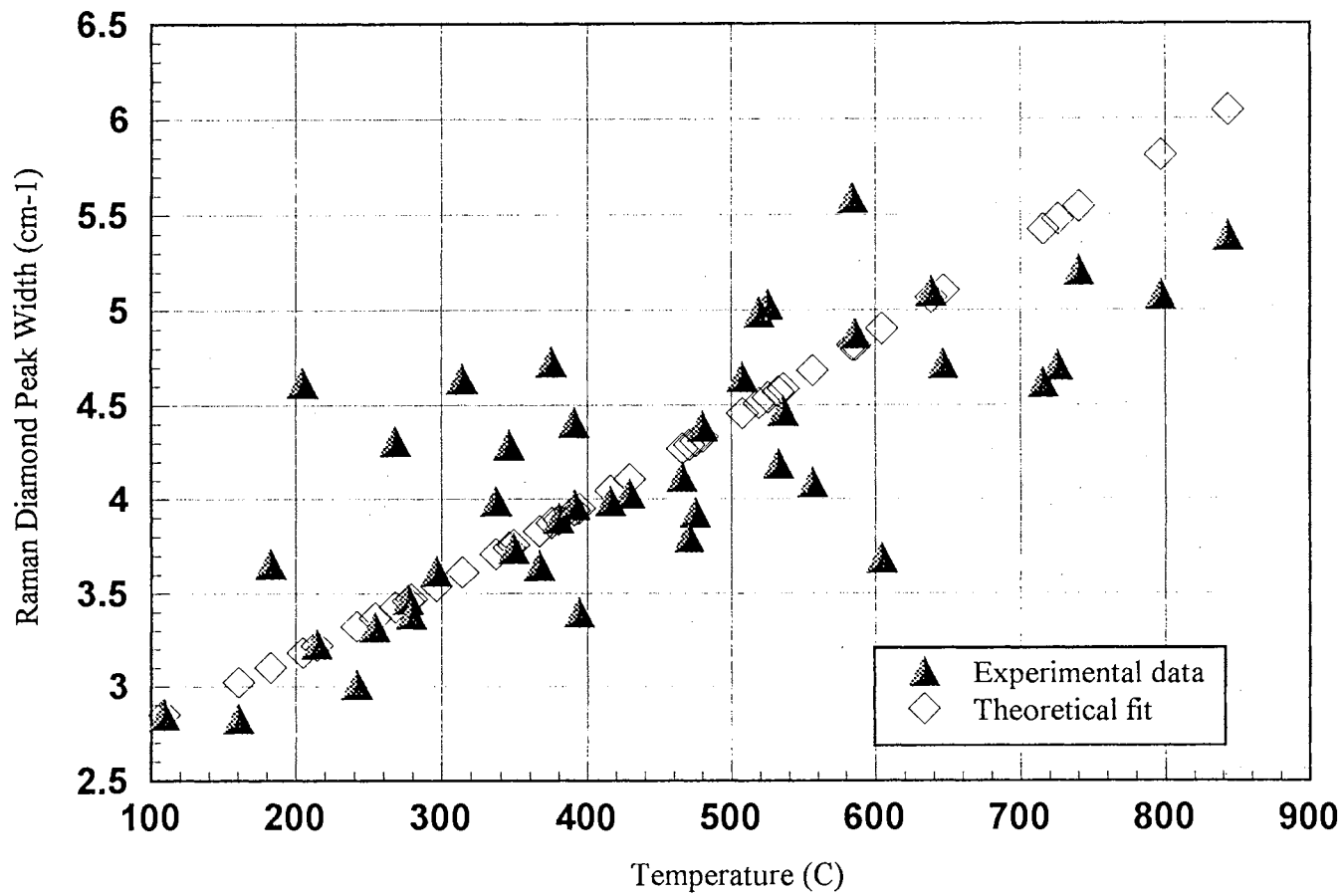


Figure 3.6. Typical diamond peak width vs. temperature curve for CVD diamond grains in this study. Data is fit using the three-phonon interaction model.

$$\omega_o = \omega_1 + \omega_2$$

$$\text{and } \mathbf{k}_2 = -\mathbf{k}_1.$$

Upon examination of the phonon dispersion curves of diamond displayed in Figure 2.3, there are six possible decay channels which obey these selection rules: $(O) \rightarrow (LA, LA)$, (TA_1, TA_1) , (TA_2, TA_2) , (LA, TA_1) , (LA, TA_2) , or (TA_1, TA_2) , where LA and TA respectively denote longitudinal and transverse acoustic phonons and the 1 and 2 subscripts refer to the two possible polarizations of the TA phonons. The contribution to the peak width from each of these mechanisms is obtained in the same manner, so that it suffices to examine the general problem of decay into two arbitrary acoustic phonons and then apply the particulars for each specific case.

Denoting the occupation numbers of the optical and two arbitrary acoustic phonons respectively by n_o , n_1 , and n_2 , the only non-zero components of H' for the three-phonon interaction are

$$\langle n_o - 1, n_1 + 1, n_2 + 1 | a_o a_1^+ a_2^+ | n_o, n_1, n_2 \rangle$$

$$\text{and } \langle n_o + 1, n_1 - 1, n_2 - 1 | a_o^+ a_1 a_2 | n_o, n_1, n_2 \rangle.$$

In thermal equilibrium, the transition probabilities for the first term, representing the decay of one optic phonon into two acoustic phonons, and the second term, representing the recombination of two acoustic phonons to produce one optic phonon, are equal. Thus,

$$\frac{d \langle n_o, n_1, n_2 \rangle}{dt} \propto n_o (n_1 + 1)(n_2 + 1) - (n_o + 1)n_1 n_2 = 0.$$

However, if a small perturbation, ε , is placed on the equilibrium population of the optic mode, the relaxation rate of the system is given by

$$\frac{d \langle n_o, n_1, n_2 \rangle}{dt} \propto (n_o + \varepsilon)(n_1 + 1)(n_2 + 1) - (n_o + \varepsilon + 1)n_1 n_2,$$

which, after subtracting out the thermal equilibrium part, becomes

$$\frac{d \langle n_o, n_1, n_2 \rangle}{dt} \propto \varepsilon(1 + n_1 + n_2).$$

This expression is valid for all six decay mechanisms listed above. However, since the TA_1 and TA_2 curves are for the most part degenerate, we will make the simplification $TA_1 = TA_2$ so that there are

only (LA,LA), (TA,TA), and (LA,TA) processes to consider. In the cases where (O) \rightarrow (LA,LA) or (TA,TA), the energies of the acoustic phonons must be equal, and as a result, so must the occupation numbers n_1 and n_2 . In the case where (O) \rightarrow (LA,TA), the energies of the two acoustic phonons are not equal, but may be found from the phonon dispersion curves to be approximately 800 cm^{-1} (LA) and 533 cm^{-1} (TA).

When all decay mechanisms are considered, the resulting relaxation rate is given by a weighted sum of the decay terms. The relaxation rate and linewidth are directly related to each other through the uncertainty principle, $\Delta E \Delta t = \hbar/2$, so that, when all processes are equally weighted, the expression for the temperature-dependence of the linewidth is given by

$$\Gamma(T) = \frac{\Gamma(0)}{5} \left[3 \left(1 + \frac{2}{e^{\hbar\omega_o/2kT} - 1} \right) + 2 \left(1 + \frac{1}{e^{\hbar\omega'/kT} - 1} + \frac{1}{e^{\hbar\omega''/kT} - 1} \right) \right],$$

where $\Gamma(0)$ is the peak width at absolute zero, $\hbar\omega' = 800 \text{ cm}^{-1}$, and $\hbar\omega'' = 533 \text{ cm}^{-1}$. The curve shown in Figure 3.6 has been fit using $\Gamma(0) = 2.4 \text{ cm}^{-1}$, with a standard deviation between the data points and the theoretical fit of 0.53 cm^{-1} . Most peak width vs. temperature curves were fit using $\Gamma(0)$ values ranging from 1.2 to 4.0 cm^{-1} with standard deviations of 0.3 to 0.6 cm^{-1} .

On many occasions, grains were seen to experience an irreversible hysteresis of the peak width vs. temperature curve after reaching the conversion temperature range. As these grains lightened in color, the width of the diamond peak was seen to become significantly narrower than those previously measured *at the same temperature*. This is illustrated in Figure 3.7, in which the linewidth of the diamond peak follows the upper curve before the conversion and the lower curve afterwards. These two curves have respectively been fit using the same $\Gamma(0)$ value of 3.0 cm^{-1} , but the upper curve has an additional constant of 5.1 cm^{-1} added to it, attributed to the presence of inhomogeneous strain broadening which is removed in the conversion process. A set of "before and after" Raman spectra for the given grain is shown in Figure 3.8, where both scans have been taken at roughly 560°C . The peak is obviously narrower after conversion.

An equally interesting observation was made for grains which initially lacked any detectable diamond signal but showed a broad disordered sp^3 peak. When these grains were heated to the

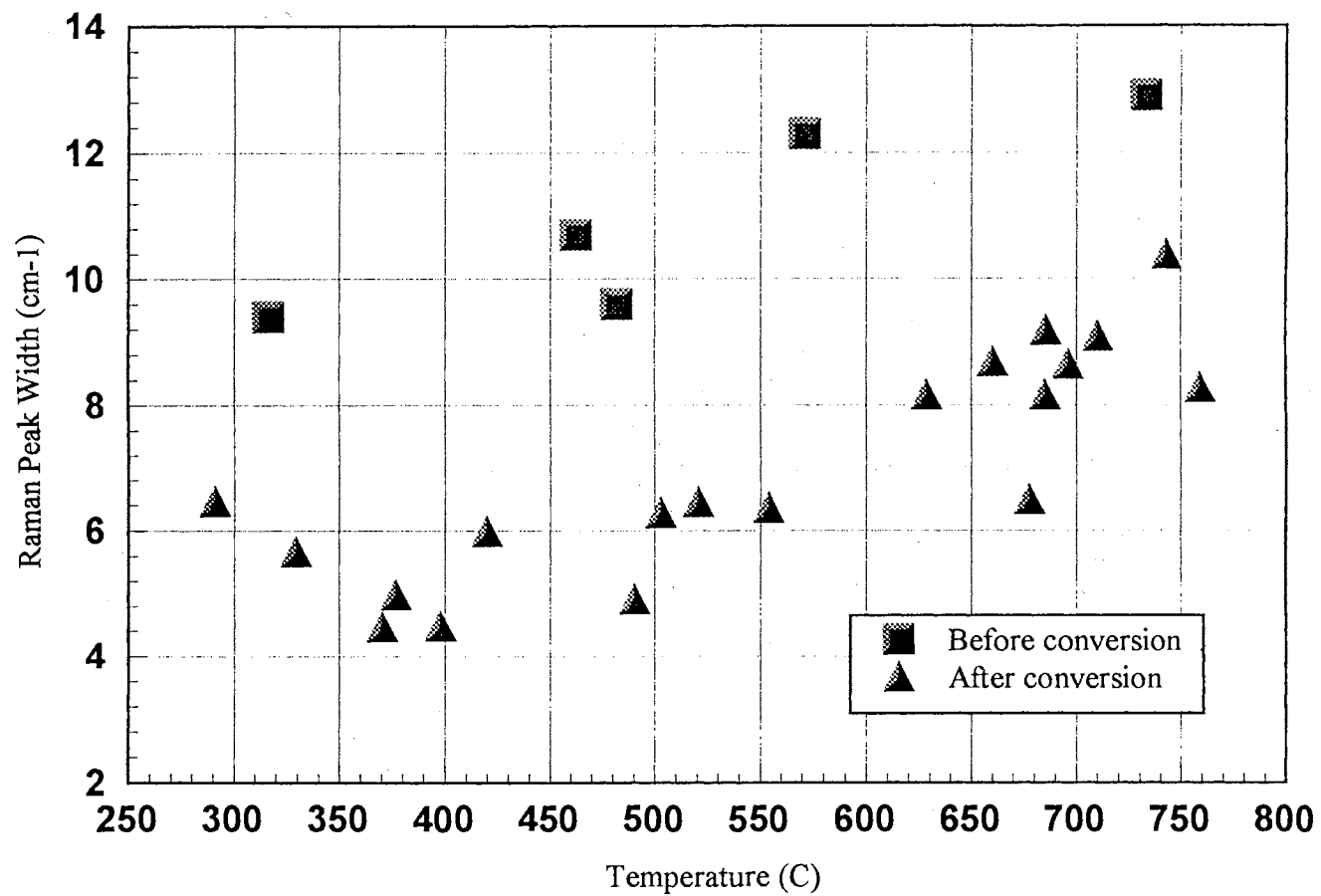


Figure 3.7. Irreversible hysteresis of the diamond peak width vs. temperature curve which occurred with grain conversion. All data points are taken from the same grain, before and after conversion.

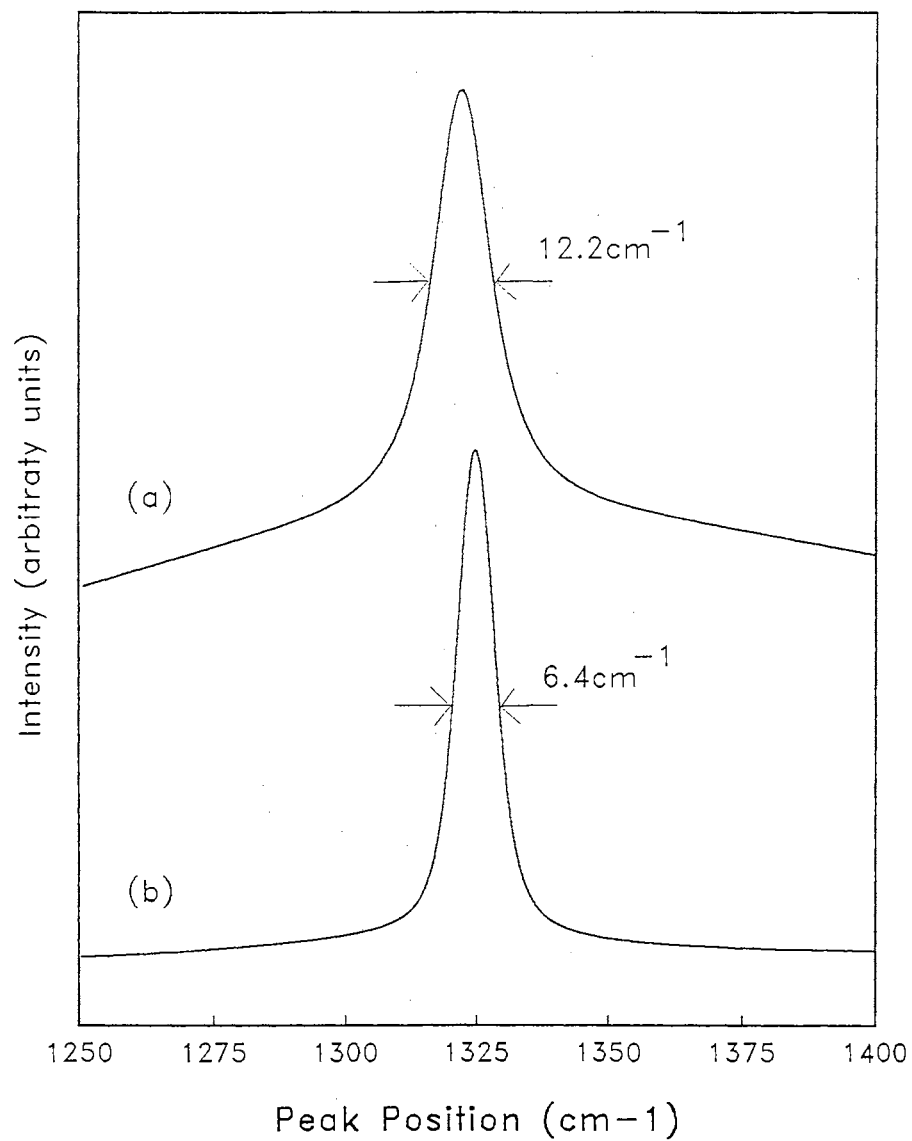


Figure 3.8. Raman spectra taken (a) before and (b) after the conversion-induced hysteresis shown in Figure 3.7. Both spectra, with respective widths of 12.2 cm^{-1} and 6.4 cm^{-1} , are taken at a temperature of roughly 560°C .

conversion temperature range, a diamond peak rose out of the broad sp^3 band and became more prominent with further exposure to temperatures above 700°C . An example of this is shown in Figure 3.9, where all scans are taken at roughly 700°C over a period of 3 hours. In the final scan, the diamond peak has a width of 5.9 cm^{-1} . This process could have been further repeated and the diamond grain even more improved had laser powers greater than 2.0 W been attainable.

The reduction in the linewidth of the diamond peak with the conversion process is certainly the result of the selective removal of impurities and defects from a pre-existing diamond lattice. At temperatures above 700°C , some portion of these effects are removed, as seen by the reduction in the width of the diamond peak and the mass losses of the converted grains in the SEM photographs. Since poorer quality grains have higher levels of defects and impurities, their potential for improvement is significantly greater than those grains with peak widths of $2\text{ to }4\text{ cm}^{-1}$. However, it could be very well be that higher quality grains are in fact improved, but that the changes are within the standard deviation of the data and are thus undetectable.

Increases in the Scattering Intensity of the Diamond Peak with Grain Conversion

In comparing Raman scans taken at the same temperature before and after grain conversion, the scattering intensity of the diamond peak is seen to increase significantly in the conversion process, sometimes by more than an order of magnitude. This result is shown in Figure 3.10, where scans are taken at the same laser power before and after conversion. Equal laser powers, rather than equal temperatures, have been considered, since the higher laser power needed to obtain the same temperature after conversion would itself cause the intensity to increase. The intensity of the underlying silicon peak was also seen to increase with the conversion, as were the disordered sp^2 and sp^3 peaks, although to a much lesser degree.

By examining the theoretical expression for the scattering intensity, an explanation for the increase in diamond peak intensity can be found. In the backscattering configuration, with spatial coordinates as defined in Figure 3.11, the scattering intensity at the surface of the sample is given by

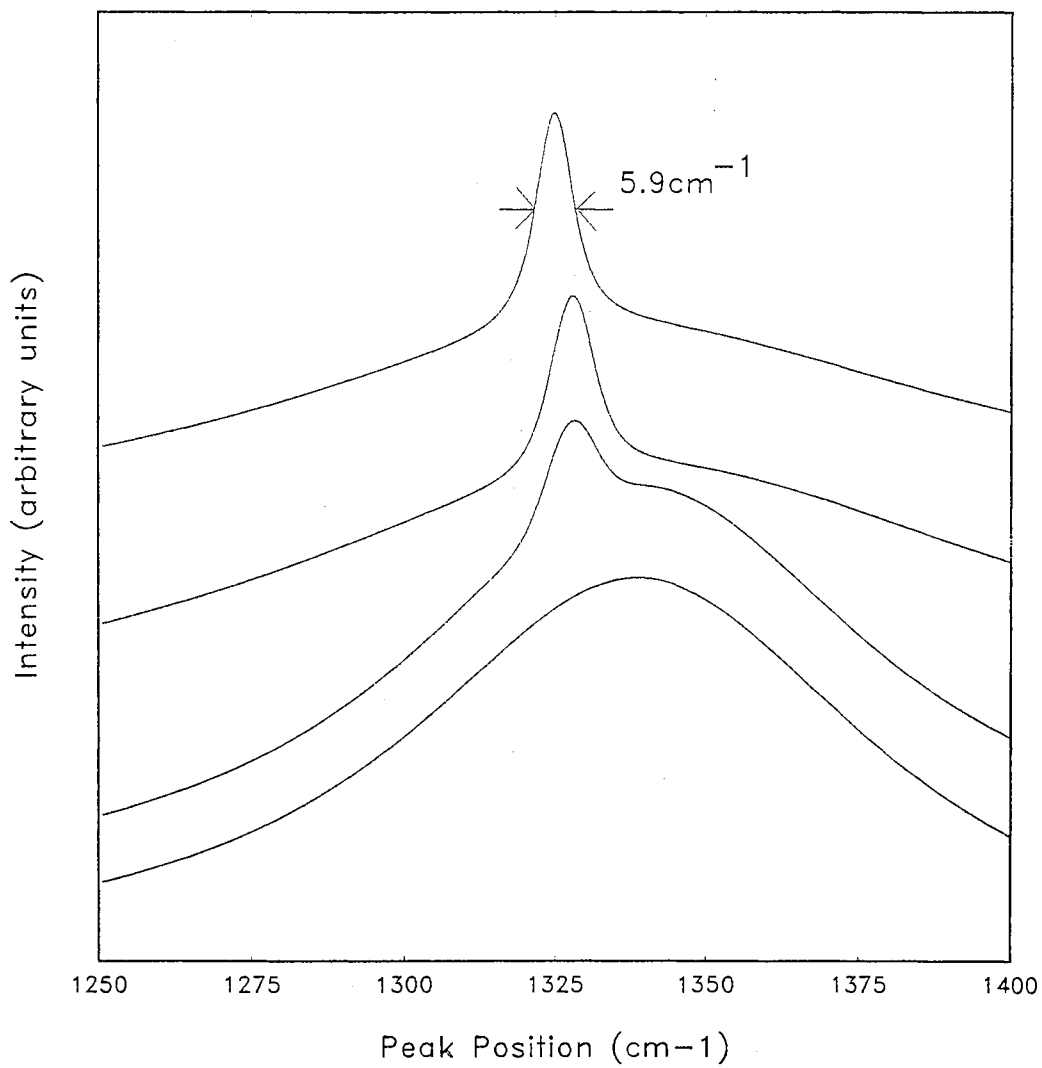


Figure 3.9. The uprising of the diamond peak from out of the disordered *sp*³ background with grain conversion. All scans are taken at roughly 700°C.

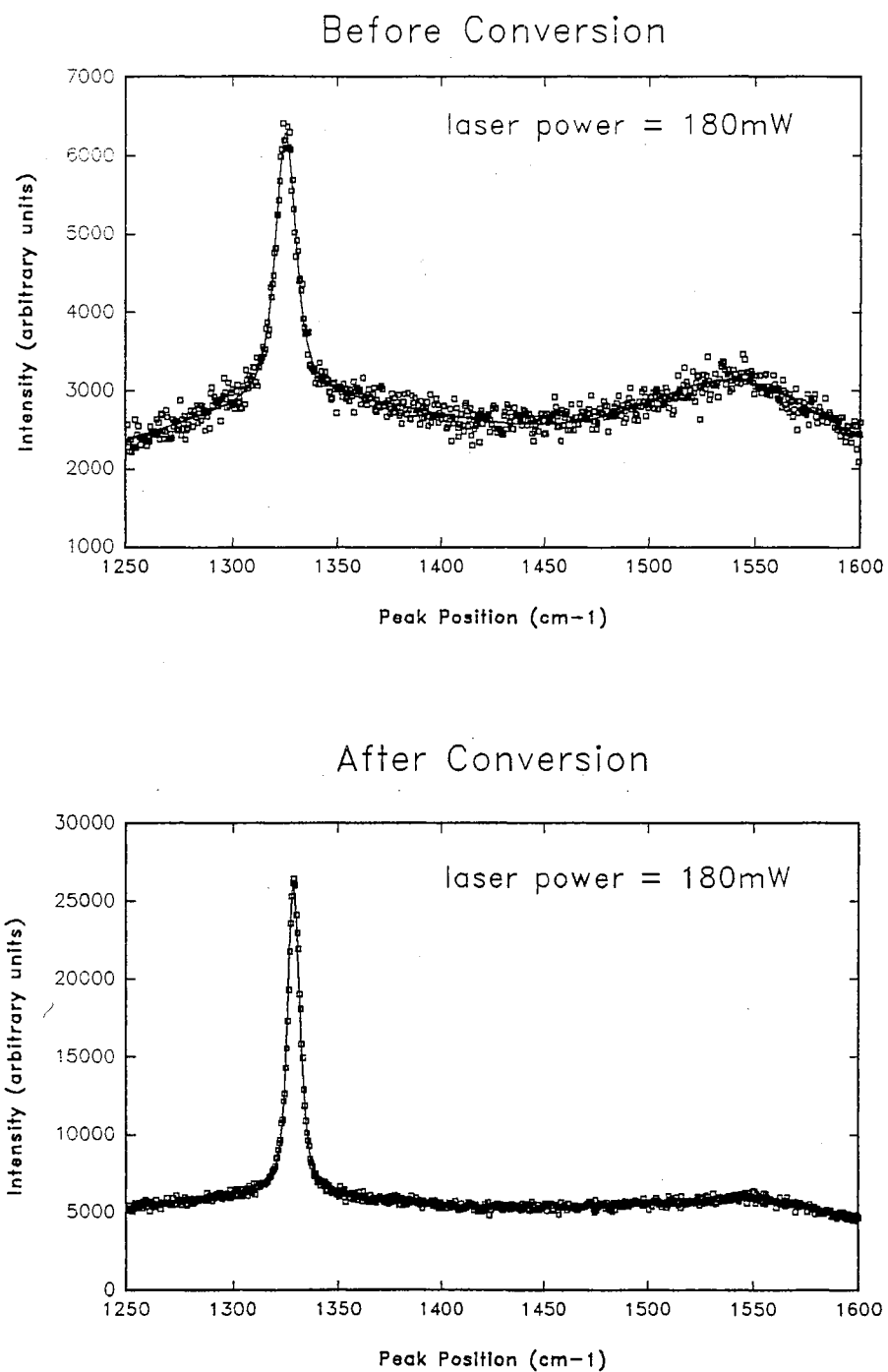


Figure 3.10. A typical example of the increase in scattering intensity seen upon grain conversion. Both scans are taken at a laser power of 180 mW

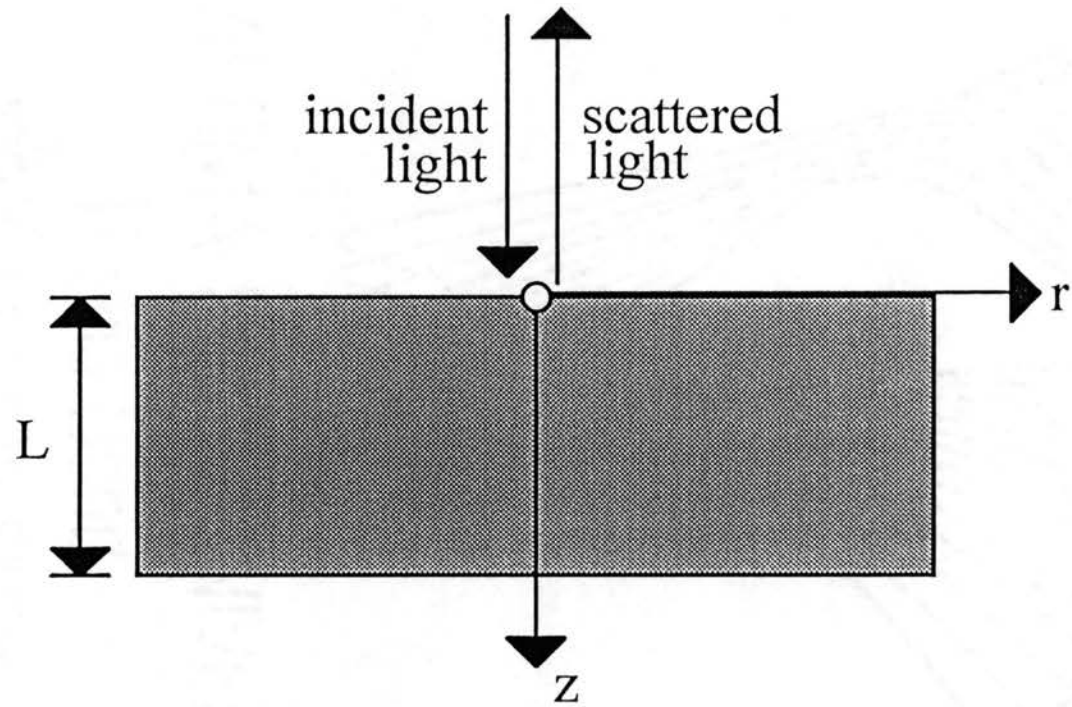


Figure 3.11. Spatial coordinates in the backscattering configuration.

$$I(0) = \eta I_0 \frac{[1 - e^{-(\eta + \alpha_0 + \alpha)L}]}{(\eta + \alpha_0 + \alpha)}$$

where η is the Raman efficiency, I_0 is the intensity of the incident radiation, and α_0 and α are the absorption coefficients at the frequencies of the incident and scattered light, ω_0 and $\omega_0 \pm \omega_k$ [58]. This relation is derived from the differential equations for the spatial dependencies of I_0 and I :

$$\frac{dI_0(z)}{dz} = -\eta I_0(z) - \alpha_0 I_0(z),$$

$$\frac{dI(r, z)}{dr} = -\alpha I(r, z),$$

$$\text{and } \frac{dI(0, z)}{dz} = \eta I_0(z),$$

subject to the boundary condition $I(0, 0) = 0$.

The Raman efficiency, defined as the ratio of the number of observed Raman-scattered photons produced per unit cross-sectional area of the crystal per unit time to the number of exciting photons incident on the sample per unit area per unit time, is shown in Appendix D to be

$$\eta = K \frac{\hbar(\omega_0 - \omega_k)^4 d\Omega}{\mu\omega_k} |\alpha_R|^2 (n_k + 1),$$

for Stokes scattered radiation, where K is a constant, $(\omega_0 - \omega_k)$, is as defined above, α_R is the Raman polarizability, and μ is the reduced mass. For the anti-Stokes component, $(n_k + 1)$ and $(\omega_0 - \omega_k)$ are replaced by n_k and $(\omega_0 + \omega_k)$ respectively. The Raman efficiency is strongly dependent on the frequency of the incident light and on the temperature of the sample.

The only variables in the intensity equation which vary significantly between scans taken at the same laser power before and after conversion are the absorption coefficients α_0 and α , and the Raman polarizability α_R . Changes in the frequency, and reduced mass are minimal, as are the changes in $(n_k + 1)$, since the temperature typically drops by 100 to 300°C in the conversion. Thus, the most significant contributions must come from α_0 , α , and/or α_R .

The dramatic lightening of grains and drop in temperature observed upon conversion indicate that it is the absorption coefficients, α_0 and α , which are predominantly responsible for increases in the scattering intensity. However, the role of sp^2 -bonded carbon as the only absorber is clearly incorrect,

since the intensity of the sp^2 peak is seen to increase as much as the disordered sp^3 peak with conversion. Grain absorption must therefore additionally be attributed to the presence of hydrogen inclusions and weakly-bonded hydrocarbon impurities, the levels of which are reduced as grains are heated beyond 700°C.

Studies of the Underlying Silicon Substrate and the Diamond/Silicon Interface

For each pair of Stokes and anti-Stokes Raman spectra taken in the disordered sp^3 /diamond peak region, a pair of Stokes and anti-Stokes spectra were also obtained in the silicon peak region from 500 to 540 cm^{-1} . The vibrational frequency and linewidth of the $k \approx 0$ optic mode of silicon were examined as a function of temperature and gradients between the diamond and silicon temperatures measured before and after annealing were compared. From these studies, much was learned about the effects of grain conversion on the silicon substrate and the composition of the interface connecting the diamond grains to the silicon.

As can be seen in Figure 3.12, the vibrational frequency of the $k \approx 0$ optic mode of silicon behaves in a manner very similar to that of diamond. The peak is downshifted from the usual position of 520 cm^{-1} at increased temperatures and all data points, obtained both before and after conversion, fall on the same universal curve. This common behavior, seen in cauliflower grains with and without (100) faces and in silver cauli-faceted and faceted grains, suggests that the *net* strain on the silicon lattice is identical for all grain types and that this strain is not affected by the conversion process.

On several occasions, two or more peaks were seen in the silicon spectra -- a result of the diamond grain under examination being narrower than the laser beam and/or containing several domains with different levels of absorptiveness. The silicon not covered by diamond remained at roughly room temperature at all laser powers, being so massive that it essentially acted as an infinite heat sink. In contrast, the covered silicon heated considerably, responding as though a hot poker had been placed on its surface. Since the data points for all doubly-peaked silicon spectra which met the acceptance criteria fell on the universal silicon peak position vs. temperature curve, these spectra were considered legitimate.

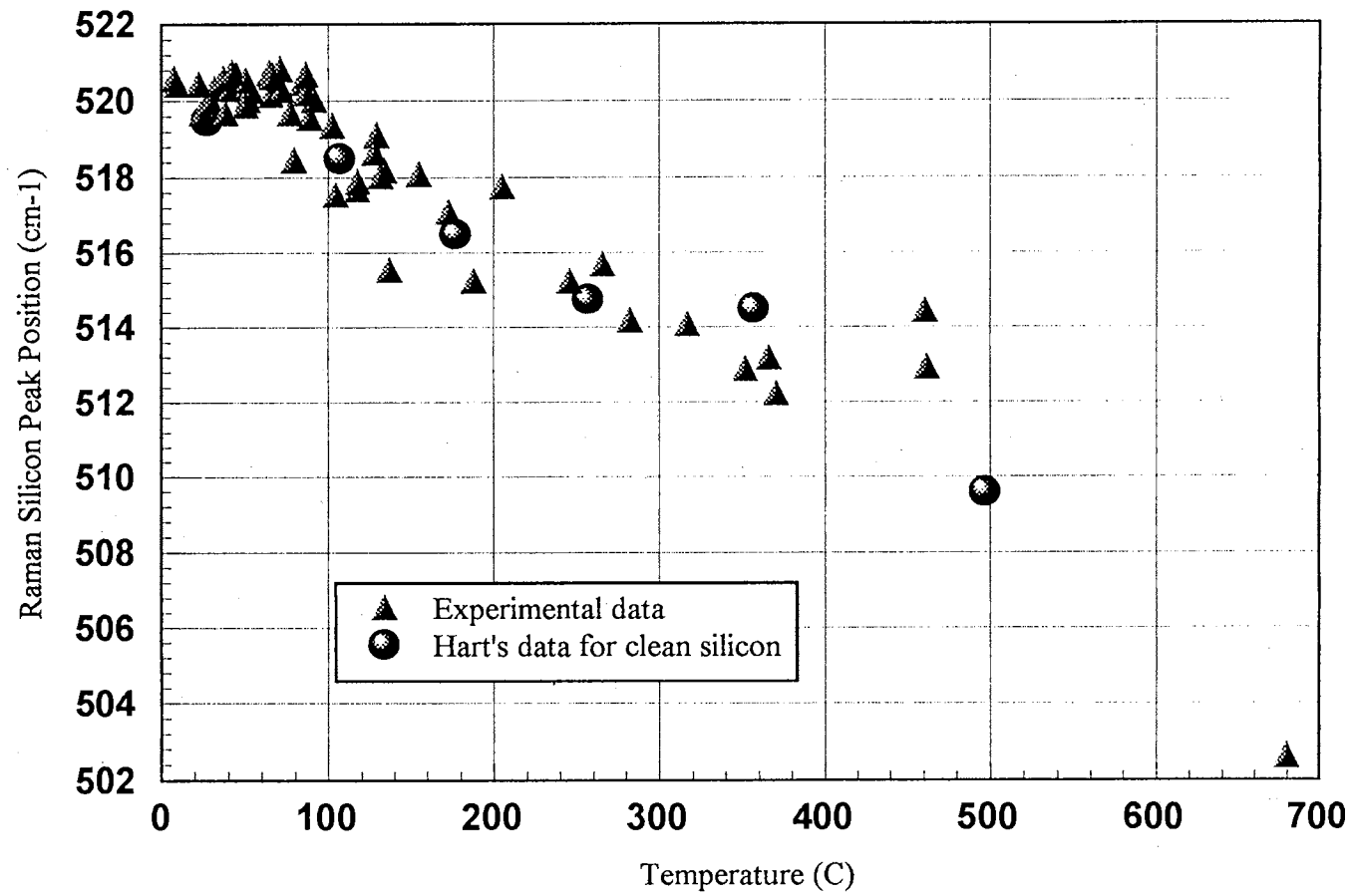


Figure 3.12. The universal silicon peak position vs. temperature curve for the silicon substrate beneath CVD diamond grains. Hart's data for clean silicon is included for comparison.

As a verification of the experimental method, the results of a similar study by Hart *et al.* [59] have been included in Figure 3.12, where in Hart's study, Raman spectra were obtained from polished (111) silicon substrates heated in a furnace from 25 to 500°C. The two sets of data clearly fall upon the same curve, indicating not only that the net strain on the silicon beneath the diamond grains is zero but also that the method of temperature determination used in this study is indeed accurate.

The width of the silicon peak is plotted as a function of temperature in Figure 3.13, where the data points for all grains with acceptable silicon spectra have been included. At any given temperature, the distribution of linewidths is seen to extend across a narrow range, suggesting that all grains perturb the substrate in essentially the same way. Comparisons of silicon peak widths obtained from underneath the *same* grain before and after conversion (at the same temperature) reveal no significant changes in the linewidth with grain conversion, implying that there are either no strain broadening mechanisms present or that they are present but unaffected by grain conversion.

To determine which of these is the case, a theoretical fit to the linewidth curve was obtained using the three phonon interaction model [57]. For silicon, the energy and momentum selection rules limit the $\mathbf{k} \approx 0$ optic mode to decay into two longitudinal acoustic phonons of equal energy and opposite wavevector, due to an increased separation of the optic and transverse acoustic phonon modes. As a result, the temperature dependence of the width of the silicon peak is given by

$$\Gamma(T) = \Gamma(0) \left(1 + \frac{2}{(e^{\hbar\omega_o / 2kT} - 1)} \right).$$

The theoretically fit to the data using this equation has been included in Figure 3.13, with $\Gamma(0) = 2.0 \text{ cm}^{-1}$. This value for $\Gamma(0)$ was successfully used by Hart *et al.* [59] to obtain a fit to the silicon peak widths in their study, but the fit to the present data is obviously rather poor. This suggests that there are higher levels of inhomogeneous strain present in the silicon substrates of this study, most likely induced in the CVD process by the heteroepitaxial growth of diamond and possibly silicon carbide on the substrate and the diffusion of hydrogen atoms into the silicon lattice.

In comparing diamond grain temperatures with the simultaneously-obtained temperatures of the underlying silicon substrates, the grains are always seen to be at higher temperatures than the underlying

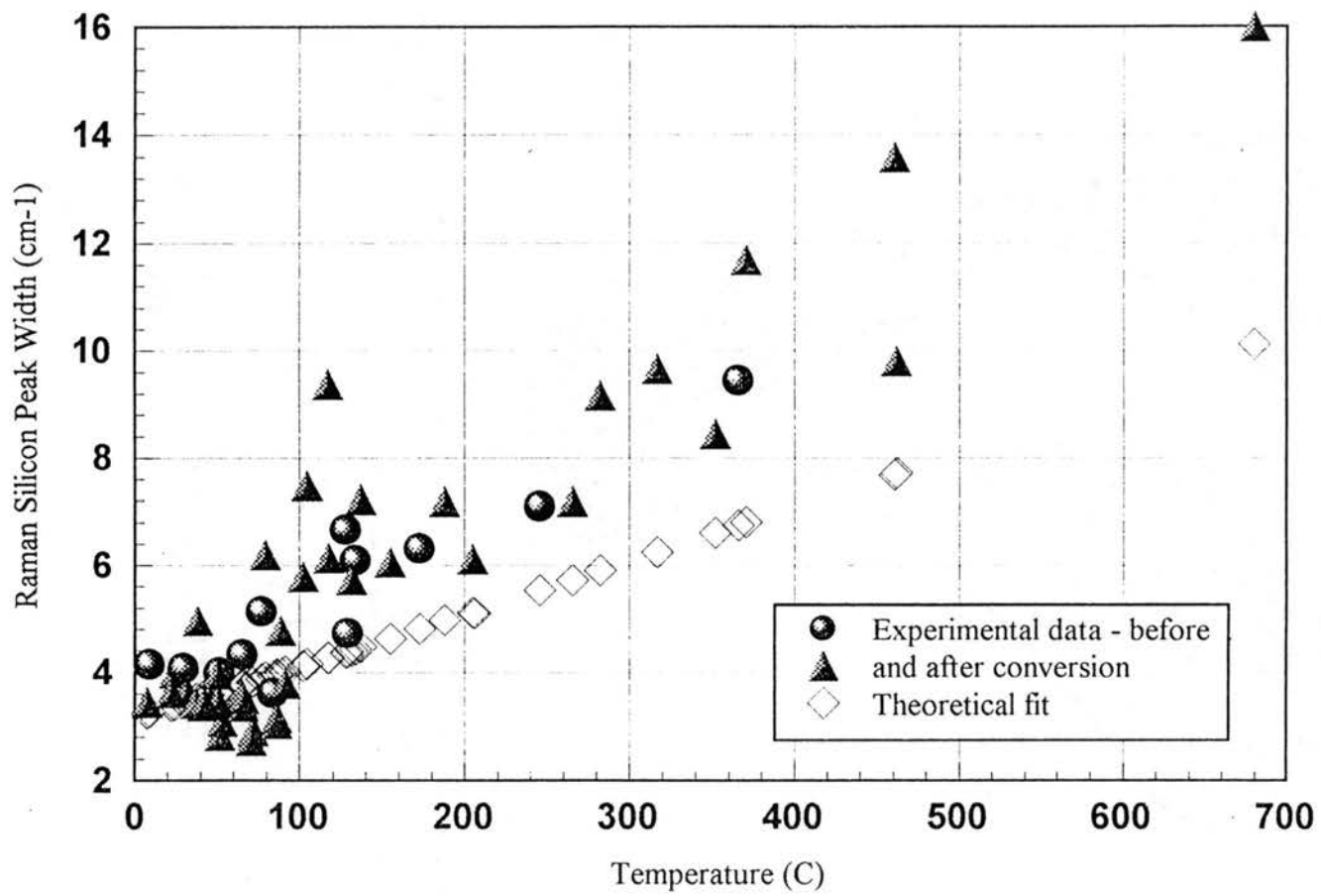


Figure 3.13. The universal silicon peak width vs. temperature curve for the silicon substrate beneath CVD diamond grains. Data is fit using the three phonon interaction model.

silicon. This result, shown in Figure 3.14, is attributed to the reflection of some portion of the thermal phonons at the interface between the two materials, where the differences in the sound velocities on either side of the boundary produce what is called a *kapitza resistance*. This “resistance”, defined by

$$R_K \equiv A \frac{\Delta T}{\dot{Q}},$$

provides a measure of phonon transmissions between solids, where ΔT and \dot{Q} are the temperature difference and heat flow across the interface of area A [60]. Data points taken before and after grain conversion reveal that the temperature gradient between the diamond and silicon increases with conversion, suggesting that the interface is somehow changed in the conversion process.

In an attempt to explain how the diamond/silicon interface is affected by conversion while perturbations on the silicon lattice are not, it is ventured that there is a Raman-invisible transition layer between the two materials, most probably silicon carbide or a layer of amorphous silicon. Several samples not included in this study for lack of diamond were indeed found to contain silicon carbide, with a Raman peak at roughly 800 cm^{-1} in agreement with the reported position [61]. These samples were grown using 1 to 2% methane and total flow rates of 100 to 200 sccm, but with substrate temperatures usually below 900°C . Large regions of yellow and blue interference patterns were frequently seen on these samples.

The possible existence of a transition layer is further strengthened by the presence of the shiny, Raman-undetectable growth at the sample centers and the interference patterns sometimes seen near the corners farthest from the filament. A transition layer of silicon carbide several hundred nanometers thick would be imperceivable by Raman spectroscopy, separate the silicon lattice from the area of conversion, and still affect the temperature gradient between the diamond and silicon as the boundary between the diamond and transition layer is altered.

Without an electron diffraction apparatus readily available to confirm or disprove the presence of a non-silicon interface, Raman spectra of the substrate were obtained at points far from any diamond growth or scratches to search for possible perturbations. These measurements proved quite worthwhile, for the silicon spectra obtained were generally asymmetric, as shown in Figure 3.15, with the mean of the peak downshifted from the maximum. These perturbations on the silicon peak were greatest at the sample

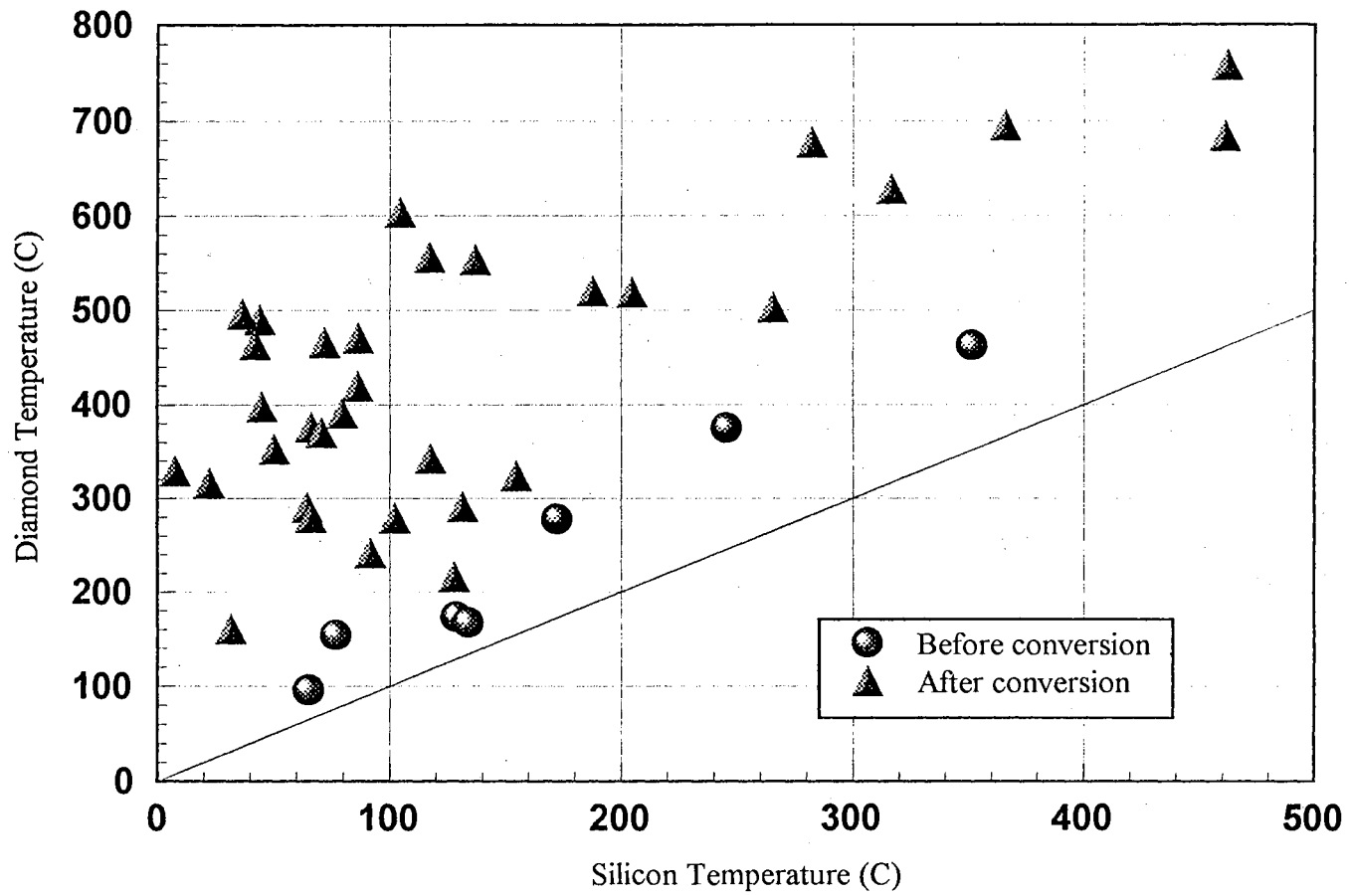


Figure 3.14. Diamond grain temperature as a function of the temperature of the underlying silicon substrate.

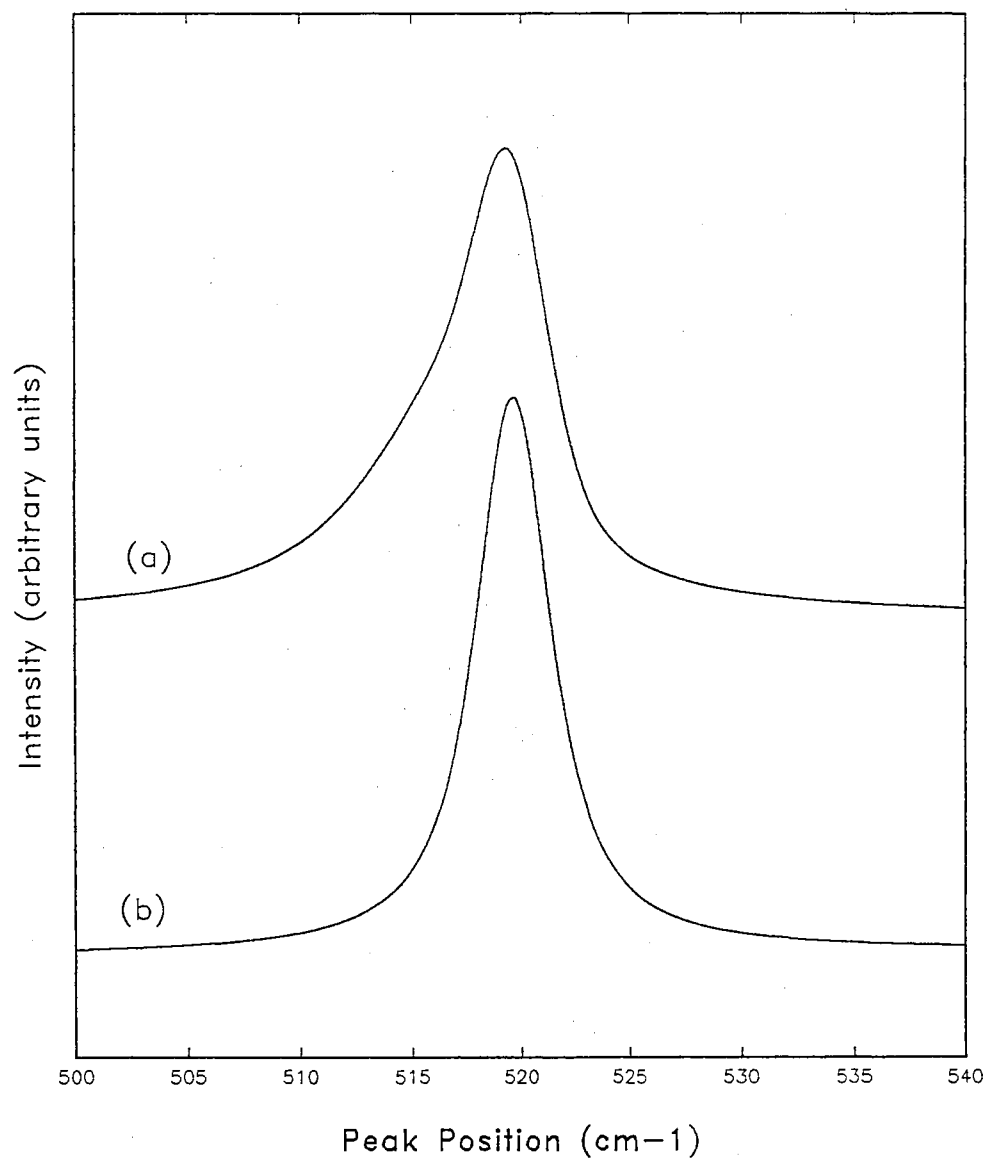


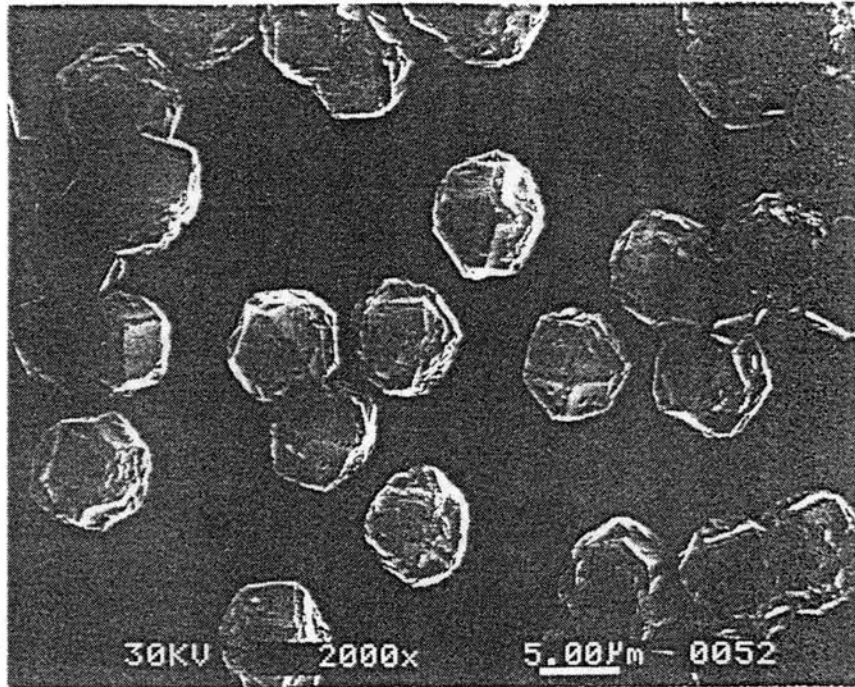
Figure 3.15. Silicon peaks obtained from (a) the exposed surface of a CVD-processed silicon wafer and (b) a clean silicon wafer, for comparison.

center and diminished at distances further out. At increased laser powers, the silicon peaks were seen to become even more asymmetric, suggesting that the perturbation is due to heating induced by phonon reflection at the interface. This would cause the layers of silicon near the boundary to be at a slightly higher temperature than the bulk material, with these layers consequently producing more downshifted Raman peaks. When the same procedure was performed on as-received and scratched *clean* silicon wafers, the silicon peak remained symmetric at all powers.

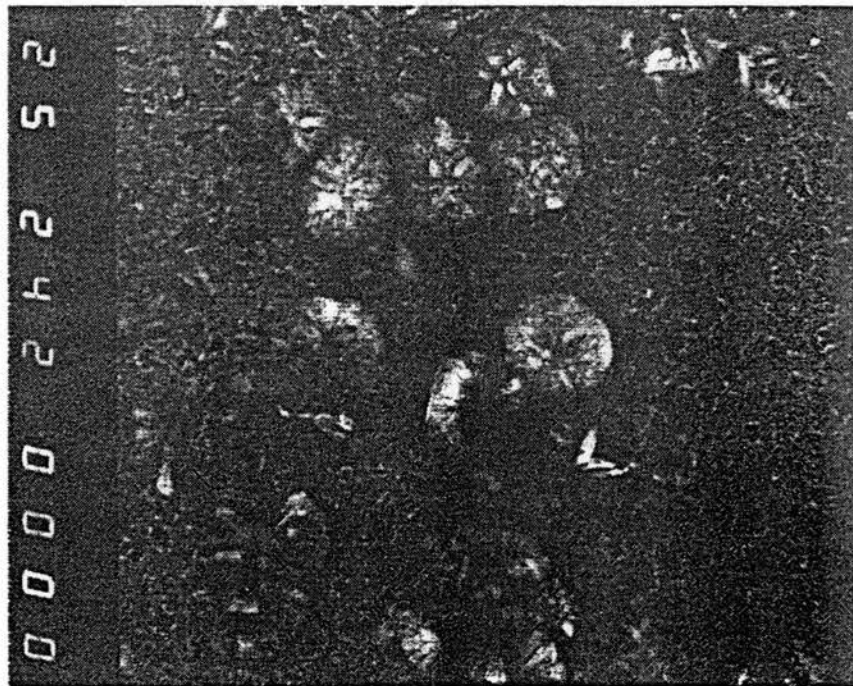
To determine whether the thickness of the transition layer is reduced in the conversion process, several samples were annealed in a tube furnace under conditions similar to those in the laser-annealing experiments. Halves of samples chosen for tube furnace annealing were exposed to a slowly moving stream of air at 700 to 800°C for a duration of 30 minutes, while the other half of the sample was kept intact for "before and after" comparisons. Although diamond grains were drastically affected by the annealing process (as discussed in the next section), the underlying silicon substrates showed no changes, either visually or in Raman behavior. The interference patterns at the clamped corners of the films remained the same, as did the asymmetric nature of the silicon peak. From these observations, it is concluded that the conversion process may affect the area of the interface and the composition of the diamond grains (which would alter the sound velocities in the grains) but does not directly affect the thickness of the transition layer. This is as would be expected for silicon carbide, which sublimates at 2700°C [45].

Tube Furnace vs. Laser Annealing

As samples were removed from the tube furnace, changes in the diamond-containing regions were immediately noticeable to the unaided eye. The concentric rings of growth were drastically lighter in color in a manner similar to the laser-annealed grains. Before and after SEM photographs of black cauliflower grains with (100) faces from the same substrate are shown in Figure 3.16, where the sample has been furnace annealed at 800°C in flowing air for 30 minutes. As seen in the close-up in Figure 3.17, the annealing process is seen to have removed large sections of some grains while leaving others intact but severely etched. These results suggest that growth is radial but that a great deal of randomness still exists.



(a)



(b)

Figure 3.16. SEM photographs of black cauliflower grains with (100) faces taken (a) before and (b) after tube furnace annealing in air at 800°C for 30 minutes.



Figure 3.17. SEM close-up of the central grain in Figure 3.16(b). Note the surviving (100) faces and needle-like growth.

Upon careful examination of the annealed grains, the flat (100) faces in the grains are seen to be less etched than the cauliflower growth.

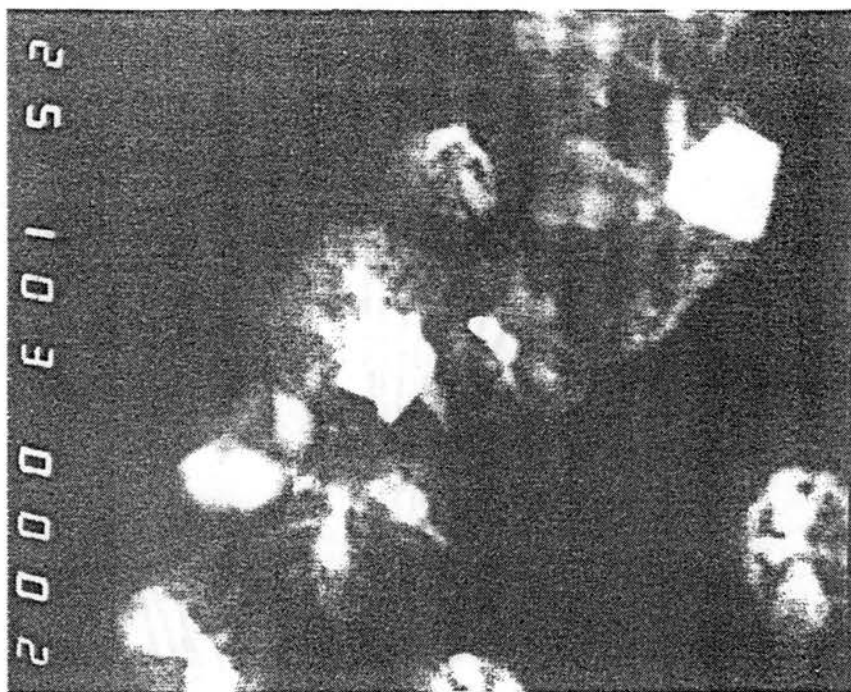
Two additional SEM photographs of tube furnace annealed grains are shown in Figure 3.18(a-b), where the first picture shows cauli-faceted grains with all but the central cores of single crystal diamond and the bases removed in annealing. The brightness in the diamond cores is attributed to lower conductivities, due to the reduced levels of graphite present in single crystal grains. On the opposite end of the morphological spectrum are cauliflower grains, shown in Figure 3.18(b). After annealing at 800°C for 30 minutes, only the small domains of diamond are seen to remain.

Raman spectra illustrating the two extremes of tube furnace grain conversion are illustrated in Figure 3.19(a-b), where grains from the same ring on the annealed and unannealed portions of the same substrate have been analyzed. From these spectra, no changes in quality are seen in grains which contain few defects and impurities to begin with, while initially inferior grains are found to improve significantly after annealing. These spectra also demonstrate that tube furnace and laser annealing produce essentially the same results, where both methods yield higher quality diamond, increased scattering intensities, and lower grain temperatures at a given laser power after heating grains to 700 to 900°C in the atmosphere.

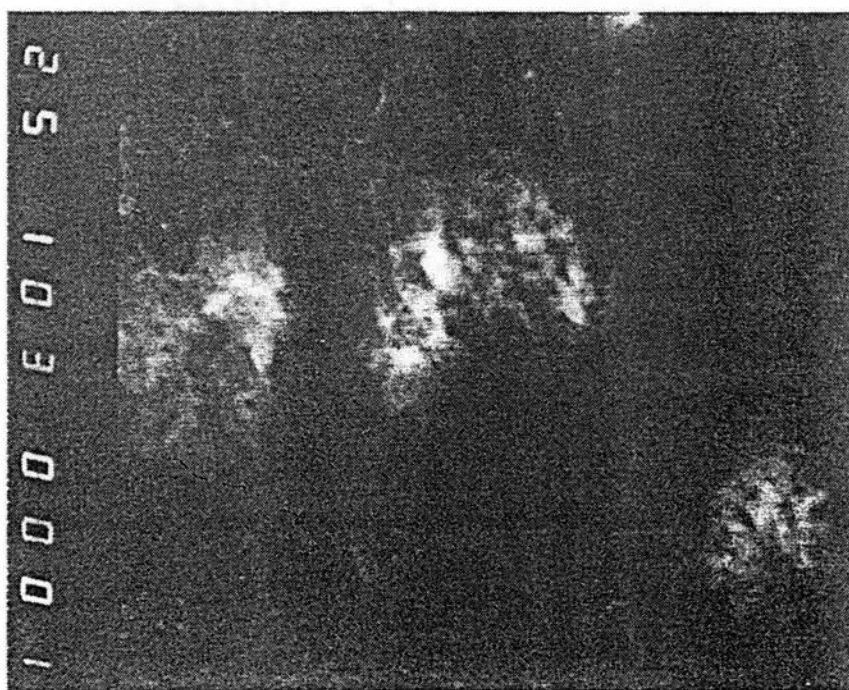
The Effects of Nitrogen on Diamond Grain Growth and Conversion

Because nitrogen forms covalent bonds and is comparative in size to carbon, it is capable of forming substitutional impurities in the diamond lattice. Because these substitutions will affect the quality and composition of diamond grains, attempts to produce and evaluate N-doped diamond have been examined. Also of interest are the comparative effects of nitrogen and oxygen annealing on diamond grains. Since oxygen is known to be much more reactive than nitrogen, the effects due to nitrogen may be overshadowed by open-air annealing. Pure nitrogen annealing is examined to account for this possibility.

Nitrogen-Doping of Diamond Grains Using the standard CVD growth procedure but with an additional 0.25 to 0.5% nitrogen added to the standard methane and hydrogen source gases, samples containing N-doped diamond grains were produced. Typical growth conditions included a total flow rate



(a)



(b)

Figure 3.18. SEM photographs of (a) cauliflower grains with (100) faces and (b) cauliflower grains after tube furnace annealing in air at 800°C for 30 minutes.

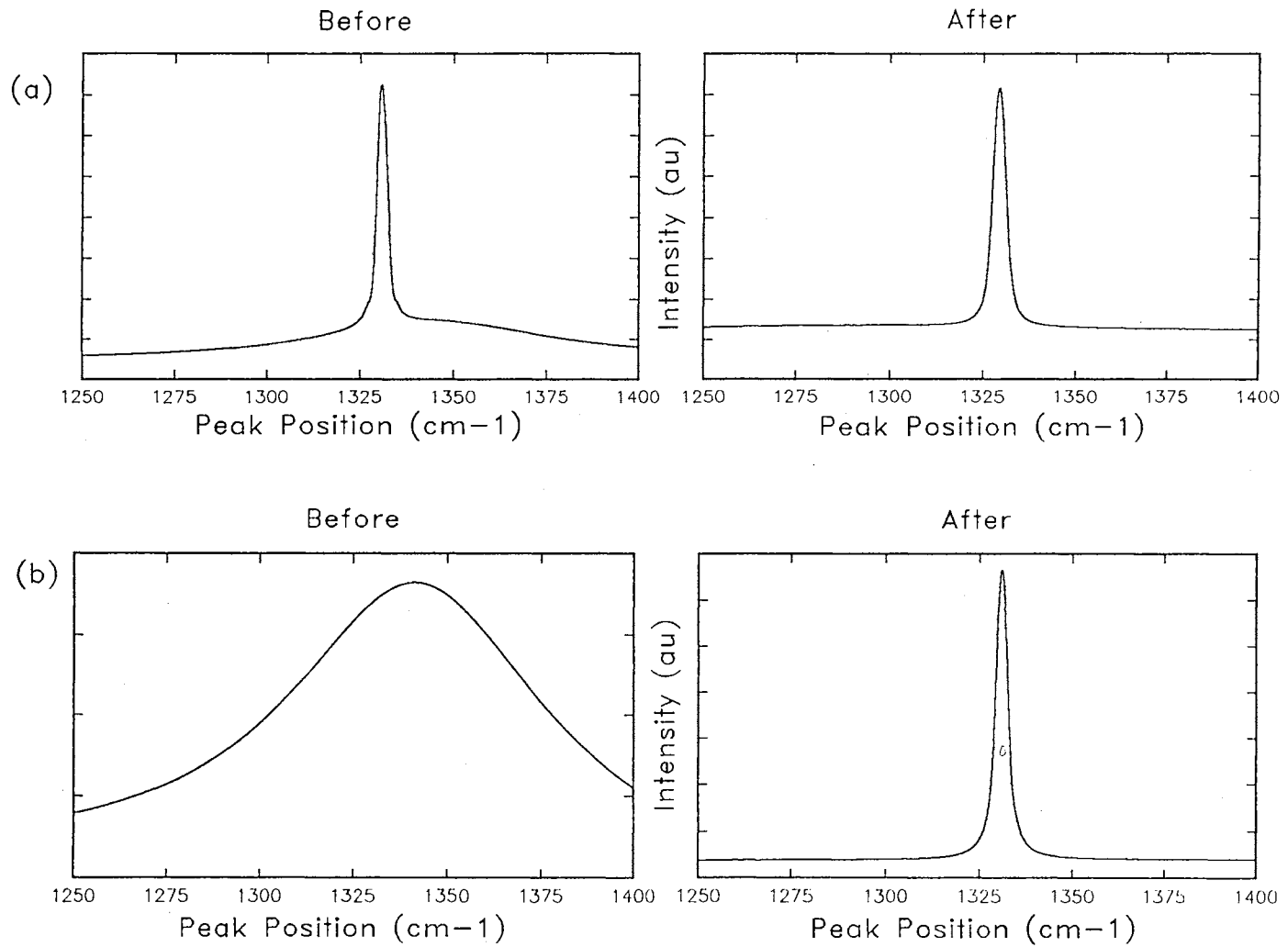


Figure 3.19. Raman spectra of CVD grains containing (a) high quality, single-crystal diamond and (b) polycrystalline disordered sp^3 -bonded carbon before and after tube furnace annealing.

of 200 sccm hydrogen with 2% CH₄ and 0.5% N₂, filament and substrate temperatures of 1900°C and 1000°C, and a pressure of 30 Torr. N-doped samples differed in appearance from the usual samples in that the grain densities were substantially reduced and that all growth rings, especially the inner ones, appeared to contain lower levels of graphitic grains as the nitrogen concentration was increased. N-doped grains were slightly larger than average -- sometimes double the diameter of their standard CVD counterparts. However, this is to be expected since reduced nucleation densities cause increased growth rates.

Most N-doped grains were silver cauliflower and cauli-faceted, though samples doped with 0.25% nitrogen also contained slightly darker cauliflower grains closer to the center. Raman analysis of these grains revealed diamond peak positions and widths comparable to those of the standard CVD grain categories. In finding that the peak position vs. temperature curve could be properly fit using $\omega(0)$ values no different from those of standard grains, and knowing that nitrogen substitutions, being larger than carbon atoms, should shift the diamond peak to higher frequencies, it is believed that the number of nitrogen substitutions in the diamond lattice is rather low. Laser-annealing studies on the N-doped grains produced the same unsuccessful results commonly seen with standard silver cauliflower and cauli-faceted grains, where they could not be heated to 700°C at even the maximum laser power of 2.0 W.

In summary, the most significant finding in the production of N-doped diamond is the considerable drop in nucleation densities - estimated to be 2 to 4 orders of magnitude less than the densities on standard CVD substrates. This observation implies a reduction in nucleation sites, the result of competition between nitrogen and carbon at the silicon surface. Though Raman analysis of the substrates revealed neither silicon nitride or silicon carbide, the formation of even a thin layer of silicon nitride would certainly inhibit the growth of diamond.

Tube Furnace Annealing in Nitrogen By annealing several (standard) samples in the tube furnace using only nitrogen, the comparative effects of oxygen and nitrogen annealing were determined. Without oxygen, grains were seen to experience no mass loss, and in some cases, yellow and blue interference patterns and small (~ 0.5 μm) black dots were actually seen to form across the surface. These

effects are believed to be attributed to the formation of silicon nitride on the surface, although Raman spectra again show no sign of this material. Spectra of the diamond and silicon taken from the same growth rings on the annealed and unannealed portions of each sample revealed no changes in the quality of either the grains or the silicon after annealing. From these results, it is concluded that only oxygen participates in the selective removal of impurities from the diamond lattice.

Suggested Models for the CVD Diamond Grain Conversion Process

By collectively considering the results of the present chapter, two models are now proposed to explain the conversion process by which CVD diamond grains are improved. These models both assume grain improvement to occur with the selective removal of impurities from diamond grains, but differ in the assumed distributions of defects throughout the grains. These two distributions, one homogeneous and the other radially-varying, are respectively inspired by the SEM photographs of the annealed single-crystal and cauliflower grains.

The Homogeneous Defect Distribution Model In this model, diamond grains are assumed to have a predominantly homogeneous distribution of disordered sp^2 and sp^3 bonds, hydrogen inclusions, and other impurities throughout what would otherwise be single-crystal diamond. These grains are believed to rest on a thin layer of silicon carbide atop the silicon substrate, as illustrated in Figure 3.20. In this model, laser light incident on the grain is absorbed by the sp^2 carbon and other impurities, homogeneously embedded in the diamond lattice, resulting in grain heating and thermal expansion. With this expansion, small quantities of impurities escape from the lattice, causing a reduction in the absorption coefficient of the grain. The resultant enhanced transparency causes the Raman scattering intensities of both the diamond and the underlying silicon to increase and the grain temperature to drop.

Each time the conversion temperature is reached, more impurities are able to escape from the lattice and in so doing cause a reduction in the localized strains perturbing some number of the crystal's unit cells. As the perturbations on more and more unit cells are removed and the crystal potential becomes more homogeneous, the diamond peak is seen to become narrower. The underlying silicon

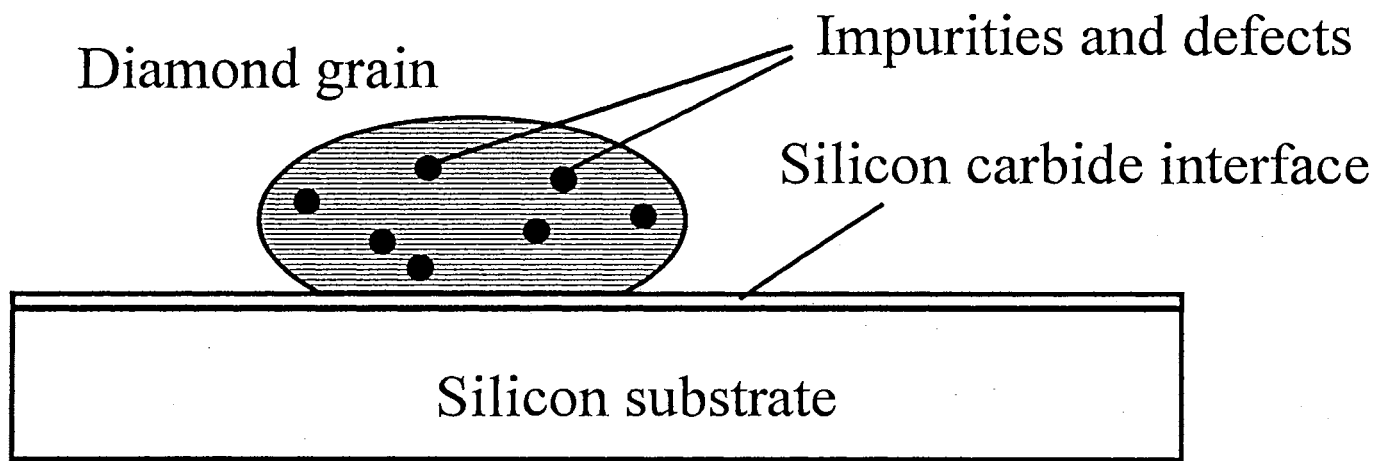


Figure 3.20. The homogeneous defect distribution model proposed to explain grain conversion.

substrate is unaffected by the removal of impurities because, although the silicon carbide layer may be more or less perturbed by the removal of impurities, it is not significantly reduced.

The Radially-Varying Defect Distribution Model In this model, proposed for polycrystalline grains, the defect distribution is assumed to vary with the radial distance from the grain center. The outer layers are believed to have higher levels of disordered sp^2 and sp^3 bonds, hydrogen inclusions, and other impurities than the grain core, which is assumed to contain only diamond and a minimal number of defects. The diamond grain may be directly atop silicon or on a transition layer of silicon carbide, as shown in Figure 3.21.

The majority of the laser light incident on the grain will be absorbed by the outer layer, since it contains the largest level of impurities. Because the thermal properties of this disordered diamond are considerably reduced, this layer may be excessively heated and vaporize, thus exposing inner layers of the grain. This process would continue until an inner layer with lower levels of impurities and better thermal properties is exposed, where this layer does not vaporize at the same laser power. Because this newly exposed layer is less absorptive, more of the laser light is able to penetrate into the grain core and the underlying silicon, so that the scattering intensities of both increase. Since the diamond at the center of the sample is higher in quality than the removed outer diamond layers, the subtraction of these broader contributions from the Raman spectra results in a reduction of the diamond peak width.

As the conversion temperature is repeatedly reached, more and more impurities are removed from the outer layers of the grain. The remaining inner layers of higher quality diamond produce a much narrower Raman peak than the poorer-quality material in the outer layers which had previously obscured this core. Since the base of the grain has, for the most part, remained constant throughout the conversion, the removal of the outer layers of the grain has no effect on the underlying interface and/or substrate.

Model Determination In order to determine which of the two models is more appropriate for a given grain, crystal orientation studies may be undertaken, again using micro-Raman spectroscopy. By rotating samples with respect to the incident polarized laser light, single-crystal and polycrystalline grains are easily differentiated, since the more single crystal the sample is, the more identical the components of

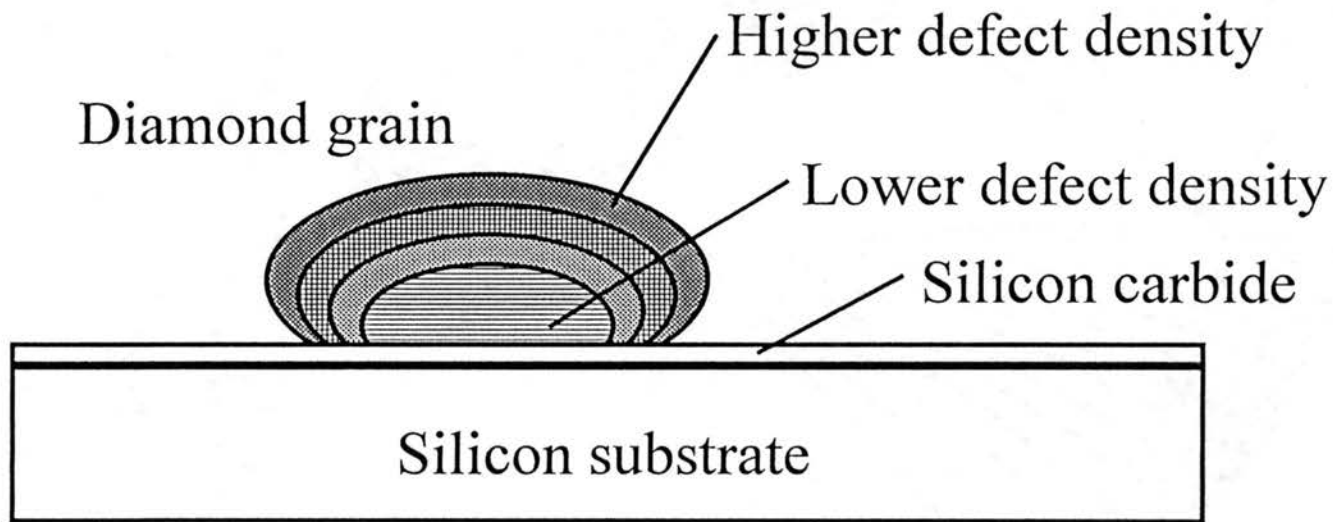


Figure 3.21. The radially-varying defect distribution model proposed to explain grain conversion.

the induced dipole moment $\mathbf{p} = \alpha\mathbf{E}$ (which is clearly dependent on orientation) will be. Just as the silicon substrate gives the strongest Raman signal when the (110) direction is aligned with the polarized laser beam, the same is true for single-crystal diamond grains. Grains more polycrystalline in nature do not show this directional dependence since the crystal axes in the innumerable unit cells are more randomly oriented.

Chapter Summary

By laser annealing CVD diamond grains at temperatures of 700 to 900°C in the atmosphere, the quality of diamond is seen to be greatly enhanced, as ascertained from the width of the Raman diamond peak. This enhancement is accompanied by a lightening in grain color and, as observed in SEM photographs, some degree of mass loss. Increases in the Raman scattering intensities of both the diamond and the underlying silicon substrate also occur in the annealing process, suggesting that grain improvement is due to the selective removal of absorbing impurities from the lattice.

An irreversible narrowing of the diamond peak is seen to occur with the annealing of poorer-quality grains, attributed to the removal of strain-broadening mechanisms. Many grains which initially displayed only disordered sp^3 Raman peaks were seen to develop quite narrow ($\sim 4 \text{ cm}^{-1}$) diamond peaks after annealing. This hysteresis was less noticeable in grains which were initially high in quality, since the levels of inhomogeneous broadening in these grains were small to begin with.

Analysis of the Raman diamond peak as a function of temperature revealed that the diamond peak positions of all grains in this study are shifted equally with temperature. This shift is shown to be almost entirely attributed to volume expansion, where CVD grains are found to have roughly the same thermal expansion as natural diamond.

Raman studies of the silicon substrate before and after annealing suggest that the silicon is not changed in any way by the annealing process. However, because the temperature gradient between the diamond grains and the underlying substrate is seen to increase with annealing, attributed to changes in the boundary layer between the two materials, the existence of a transition layer is hypothesized. This

claim is reinforced by observations of perturbations on the silicon peak at points away from diamond grains and interference patterns sometimes seen at the clamped corners of substrates.

By tube furnace annealing several samples in conditions similar to those of laser annealing, grains were proven to be improved in essentially the same manner by both laser and tube furnace annealing, aside from the variations in mass loss seen across the grain surface. Additional tube furnace studies have revealed that the thickness of the transition layer is not affected by annealing and that oxygen is entirely responsible for the selective removal of impurities. Nitrogen was believed to form silicon nitride on the substrate, as evidenced by black dots developed across the silicon with nitrogen annealing and the reduced grain densities seen in attempts to produce N-doped diamond.

Based on the findings in this study and the SEM photographs of annealed grains with different morphologies, two modes for grain structure have been proposed. Single-crystal grains are believed to have homogeneous defect distributions while those in polycrystalline grains vary radially. The selective removal of impurities from these two models has been hypothesized, with all explanations agreeing with the observed findings.

CHAPTER IV

SUMMARY AND SUGGESTIONS FOR FUTURE RESEARCH

This study has shown that the quality of CVD diamond grains may be greatly enhanced by open-air laser annealing at temperatures of 700 to 900°C. This occurs as a result of oxygen selectively removing impurities from the diamond lattice, which can be observed in the reduction of the Raman diamond peak width as the strain-broadening mechanisms are removed. SEM photographs of annealed grains show mass loss correlated with morphology, so that poorer quality grains experience the largest reductions in mass.

Further Raman analysis has shown the fundamental silicon lattice to be unaffected by the annealing process, though it is also shown that diamond grains become more thermally-disconnected from the silicon after annealing. The existence of a thin boundary layer of silicon carbide is proposed to explain these inconsistencies, encouraged by occasional presence of interference patterns in the outer growth regions and several tube furnace annealing studies.

Future research should certainly include interfacial studies to either prove or disprove the existence of the transition layer and determine its composition. This would most likely be done using some form of electron diffraction, so that only the surface, and not the bulk of the sample is penetrated. If the transition layer does indeed exist, electron diffraction measurements made before and after annealing could determine whether the layer is improved or worsened with annealing.

Also of interest to the author is the intentional "dissection" of diamond grains by laser exposure. Several SEM photographs in this study which contained grain cross-sections etched by laser annealing proved quite helpful in understanding the defect distributions within grains. Using a more powerful laser, the inner layers of the silver cauli-faceted and faceted grain types could be exposed and the unusually large diamond peak widths of the single-crystal silver faceted grains could perhaps be better explained.

A third suggestion for future research involves the study of homoepitaxial diamond growth on annealed grains of all qualities. It would be interesting to see if high quality films could be grown over a larger area of the substrate by alternately growing and annealing. In this way, a semi-continuous web of diamond could be constructed. These porous surfaces, as well as those of laser annealed individual diamond grains, could have potential uses as abrasives.

The most obvious current applications for laser-induced CVD diamond enhancement are in the microelectronics industry, where the microscopic control of material properties is essential. Diamond films are currently in the developmental stage of use as heat sinks, but because of temperature limitations on the other microchip components, these films are often of poor quality. By laser annealing these films, thermal conductivities could be greatly improved, allowing both quicker cooling and a reduction in heat sink size.

When diamond semiconductors become feasible, laser annealing may be used in conjunction with masks to controllably alter micron-sized areas of the films. Portions of these films could not only be selectively improved by laser annealing, but could also be vaporized using excessive laser powers. Since diamond has a high frequency limit much larger than that of silicon, this would enable the production of faster computers than ever before realized.

The repeated growth and annealing of diamond films could have many other low temperature applications besides the improvement of diamond heat sinks described above. Diamond has been grown at low temperatures ($< 500^{\circ}\text{C}$) on a wide variety of materials, but consequently contains high levels of defects and sp^2 -bonded carbon. However, since the laser annealing procedure heats the substrate only minimally, these large scale films may be improved a portion at a time. With this technique, the concept of scratch-proof sunglasses may some day become a reality.

REFERENCES

1. Max N. Yoder, in *Diamond Films and Coatings* (Noyes, New Jersey, 1993), ed. Robert F. Davis, pp. 2-4.
2. L. Robbin Martin, *Amer. Cer. Soc. Bull.* **71**, 1419 (1992).
3. Kurt Nassau, in *Diamond Films and Coatings* (Noyes, New Jersey, 1993), ed. Robert F. Davis, pp. 31-67.
4. Michael W. Geis and John C. Angus, *Sci. Amer.*, October, 1992, p. 84 (1992).
5. B.V. Derjaguin and D.V. Fedoseev, *Sci. Amer.* **233**, 102 (1975).
6. Richard J. Koba, in *Diamond Films and Coatings* (Noyes, New Jersey, 1993), ed. Robert F. Davis, pp. 147-157.
7. S. Matsumoto, Y. Sato, M. Kamo, and N. Setaka, *J. Appl. Phys.* **21**, L183 (1982).
8. F. Davanloo, E.M. Juengerman, D.R. Jander, T.J. Lee, and C.B. Collins, *J. Appl. Phys.* **67**, 2081 (1990).
9. A. Hiraki, K. Toshifumi, and Y. Kawakami, *Sol. State Comm.* **50**, 713 (1984).
10. G. Popovici, and M.A. Prelas, *Phys. Stat. Sol. (a)* **132**, 233 (1992).
11. F.G. Celii, D. White, Jr., and A.J. Purdes, *J. Appl. Phys.* **70**, 5636, (1991).
12. Bernard J. Bulkin, "The Raman Effect: An Introduction," in *Analytical Raman Spectroscopy* (John Wiley & Sons, New York, 1991), p. 1.
13. Marvin C. Tobin, *Laser Raman Spectroscopy* (John Wiley & Sons, New York, 1971), p. 1.
14. Karl W. Böer, *Survey of Semiconductor Physics* (Van Nostrand Reinhold, New York, 1990), p. 95.
15. S. Bhagavantam, *Scattering of Light and the Raman Effect* (Chemical Publishing Company, Brooklyn, 1942), p. 229.
16. Charles Kittel, *Introduction to Solid State Physics*, 6th ed. (John Wiley & Sons, New York, 1986), p. 114.
17. B. Di Bartolo, *Optical Interactions in Solids* (John Wiley & Sons, New York, 1968), p. 357.
18. M. Yoshikawa, G. Katagiri, H. Ishida, and A. Ishitani, *Appl. Phys. Lett.* **55**, 2608 (1989).
19. Bernard Yates, *Thermal Expansion* (Plenum Press, New York, 1972), p. 35.

20. A.M. Bonnot, *Phys. Rev. B* **41**, 6040 (1990).
21. G.T. Visscher, D.C. Nesting, J.V. Badding, and P.A. Bianconi, *Science* **260**, 1496 (1993).
22. Walter A. Yarbrough and Russell Messier, *Science* **247**, 688 (1990).
23. K. Suhm, "Synthesis of Lonsdaleite by Filament-Assisted Chemical Vapor Deposition", Oklahoma State University Master's Thesis, 1993.
24. N. Uchida, T. Kurita, K. Uematsu, K. Saito, *J. Mater. Sci. Lett.* **9**, 249 (1990).
25. K. Suhm, unpublished results.
26. Hugh O. Pierson, *Handbook of Chemical Vapor Deposition* (Noyes Publications, New Jersey, 1992), p. 17.
27. A.R. Badzian, *Mater. Res. Bull.* **23**, 385 (1988).
28. Pehr E. Pehrsson, Frances G. Celi, and James E. Butler, in *Diamond Films and Coatings* (Noyes, New Jersey, 1993), ed. Robert F. Davis, pp. 68-146.
29. S. Matsumoto, and Y. Matsui, *J. Mater. Sci.* **18**, 1785 (1983).
30. P.X. Ling, *Mater. Sci. and Eng.* **B14**, L15 (1992).
31. P.O. Joffreau, R. Jaubner, and B. Lux, in *Diamond and Diamond-Like Materials Synthesis*, April 1988, eds. G.H. Johnson, A.R. Badzian, and M.W. Geis (Materials Research Society, 1988), pp. 15-18.
32. B.E. Williams, J.T. Glass, R.F. Davis, and K.J. Kobashi, *J. Cryst. Growth* **99**, 1168 (1990).
33. B.E. Williams, and J.T. Glass, *J. Mater. Res.* **4**, 373 (1989).
34. R.F. Decker, E.W. Fournier, J. Asmussen, K. Bigelow, and J. Hoggins, *Microwave Processing for Diamond Films*, pamphlet distributed by Wavemat, Inc.
35. J.S. Kim, M.H. Kim, S.S. Park, and J.Y. Lee, *J. Appl. Phys.* **67**, 3354 (1990).
36. K. Kumagai, K. Miyata, K. Nishimura, and K. Kobashi, *J. Mater. Res.* **8**, 314 (1993).
37. W. Zhu, C. Randall, A.R. Badzian, and R. Messier, *J. Vac. Sci. Technol. A* **7**, 2315 (1989).
38. R. Meilunas, M.S. Wong, K.C. Sheng, and R.P.H. Chang, *Appl. Phys. Lett.* **54**, 2204 (1989).
39. M.D. Perry and L.M. Raff, *J. Phys. Chem.* **98**, 4375 (1994).
40. Y. Muranka, H. Yamashita, and H. Miyadera, *J. Appl. Phys.* **69**, 8145 (1991).
41. T. Kawato and K. Kondo, *Jap. J. Appl. Phys.* **26**, 1429 (1987).
42. N. Uchida, T. Kurita, K. Uematsu, and K. Saito, *J. Mater. Sci. Lett.* **9**, 251.
43. R.E. Shroder and R.J. Nemanich, *Phys. Rev. B* **41**, 3738 (1990).

44. R.G. Buckley, T.D. Moustakas, Ling Ye, and J. Varon, *J. Appl. Phys.* **66**, 3595 (1989).
45. *CRC Handbook of Chemistry and Physics*, 74th ed. (CRC Press, Boca Raton, 1993), eds. David R. Lide and H.P.R. Frederikse, p. I-10.
46. M. Mohaupt, C. Ralter, M. Klenner, and W. Ludwig, *Phys. Stat. Sol. (b)* **180**, 357 (1993).
47. Karl W. Böer, *Survey of Semiconductor Physics* (Van Nostrand Reinhold, New York, 1990), p. 44.
48. D.S. Knight, W.R. Drawl, A.R. Badzian, T. Badzian, and W.B. White, in *Diamond and Diamond-Like Materials Synthesis*, April 1988, eds. G.H. Johnson, A.R. Badzian, and M.W. Geis (Materials Research Society, 1988), p. 73.
49. D. Beeman, J. Silverman, R. Lynds, and M.R. Anderson, *Phys. Rev. B* **30**, 870 (1984).
50. A. Solin and A.K. Ramdas, *Phys. Rev. B* **1**, 1687 (1970).
51. J. Nulman, *SPIE Proc. Rapid Isothermal Processing* **1189**, 72 (1989).
52. C. Wolden, S. Mitra, and K.K. Gleason, *J. Appl. Phys.* **72**, 3750 (1992).
53. R.S. Krishnan, R. Srinivasan, and S. Devanarayanan, *Thermal Expansion of Crystals* (Pergamon Press, Oxford, 1979), p. 118.
54. W.J. Borer, S.S. Mitra, and K.V. Namjoshi, *Sol. State Comm.* **9**, 1377 (1971).
55. S.S. Mitra and O. Brafman, *Phys. Rev.* **186**, 942 (1969).
56. E. Whalley, A. Lavergne, and P.T.T. Wong, *Rev. Sci. Instrum.* **47**, 845 (1976).
57. P.G. Klemens, *Phys. Rev.* **148**, 845 (1966).
58. R. Loudon, *Le Journal de Physique* **26**, 677 (1965).
59. T.R. Hart, R.L. Aggarwal, and B. Lax, *Phys. Rev. B* **1**, 638 (1970).
60. A.F.G. Wyatt, in *Nonequilibrium Superconductivity, Phonons, and Kapitza Boundaries*, ed. Kenneth E. Gray (Plenum Press, New York, 1981), p. 31.
61. S. Nakashima, K. Kisoda, *J. Appl. Phys.* **75**, 5354 (1994).
62. P. Gans, *Vibrating Molecules* (William Clowes & Sons, London, 1971), p. 54.

APPENDIX A

BASIC THEORY OF RAMAN SCATTERING

Rayleigh Scattering and the Depolarization Ratio Consider a molecule in general. When an electric field \mathbf{E} is incident on the molecule, the induced dipole moment is different in different directions because the molecule is polarized more easily in some directions than others. The induced dipole within a molecule and the incident electric field are related according to the equation

$$\mathbf{p} = \alpha\mathbf{E} + \beta\mathbf{E}\cdot\mathbf{E} + \gamma\mathbf{E}\mathbf{E}^2 + \dots$$

where α is the polarizability, β is the hyper-polarizability, and γ is the second hyper-polarizability, all of which are tensors. Each higher-order term is ten orders of magnitude smaller than the last, so the non-linear effects can only be seen using the most intense pulsed lasers. As a result, terms higher than first order can often be neglected and the induced dipole moment is approximately given by

$$\mathbf{p} = \alpha\mathbf{E}$$

This expression is equivalent to the set of equations

$$p_x = \alpha_{xx}E_x + \alpha_{xy}E_y + \alpha_{xz}E_z,$$

$$p_y = \alpha_{yx}E_x + \alpha_{yy}E_y + \alpha_{yz}E_z,$$

$$p_z = \alpha_{zx}E_x + \alpha_{zy}E_y + \alpha_{zz}E_z,$$

where the α_{ij} 's are the components of the polarizability tensor and in almost every case, $\alpha_{ij} = \alpha_{ji}$. If the principle axes of the polarizability ellipsoid, x , y , and z , are chosen as the coordinate axes of the molecule, then the components α_{xy} , α_{yz} , and α_{zx} vanish.

Consider a molecule at rest with coordinate axes along the principle axes of the polarizability ellipsoid. The only non-zero polarizability components are thus α_{xx} , α_{yy} , and α_{zz} . Suppose a beam of linearly polarized radiation falls on the molecule along the z -axis, with the oscillating electric field vector,

$\mathbf{E} = E_0 \cos(2\pi\nu_0 t)$, making an angle θ with the x-axis. The components of the induced dipole moment are then

$$p_x = \alpha_{xx} E \cos\theta = \alpha_{xx} E_0 \cos(2\pi\nu_0 t) \cos\theta,$$

$$p_y = \alpha_{yy} E \sin\theta = \alpha_{yy} E_0 \cos(2\pi\nu_0 t) \sin\theta,$$

$$p_z = 0,$$

and the scattered radiation is not shifted in frequency. This represents Rayleigh scattering.

The induced dipole moment \mathbf{p} makes an angle

$$\phi = \tan^{-1} \frac{p_y}{p_x} = \tan^{-1} \frac{\alpha_{yy} \sin\theta}{\alpha_{xx} \cos\theta}$$

with the x-axis and the directions of \mathbf{p} and \mathbf{E} are different unless the molecule is isotropic about the z-axis, whereby $\alpha_{xx} = \alpha_{yy}$. The conclusion of this result is that scattered radiation is generally no longer polarized in the same direction as the incident radiation.

The depolarization ratio, defined as the ratio of the intensity of the scattered radiation polarized *perpendicular* to the plane containing the incident electric field and propagation vectors to the intensity of the scattered radiation polarized *parallel* to this plane, is given by

$$\rho = \frac{(p_x \sin\theta - p_y \cos\theta)^2}{(p_x \cos\theta + p_y \sin\theta)^2} = \frac{(\alpha_{xx} E \cos\theta \sin\theta - \alpha_{yy} E \sin\theta \cos\theta)^2}{(\alpha_{xx} E \cos^2\theta + \alpha_{yy} E \sin^2\theta)^2} = \frac{(\alpha_{xx} - \alpha_{yy})^2 \cos^2\theta \sin^2\theta}{(\alpha_{xx} \cos^2\theta + \alpha_{yy} \sin^2\theta)^2}$$

Analyzing this equation, it is apparent that the scattered radiation will generally be in a different direction than the incident radiation, unless $\alpha_{xx} = \alpha_{yy} = \alpha_{zz}$.

Vibrational Raman Scattering Consider now a molecule vibrating in one of its normal modes. The polarizability α is a function of the relative coordinates which define the positions of the atoms. For small displacements from equilibrium, the components of the polarizability tensor may be expanded in a Taylor series as

$$\alpha_{ij} = \alpha_{ij}^0 + \alpha_{ij}^1 Q_k + \dots$$

where α_{ij}^0 is the equilibrium position of the ij -component of the polarizability, Q_k is the k^{th} normal coordinate, and $\alpha_{ij}^1 = (\partial\alpha_{ij}/Q_k^0)$ is the rate of change in the ij -component of polarizability with respect to Q_k measured in equilibrium. The normal coordinate Q_k varies periodically and may be described by

$$Q_k = Q_k^0 \cos(2\pi\nu_k t).$$

Combining the equations for α_{ij} and Q_k with the equations for the components of \mathbf{p} and again assuming an oscillating electric field vector $\mathbf{E} = \mathbf{E}_0 \cos(2\pi\nu_0 t)$ gives

$$\begin{aligned} p_i &= \sum_j \alpha_{ij}^0 E_{0j} \cos(2\pi\nu_0 t) + \sum_j E_{0j} Q_k^0 \alpha_{ij}^1 \cos(2\pi\nu_0 t) \cos(2\pi\nu_k t) \\ &= \sum_j \alpha_{ij}^0 E_{0j} \cos(2\pi\nu_0 t) + \frac{1}{2} [\cos(2\pi(\nu_0 - \nu_k)t) + \cos(2\pi(\nu_0 + \nu_k)t)] \sum_j E_{0j} Q_k^0 \alpha_{ij}^1 \end{aligned}$$

The induced dipole moment is thus the superposition of three periodically changing moments, the frequencies of which are ν_0 , $(\nu_0 - \nu_k)$, and $(\nu_0 + \nu_k)$. These frequencies represent Rayleigh scattering and Stokes and anti-Stokes Raman scattering, respectively.

Rotational Raman Scattering Next consider a uniformly rotating molecule. Let a primed set of axes (x' , y' , z') be fixed to the molecule, with directional cosines relating the primed coordinate system (x' , y' , z') to the unprimed coordinates (x , y , z) fixed in space. Let the molecule be rotating about the z ($= z'$) axis with frequency ν_r , as shown in Figure A.1. Assume an incident oscillating electric field of magnitude $E = E_0 \cos(2\pi\nu_0 t)$ directed along the x -axis. Expressing the components of the induced dipole moment along the fixed x and y axes in terms of the primed coordinates gives

$$p_x = p_{x'} \cos(2\pi\nu_r t) - p_{y'} \sin(2\pi\nu_r t),$$

$$p_y = p_{x'} \sin(2\pi\nu_r t) + p_{y'} \cos(2\pi\nu_r t).$$

But $p_{x'}$ and $p_{y'}$ are related to the electric field by the relations

$$p_{x'} = \alpha_{x'x'} E \cos(2\pi\nu_r t) = \alpha_{x'x'} E_0 \cos(2\pi\nu_0 t) \cos(2\pi\nu_r t),$$

$$p_{y'} = -\alpha_{y'y'} E \sin(2\pi\nu_r t) = -\alpha_{y'y'} E_0 \cos(2\pi\nu_0 t) \sin(2\pi\nu_r t).$$

Placing these expressions for $p_{x'}$ and $p_{y'}$ into the equations for p_x and p_y yields

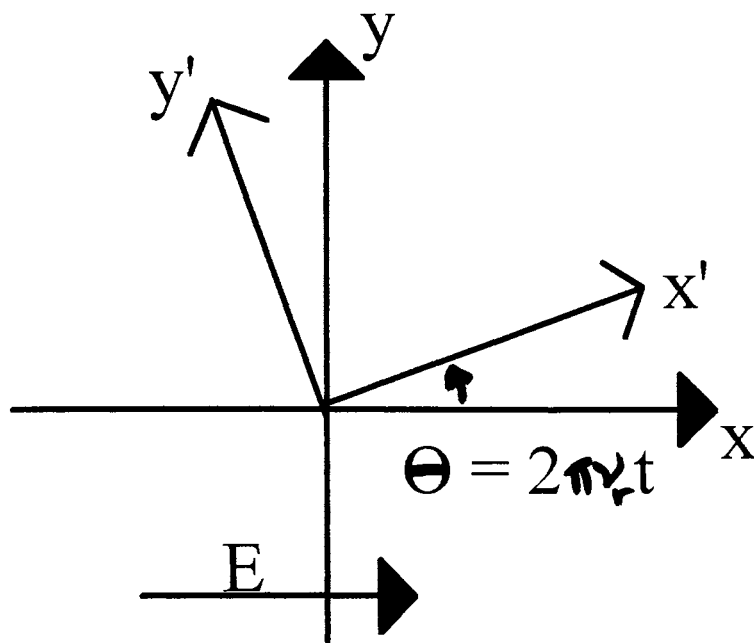


Figure A.1. Primed coordinate system (x' , y' , z') rotating with respect to a fixed coordinate system (x , y , z) about the z ($=z'$) axis with frequency ν_r .

$$p_x = \alpha_{x'x'} E_o \cos(2\pi\nu_o t) \cos^2(2\pi\nu_r t) + \alpha_{y'y'} E_o \cos(2\pi\nu_o t) \sin^2(2\pi\nu_r t),$$

$$p_y = \alpha_{x'x'} E_o \cos(2\pi\nu_o t) \cos(2\pi\nu_r t) \sin(2\pi\nu_r t) - \alpha_{y'y'} E_o \cos(2\pi\nu_o t) \sin(2\pi\nu_r t) \cos(2\pi\nu_r t),$$

and with the use of several trigonometric identities, these become

$$p_x = \frac{E_o}{2} (\alpha_{x'x'} + \alpha_{y'y'}) \cos(2\pi\nu_o t) + \frac{E_o}{4} (\alpha_{x'x'} - \alpha_{y'y'}) [\cos(2\pi(\nu_o - 2\nu_r)t) + \cos(2\pi(\nu_o + 2\nu_r)t)],$$

$$p_y = \frac{E_o}{4} (\alpha_{x'x'} - \alpha_{y'y'}) [\sin(2\pi(\nu_o - 2\nu_r)t) + \sin(2\pi(\nu_o + 2\nu_r)t)].$$

From these expressions, it can be seen that the scattered radiation has frequencies ν_o , $(\nu_o - 2\nu_r)$, and $(\nu_o + 2\nu_r)$, which represent Rayleigh scattering and pure rotational Stokes and anti-Stokes Raman scattering, respectively. Note that the rotation shifts the frequency by $\pm 2\nu_r$ instead of ν_r , as in the vibrational Raman effect. This is because for rotations, the polarizability tensor and induced dipole moment resume their original values after a rotation through π and complete two cycles after 2π .

The rotational Raman effect is not present when the polarizability ellipsoid is isotropic about the axis of rotation (in this case, $\alpha_{x'x'} = \alpha_{y'y'}$). This is obvious from the depolarization ratio as well as from the final p_x and p_y equations above. If the polarizability ellipsoid is symmetric in the $x'y'$ -plane, the rotation of the molecule about the z' -axis will not affect the direction of the induced dipole moment. Thus, for isotropic molecules, the induced dipole moment will always coincide with the direction of the incident field [62]. For rotation about an arbitrary axis, the condition for the rotational Raman effect to be absent is that $\alpha_{x'x'} = \alpha_{y'y'} = \alpha_{z'z'}$.

Rotational-Vibrational Raman Scattering Now consider a molecule which is both vibrating in one of its normal modes and rotating about the z' -axis with frequency ν_r . Again define the orientation of the molecule by means of a set of axes (x' , y' , z') fixed to the molecule with directional cosines relating these axes to the set (x , y , z) fixed in space. The component of the induced dipole moment along a fixed direction is

$$p_i = p_{x'} \cos IX' + p_{y'} \cos IY' + p_{z'} \cos IZ',$$

in which $\cos IJ'$ is the directional cosine relating the primed coordinate J' to the unprimed coordinate I , and p_i' is given by

$$p_i' = \sum_j \alpha_{ij}^{\circ} E_{oj} \cos(2\pi\nu_o t) + \frac{1}{2} \left[\cos(2\pi(\nu_o - \nu_k)t) + \cos(2\pi(\nu_o + \nu_k)t) \right] \sum_j E_{oj} Q_k^{\circ} \alpha_{ij}^1$$

where i and j are primed coordinates. To keep things simple, again assume the rotation in Figure A.1 and suppose the normal mode vibration to be such that the only non-zero rates of change in the polarizability are $\alpha_{x'x'}^1 = (\partial\alpha_{x'x'}^{\circ}/\partial Q_k^{\circ})$ and $\alpha_{y'y'}^1 = (\partial\alpha_{y'y'}^{\circ}/\partial Q_k^{\circ})$. The components of the induced dipole moment in the x and y directions are then

$$p_x = \left[\alpha_{x'x'}^{\circ} E_{ox'} \cos(2\pi\nu_o t) + \frac{1}{2} \left[\cos(2\pi(\nu_o - \nu_k)t) + \cos(2\pi(\nu_o + \nu_k)t) \right] E_{ox'} Q_k^{\circ} \alpha_{x'x'}^1 \right] \cos(2\pi\nu_r t) + \left[\alpha_{y'y'}^{\circ} E_{oy'} \cos(2\pi\nu_o t) + \frac{1}{2} \left[\cos(2\pi(\nu_o - \nu_k)t) + \cos(2\pi(\nu_o + \nu_k)t) \right] E_{oy'} Q_k^{\circ} \alpha_{y'y'}^1 \right] (-\sin(2\pi\nu_r t))$$

and

$$p_y = \left[\alpha_{x'x'}^{\circ} E_{ox'} \cos(2\pi\nu_o t) + \frac{1}{2} \left[\cos(2\pi(\nu_o - \nu_k)t) + \cos(2\pi(\nu_o + \nu_k)t) \right] E_{ox'} Q_k^{\circ} \alpha_{x'x'}^1 \right] \sin(2\pi\nu_r t) + \left[\alpha_{y'y'}^{\circ} E_{oy'} \cos(2\pi\nu_o t) + \frac{1}{2} \left[\cos(2\pi(\nu_o - \nu_k)t) + \cos(2\pi(\nu_o + \nu_k)t) \right] E_{oy'} Q_k^{\circ} \alpha_{y'y'}^1 \right] (\cos(2\pi\nu_r t))$$

which equal after some algebra

$$p_x = \alpha_{x'x'}^{\circ} E_o \cos(2\pi\nu_o t) \cos^2(2\pi\nu_r t) + \alpha_{y'y'}^{\circ} E_o \cos(2\pi\nu_o t) \sin^2(2\pi\nu_r t) + \frac{1}{2} \left[\cos(2\pi(\nu_o - \nu_k)t) + \cos(2\pi(\nu_o + \nu_k)t) \right] \left[E_o Q_k^{\circ} \alpha_{x'x'}^1 \cos^2(2\pi\nu_r t) + E_o Q_k^{\circ} \alpha_{y'y'}^1 \sin^2(2\pi\nu_r t) \right]$$

and

$$p_y = \alpha_{x'x'}^{\circ} E_o \cos(2\pi\nu_o t) \sin(2\pi\nu_r t) \cos(2\pi\nu_r t) + \alpha_{y'y'}^{\circ} E_o \cos(2\pi\nu_o t) \cos(2\pi\nu_r t) (-\sin(2\pi\nu_r t)) + \frac{1}{2} \left[\cos(2\pi(\nu_o - \nu_k)t) + \cos(2\pi(\nu_o + \nu_k)t) \right] \left[E_o Q_k^{\circ} \alpha_{x'x'}^1 \sin(2\pi\nu_r t) \cos(2\pi\nu_r t) + E_o Q_k^{\circ} \alpha_{y'y'}^1 \cos(2\pi\nu_r t) (-\sin(2\pi\nu_r t)) \right]$$

and then become, with the use of several trigonometric identities,

$$p_x = \frac{1}{2} (\alpha_{x'x'}^{\circ} + \alpha_{y'y'}^{\circ}) E_o \cos(2\pi\nu_o t) + \frac{1}{4} (\alpha_{x'x'}^{\circ} - \alpha_{y'y'}^{\circ}) E_o \left[\cos(2\pi(\nu_o + 2\nu_r)t) + \cos(2\pi(\nu_o - 2\nu_r)t) \right]$$

$$+\frac{1}{2}(\alpha_{x'x'}^1 + \alpha_{y'y'}^1) \left[\cos(2\pi(\nu_0 - \nu_k)t) + \cos(2\pi(\nu_0 + \nu_k)t) \right] E_0 Q_k^0 + \frac{1}{8}(\alpha_{x'x'}^1 - \alpha_{y'y'}^1) \left[\cos(2\pi(\nu_0 - \nu_k + 2\nu_r)t) + \cos(2\pi(\nu_0 - \nu_k - 2\nu_r)t) + \cos(2\pi(\nu_0 + \nu_k + 2\nu_r)t) + \cos(2\pi(\nu_0 + \nu_k - 2\nu_r)t) \right] E_0 Q_k^0$$

and

$$p_y = \frac{1}{4}(\alpha_{x'x'}^0 - \alpha_{y'y'}^0) E_0 \left[\sin(2\pi(\nu_0 + 2\nu_r)t) - \sin(2\pi(\nu_0 - 2\nu_r)t) \right] + \frac{1}{8}(\alpha_{x'x'}^1 - \alpha_{y'y'}^1) \left[\sin(2\pi(\nu_0 - \nu_k + 2\nu_r)t) - \sin(2\pi(\nu_0 - \nu_k - 2\nu_r)t) + \sin(2\pi(\nu_0 + \nu_k + 2\nu_r)t) - \sin(2\pi(\nu_0 + \nu_k - 2\nu_r)t) \right] E_0 Q_k^0.$$

Thus, $\nu_0 \pm 2\nu_r$ are the frequencies of the pure rotational Raman lines, $\nu_0 \pm \nu_k$ are those of the vibrational Raman lines, and $\nu_0 \pm \nu_k \pm 2\nu_r$ are the frequencies of rotational "wings" on either side of the vibrational Raman lines.

Note that if $\alpha_{x'x'}^1 = \alpha_{y'y'}^1$, the rotational-vibrational lines will completely disappear. In general, the values of $\alpha_{x'x'}^1$, $\alpha_{y'y'}^1$, $\alpha_{z'z'}^1$, $\alpha_{x'y'}^1$, $\alpha_{y'z'}^1$, and $\alpha_{z'x'}^1$ play a large role in the appearance or absence of vibrational lines and rotational-vibrational lines. The vanishing or non-vanishing of these coefficients can generally be determined from the symmetry properties of the molecule and of its vibrations.

APPENDIX B

DERIVATION OF RAYLEIGH'S ω^4 LAW

A dipole moment, oscillating with frequency ω , is found to produce scattered light with an intensity proportional to ω^4 . The proof of this begins with an introduction to the wave equations for the vector and scalar potentials, \mathbf{A} and ϕ , followed by a development of the solution to these equations for a single oscillating dipole in free space. By integrating the wave equations, the fields \mathbf{A} and ϕ are found, from which \mathbf{E} and \mathbf{B} are determined. From these, expressions for the Poynting vector, total power radiated, and the intensity may be obtained. The details of the proof are as follows:

In terms of the vector and scalar potentials, $\mathbf{A}(\mathbf{r}, t)$ and $\phi(\mathbf{r}, t)$, two wave equations exist:

$$\nabla^2 \mathbf{A} - \frac{1}{c^2} \frac{\partial^2 \mathbf{A}}{\partial t^2} - \nabla \left\{ \nabla \cdot \mathbf{A} + \frac{1}{c} \frac{\partial \phi}{\partial t} \right\} = \frac{-4\pi}{c} \left\{ \mathbf{J} + c \nabla \times \mathbf{M} + \frac{\partial \mathbf{P}}{\partial t} \right\}$$

$$\text{and } \nabla^2 \phi + \frac{1}{c} \frac{\partial(\nabla \cdot \mathbf{A})}{\partial t} = -4\pi \{ \rho - \nabla \cdot \mathbf{P} \},$$

where $\mathbf{J} = \mathbf{J}(\mathbf{r}, t)$ is the current density, $\mathbf{M} = \mathbf{M}(\mathbf{r}, t)$ is the magnetization, $\mathbf{P} = \mathbf{P}(\mathbf{r}, t)$ is the polarization, and $\rho = \rho(\mathbf{r}, t)$ is the charge density. These equations may be derived from Maxwell's equations,

$$\nabla \times \mathbf{E} = -\frac{1}{c} \frac{\partial \mathbf{B}}{\partial t},$$

$$\nabla \cdot \mathbf{B} = 0,$$

$$\nabla \cdot \mathbf{D} = 4\pi\rho,$$

$$\text{and } \nabla \times \mathbf{H} = \frac{4\pi}{c} \mathbf{J} + \frac{1}{c} \frac{\partial \mathbf{D}}{\partial t}.$$

This is done by first using the equations for the magnetic induction $\mathbf{B} = \mathbf{B}(\mathbf{r}, t)$ and the electric displacement $\mathbf{E} = \mathbf{E}(\mathbf{r}, t)$ to express \mathbf{E} and \mathbf{B} in terms of \mathbf{A} and ϕ :

$$\mathbf{B} = \nabla \times \mathbf{A}$$

$$\mathbf{E} = -\frac{1}{c} \frac{\partial \mathbf{A}}{\partial t} - \nabla \phi,$$

and then expressing the electric displacement field $\mathbf{D} = \mathbf{D}(\mathbf{r}, t)$ and the magnetic field strength $\mathbf{H} = \mathbf{H}(\mathbf{r}, t)$ in terms of \mathbf{A} and ϕ using the definitions of \mathbf{P} and \mathbf{M} ,

$$\mathbf{D} = \mathbf{E} + 4\pi\mathbf{P},$$

$$\text{and } \mathbf{H} = \mathbf{B} - 4\pi\mathbf{M},$$

and the newly found expressions for \mathbf{E} and \mathbf{B} .

With the Lorentz Gauge condition

$$\nabla \cdot \mathbf{A} + \frac{1}{c} \frac{\partial \phi}{\partial t} = 0,$$

imposed on the wave equations for \mathbf{A} and ϕ , now consider an oscillating point dipole in free space for which $\mathbf{J} = 0$, $\rho = 0$, $\mathbf{M} = 0$, and $\mathbf{P} = \mathbf{P}_0 \delta(\mathbf{r}) \cos(\omega t)$. In this case, the wave equations reduce to

$$\left\{ \nabla^2 - \frac{1}{c^2} \frac{\partial^2}{\partial t^2} \right\} \mathbf{A} = -\frac{4\pi}{c} \frac{\partial \mathbf{P}}{\partial t}$$

$$\text{and } \left\{ \nabla^2 - \frac{1}{c^2} \frac{\partial^2}{\partial t^2} \right\} \phi = 4\pi \nabla \cdot \mathbf{P}.$$

These may be expressed more succinctly in terms of the Hertz vector, $\mathbf{Z} = \mathbf{Z}(\mathbf{r}, t)$, such that

$$\mathbf{A} = \frac{1}{c} \frac{\partial \mathbf{Z}}{\partial t},$$

$$\phi = -\nabla \cdot \mathbf{Z},$$

$$\text{and } \left\{ \nabla^2 - \frac{1}{c^2} \frac{\partial^2}{\partial t^2} \right\} \mathbf{Z} = -4\pi\mathbf{P} + \boldsymbol{\gamma}$$

where $\boldsymbol{\gamma} = \boldsymbol{\gamma}(\mathbf{r})$ is an arbitrary vector field dependent only on \mathbf{r} . Setting $\boldsymbol{\gamma} = 0$, the last equation is now of the form

$$\left\{ \nabla^2 - \frac{1}{c^2} \frac{\partial^2}{\partial t^2} \right\} \Lambda(\mathbf{r}, t) = -\mathbf{S}(\mathbf{r}, t),$$

which is most easily solved by evaluating the Green's function

$$\left\{ \nabla^2 - \frac{1}{c^2} \frac{\partial^2}{\partial t^2} \right\} G(\mathbf{r}, t; \mathbf{r}', t') = -4\pi \delta(\mathbf{r} - \mathbf{r}') \delta(t - t').$$

Using this Green's function, the solution for Λ is then seen to be

$$\Lambda = \Lambda_0 + \frac{1}{4\pi} \int d^3\mathbf{r}' \int dt' G(\mathbf{r}, t; \mathbf{r}', t') S(\mathbf{r}', t')$$

where $\Lambda_0(\mathbf{r}, t)$ solves the homogeneous equation.

Evaluating the Green's function by taking a Fourier transform and using contour integration, two solutions are found -- retarded and advanced in time by an amount $|\mathbf{r} - \mathbf{r}'|/c$. The retarded Green's function,

$$G(\mathbf{r}, t; \mathbf{r}', t') = \frac{\delta(t - |\mathbf{r} - \mathbf{r}'|/c)}{|\mathbf{r} - \mathbf{r}'|}$$

is consistent with the behavior of the system. Inserting this function into the expression for Λ above and ignoring the homogeneous solution Λ_0 , we now have

$$\Lambda = \frac{1}{4\pi} \int d^3\mathbf{r}' \frac{S(\mathbf{r}', [t - |\mathbf{r} - \mathbf{r}'|/c])}{|\mathbf{r} - \mathbf{r}'|}.$$

Using this relation, the Hertz vector is then seen to have the solution

$$\mathbf{Z} = \frac{\mathbf{P}_0}{r} \cos(\omega[t - r/c]).$$

From this, the vector and scalar potentials may be found:

$$\mathbf{A} = -\frac{\omega}{c} \frac{\mathbf{P}_0}{r} \sin(\omega[t - r/c])$$

$$\text{and } \phi = -\mathbf{P}_0 \cdot \left(\frac{1}{r^2} \frac{\omega}{c} \sin(\omega[t - r/c]) - \frac{1}{r^3} \cos(\omega[t - r/c]) \right),$$

and from these, the fields \mathbf{E} and \mathbf{B} can be calculated:

$$\begin{aligned} \mathbf{E} = & \left(\frac{\omega}{c} \right)^2 \frac{\mathbf{P}_0}{r} \cos(\omega[t - r/c]) + \frac{\omega}{c} \frac{\mathbf{P}_0}{r^2} \sin(\omega[t - r/c]) - \frac{\mathbf{P}_0}{r^3} \cos(\omega[t - r/c]) \\ & + (\mathbf{P}_0 \cdot \mathbf{r}) \left\{ -\frac{3\omega}{cr^4} \sin(\omega[t - r/c]) - \frac{\omega^2}{c^2 r^3} \cos(\omega[t - r/c]) + \frac{3}{r^5} \cos(\omega[t - r/c]) \right\} \mathbf{r}, \end{aligned}$$

$$\text{and } \mathbf{B} = \left\{ \left(\frac{\omega}{cr} \right)^2 \cos(\omega[t-r/c]) + \frac{\omega}{cr^3} \sin(\omega[t-r/c]) \right\} (\mathbf{r} \times \mathbf{P}_0).$$

In the far radiation zone, where $r \gg \lambda = 2\pi c/\omega$, terms of order $(1/r)^2$ and higher may be neglected.

Taking this into consideration and arbitrarily choosing \mathbf{P}_0 to be in the \mathbf{e}_z direction, \mathbf{E} and \mathbf{B} become

$$\mathbf{E} \approx - \left(\frac{\omega}{c} \right)^2 \frac{P_0}{r} \cos(\omega[t-r/c]) \sin\theta \mathbf{e}_\theta$$

$$\text{and } \mathbf{B} \approx - \left(\frac{\omega}{c} \right)^2 \frac{P_0}{r} \cos(\omega[t-r/c]) \sin\theta \mathbf{e}_\phi.$$

The Poynting vector, $\mathbf{N}(\mathbf{r}, t) = (c/4\pi) \mathbf{E} \times \mathbf{H}$, defined as the energy flow per unit time per unit area is then

$$\mathbf{N} = \frac{c}{4\pi} \left(\frac{\omega}{c} \right)^4 \left(\frac{P_0}{r} \right)^2 \sin^2 \theta \cos^2(\omega[t-r/c]) \mathbf{e}_r.$$

Averaged over all time, this becomes

$$\langle \mathbf{N} \rangle = \frac{c}{8\pi} \left(\frac{\omega}{c} \right)^4 \left(\frac{P_0}{r} \right)^2 \sin^2 \theta \mathbf{e}_r$$

and, by integrating this function over a sphere of radius R , the total power radiated by the dipole is found to be

$$P = \frac{c}{3} \left(\frac{\omega}{c} \right)^4 P_0^2.$$

Hence, the intensity of the radiation emitted by the dipole, equal to the power per unit area, is thus proportional to ω^4 and the proof is complete.

APPENDIX C

DIAGONALIZATION OF THE HARMONIC OSCILLATOR ENERGY MATRIX

In the harmonic approximation, the N atoms in a crystal lattice are treated as masses attached by springs. These masses are assumed to experience only slight displacements from their equilibrium positions, so that the potential energy may be expanded in a Taylor series:

$$V = V_0 + \frac{1}{2} \sum_{i,j} f_{ij} q_i q_j + \dots$$

In this expression, $f_{ij} = (\partial^2 V / \partial q_i \partial q_j)$, and q_i denotes a displacement from equilibrium, with q_n , q_{n+1} , and q_{n+2} respectively representing the x, y, and z displacements of the n^{th} atom. Neglecting the constant potential energy term, V_0 , the total energy of the crystal is given by

$$E = \frac{1}{2} \sum_i \frac{p_i^2}{m_i} + \frac{1}{2} \sum_{i,j} f_{ij} q_i q_j$$

where p_i and m_i in the kinetic energy term respectively represent momentum and mass.

The energy eigenvalues are not easily found in this representation, since cross terms in the potential energy matrix make the $3N \times 3N$ total energy matrix non-diagonal. However, a new set of $3N$ *normal coordinates*, Q_k , may be chosen so that both the kinetic and potential energies are free of cross terms and the energy matrix is diagonal. This transformation is made by first introducing the mass-weighted coordinates $\alpha_i = q_i \sqrt{m_i}$, so that

$$E = \frac{1}{2} \sum_i \dot{\alpha}_i^2 + \frac{1}{2} \sum_{i,j} D_{ij} \alpha_i \alpha_j$$

where $D_{ij} = f_{ij} / \sqrt{m_i m_j}$. The next step involves diagonalizing the potential energy matrix, \mathbf{D} , by finding its $3N$ eigenvalues, ω_k^2 , and the $3N$ corresponding eigenvectors, a_{jk} , so that

$$\sum_j D_{ij} a_{jk} = \omega_k^2 a_{ik}$$

The relationship between the normal coordinates, Q_k , and the displacement coordinates, q_j , may then be chosen so that

$$q_i \sqrt{m_i} = \alpha_i = \sum_k a_{ik} Q_k$$

This gives the desired kinetic and potential energy terms when the eigenvectors, a_{ik} , are normalized to one. The energy expression, now diagonal in the normal coordinates, becomes

$$E = \frac{1}{2} \sum_k \dot{Q}_k^2 + \frac{1}{2} \sum_k \omega_k^2 Q_k^2.$$

APPENDIX D

DERIVATION OF THE SCATTERING EFFICIENCY

Using the result of Appendix B, the intensity of the light radiated by the induced dipole \mathbf{P} in making the transition from an initial state n to final state m is given by

$$I_{nm} = K\omega_s^4 |\overline{P_{nm}}|^2 d\Omega$$

where K is a constant, ω_s is the frequency of the emitted light, P_{nm} is the transition moment between states n and m , and $d\Omega$ is the solid angle of collection. The transition moment may be expressed as

$$P_{nm} = \alpha_{nm} E_o = \left(\int \psi_m^* \alpha \psi_n dQ_k \right) E_o,$$

where ψ_m and ψ_n are the vibrational wave functions of the initial and final states, E_o is the magnitude of the incident electric field, and α is the polarizability, which is only a function of the vibrational coordinate Q_k . Provided the amplitude of Q_k is small, the polarizability may expand it as a Taylor series to first order:

$$\alpha = \alpha_o + \left(\frac{\partial \alpha}{\partial Q_k} \right)_o Q_k$$

Inserting this into the expression for the transition moment yields

$$\alpha_{nm} = \int \psi_m^* \alpha_o \psi_n dQ_k + \left(\frac{\partial \alpha}{\partial Q_k} \right)_o \int \psi_m^* Q_k \alpha \psi_n dQ_k,$$

the solution of which is most easily found in the one-dimensional treatment from which the result may be applied to the 3N-dimensional case. For the one-dimensional harmonic oscillator, the vibrational wave functions are of the form

$$\psi_n(x) = N_n e^{-\xi^2/2} H_n(x)$$

where $\xi = \sqrt{\alpha x}$, $\alpha = \frac{m\omega}{\hbar}$, N_n is a normalization constant:

$$N_n = \sqrt{\left(\frac{\alpha}{\pi}\right)^{1/2} \frac{1}{2^n n!}},$$

and $H_n(x)$ is the n^{th} Hermite polynomial:

$$H_n(x) = (-1)^n e^{\xi^2} \frac{d^n e^{-\xi^2}}{d\xi^n}.$$

Using these wave functions in the expression for α_{nm} gives

$$\alpha_{nm} = \int \psi_m^*(x) \alpha_o \psi_n(x) dx + \left(\frac{\partial \alpha}{\partial x}\right) \int \psi_m^*(x) x \psi_n(x) dx.$$

The first term is zero unless $m=n$, since the wave functions are orthogonal. When $m=n$, representative of Rayleigh scattering, the first integral is equal to $2^n n! \sqrt{\pi}$. In a similar manner, the second term is equal to zero unless $m = n \pm 1$. When this condition is met, the second integral reduces to

$$\sqrt{\frac{(n+1)\hbar}{2m\omega}} \quad \text{for } m=n+1 \quad \text{and} \quad \sqrt{\frac{n\hbar}{2m\omega}} \quad \text{for } m=n-1.$$

These terms respectively correspond to Stokes and anti-Stokes Raman scattering.

Applying these results to the case of the 3N-dimensional harmonic oscillator with normal coordinates Q_k , the components of the polarizability for $m=n \pm 1$ for the k^{th} normal mode Q_k are

$$\sqrt{\frac{(n_k+1)\hbar}{2\mu\omega_k}} \quad \text{for } m=n+1 \quad \text{and} \quad \sqrt{\frac{n_k\hbar}{2\mu\omega_k}} \quad \text{for } m=n-1$$

where ω_k and n_k are respectively the frequency and occupation number of the k^{th} normal mode and μ is the reduced mass.

Inserting the Stokes component of α_{nm} into P_{nm} and the intensity expression, we get

$$I_{nm} = I_o K \frac{\hbar\omega_s^4 d\Omega}{\mu\omega_k} |\alpha_R|^2 (n_k + 1),$$

so that the Stokes Raman scattering efficiency of the k^{th} vibrational mode is given by

$$\eta = K \frac{\hbar\omega_s^4 d\Omega}{\mu\omega_k} |\alpha_R|^2 (n_k + 1).$$

2

VITA

Karen Elaine Suhm

Candidate for the Degree of

Doctor of Philosophy

Thesis: CVD DIAMOND GRAIN QUALITY ENHANCEMENT BY POST-PRODUCTION LASER ANNEALING.

Major Field: Physics

Biographical:

Personal Data: Born in Kingsville, Texas, on December 10, 1970, the daughter of Raymond and June Suhm; married Jerry Little on July 27, 1991.

Education: Graduated Valedictorian of Moore High School, Moore, Oklahoma, in May, 1989; received Bachelor of Science Degree with Honors in Physics and Mathematics from Oklahoma State University, Stillwater, Oklahoma, in December, 1991; received Masters Degree in Physics from Oklahoma State University, Stillwater, Oklahoma in December, 1993; completed the requirements for the Doctor of Philosophy Degree in Physics at Oklahoma State University in December, 1995.

Professional Experience: Instructor, PHYSC 1114, Oklahoma State University Department of Physics, Stillwater, Oklahoma, from January, 1995 to May, 1995; Graduate Research Assistant, Oklahoma State University Department of Physics, Stillwater, Oklahoma, from August, 1991 to December, 1994; Teaching Assistant, Oklahoma State University Department of Physics, Stillwater, Oklahoma, from August 1991 to December 1991.